

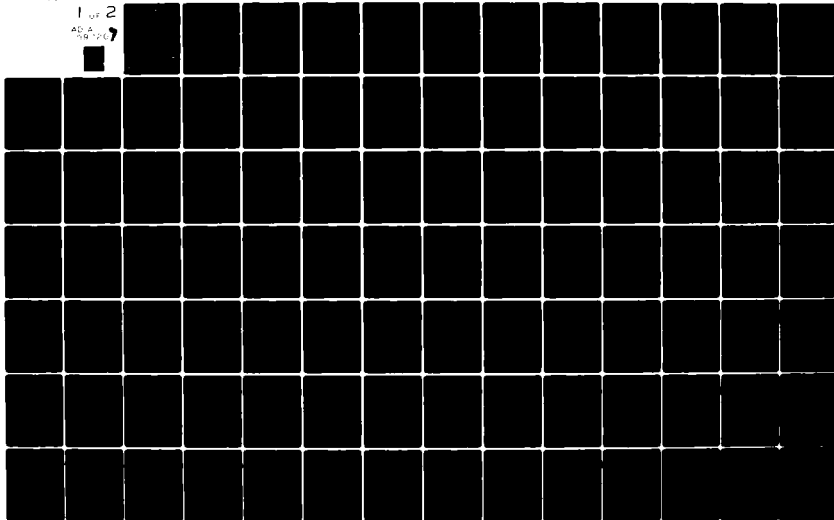
AD-A097 207

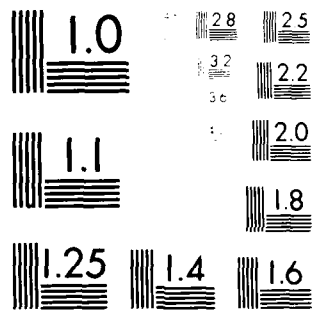
PENNSYLVANIA STATE UNIV UNIVERSITY PARK APPLIED RESE--ETC F/6 20/1  
AN EXPERIMENTAL INVESTIGATION OF OCEAN SEDIMENT EFFECTS UPON LO--ETC(U)  
DEC 80 J H BEEBE  
N00024-79-C-6043  
NL

UNCLASSIFIED

1 of 2

AD-A  
10-106





MICROCOPY RESOLUTION TEST CHART  
 NATIONAL BUREAU OF STANDARDS-1963-A

LEVEL II

10

AD A 097207

AN EXPERIMENTAL INVESTIGATION OF OCEAN SEDIMENT  
EFFECTS UPON LONG-RANGE TRANSMISSION LOSS IN  
SHALLOW WATER

John Harold/Beebe

Technical Memorandum  
File No. TM 80-247  
December 9, 1980  
Contract No. N00024-79-C-6043

Copy No. 5

The Pennsylvania State University  
Intercollege Research Programs and Facilities  
APPLIED RESEARCH LABORATORY  
Post Office Box 30  
State College, PA 16801

APPROVED FOR PUBLIC RELEASE  
DISTRIBUTION UNLIMITED

NAVY DEPARTMENT

NAVAL SEA SYSTEMS COMMAND

DTIC  
ELECTE  
S APR 2 1981 D  
D

DTIC FILE COPY

81 4 01 018

## UNCLASSIFIED

SECURITY CLASSIFICATION OF THIS PAGE (When Data Entered)

REPORT DOCUMENTATION PAGE		READ INSTRUCTIONS BEFORE COMPLETING FORM
1. REPORT NUMBER TM 80-247	2. GOVT ACCESSION NO. AD-A097 207	3. RECIPIENT'S CATALOG NUMBER
4. TITLE (and Subtitle) AN EXPERIMENTAL INVESTIGATION OF OCEAN SEDIMENT EFFECTS UPON LONG-RANGE TRANSMISSION LOSS IN SHALLOW WATER		5. TYPE OF REPORT & PERIOD COVERED PhD Thesis, May 1981
7. AUTHOR(s) John Harold Beebe		6. PERFORMING ORG. REPORT NUMBER TM 80-247
9. PERFORMING ORGANIZATION NAME AND ADDRESS The Pennsylvania State University Applied Research Laboratory P. O. Box 30, State College, PA 16801		8. CONTRACT OR GRANT NUMBER(s) N00024-79-C-6043 ✓
11. CONTROLLING OFFICE NAME AND ADDRESS Naval Sea Systems Command Department of the Navy Washington, DC 23062		10. PROGRAM ELEMENT, PROJECT, TASK AREA & WORK UNIT NUMBERS
14. MONITORING AGENCY NAME & ADDRESS (if different from Controlling Office)		12. REPORT DATE December 9, 1980
		13. NUMBER OF PAGES
		15. SECURITY CLASS. (of this report) Unclassified, Unlimited
		15a. DECLASSIFICATION/DOWNGRADING SCHEDULE
16. DISTRIBUTION STATEMENT (of this Report)  Approved for public release, distribution unlimited, per NSSC (Naval Sea Systems Command), 2/13/81		
17. DISTRIBUTION STATEMENT (of the abstract entered in Block 20, if different from Report)		
18. SUPPLEMENTARY NOTES		
19. KEY WORDS (Continue on reverse side if necessary and identify by block number)  thesis, underwater sound, sediment, absorption, transmission, loss		
20. ABSTRACT (Continue on reverse side if necessary and identify by block number) → For many shallow-water areas, the dominant effect of the environment upon sound propagation is volume absorption in the upper sedimentary layers of the seabed. In these shallow-water areas, sound propagation is generally modeled using normal-mode theory, and, within this theory, the effects of sediment absorption are implemented through the mode-attenuation coefficients. In this study, volume absorption was determined experimentally from mode- attenuation coefficients measured using explosive sources at sites having		

DD FORM 1473

JAN 73

EDITION OF 1 NOV 65 IS OBSOLETE  
5/N 0102-LF-014-6601

UNCLASSIFIED

SECURITY CLASSIFICATION OF THIS PAGE (When Data Entered)

UNCLASSIFIED

SECURITY CLASSIFICATION OF THIS PAGE (When Data Entered)

20. ABSTRACT (continued)

varied sediment types. Absorption was predicted using the sedimental models of Biot and Hamilton, and compared with the experimental absorption data. Comparisons between experimental and predicted absorption showed good agreement for three sites having medium-to-coarse sediments. The Biot model gave the best results for these sites and predicted a frequency dependence of  $f^{1.76}$  for data obtained over a frequency range of 50 to 600 Hz. The best agreement was obtained for a site having a mud bottom where the Biot model gave slightly better results than that of Hamilton over a frequency range of 25 to 250 Hz.

Transmission loss was predicted for a site on the Scotian Shelf with a sloping bottom using values of sediment absorption predicted with the sediment models. Comparisons of transmission loss measured in one-third-octave bands over a frequency range of 25 to 800 Hz showed excellent agreement below 250 Hz with the loss predicted using an adiabatic normal-mode propagation loss model whose sediment absorption inputs were obtained using the Biot model.

Accession For	
NTIS GRA&I	<input checked="checked" type="checkbox"/>
DTIC TAB	<input type="checkbox"/>
Unannounced	<input type="checkbox"/>
Justification	
By	
Distribution/	
Availability Codes	
Dist	Avail and/or Special
A	

UNCLASSIFIED

SECURITY CLASSIFICATION OF THIS PAGE (When Data Entered)

## ABSTRACT

For many shallow-water areas, the dominant effect of the environment upon sound propagation is volume absorption in the upper sedimentary layers of the seabed. In these shallow-water areas, sound propagation is generally modeled using normal-mode theory, and, within this theory, the effects of sediment absorption are implemented through the mode-attenuation coefficient.

In this study, volume absorption was determined experimentally from mode-attenuation coefficients measured using explosive sources at sites having varied sediment types. Absorption was predicted using the sedimental models of Biot and Hamilton, and compared with the experimental absorption data. Comparisons between experimental and predicted absorption showed good agreement for three sites having medium-to-coarse sediments. The Biot model gave the best results for these sites and predicted a frequency dependence of  $f^{1.76}$  for data obtained over a frequency range of 50 to 600 Hz. The best agreement was obtained for a site having a mud bottom where the Biot model gave slightly better results than that of Hamilton over a frequency range of 25 to 250 Hz.

Transmission loss was predicted for a site on the Scotian Shelf with a sloping bottom using values of sediment absorption predicted with the sediment models. Comparisons of transmission loss measured in one-third-octave bands over a frequency range of 25 to 800 Hz showed excellent agreement below 250 Hz with the loss predicted using an adiabatic normal-mode propagation loss model whose sediment absorption inputs were obtained using the Biot model.

## TABLE OF CONTENTS

	<u>Page</u>
ABSTRACT . . . . .	iii
LIST OF SYMBOLS . . . . .	vii
LIST OF FIGURES . . . . .	xi
LIST OF TABLES . . . . .	xiii
ACKNOWLEDGMENTS . . . . .	xv
Chapter	
I. INTRODUCTION . . . . .	1
II. BACKGROUND . . . . .	5
2.1 Normal-Mode Theory . . . . .	5
2.1.1 Formal Development of Normal-Mode Theory . .	7
2.1.2 Loss Mechanisms . . . . .	16
2.1.3 Previous Shallow-Water Studies . . . . .	19
2.1.4 Range-Dependent Modeling . . . . .	21
2.2 Geoacoustic Models of the Ocean Bottom . . . . .	22
2.2.1 Sediment Model of Biot . . . . .	23
2.2.2 Hamilton's Approach to Sediment Absorption .	29
III. EXPERIMENTAL PROCEDURES . . . . .	33
3.1 Background . . . . .	33
3.2 At-Sea Experiments . . . . .	34
3.3 Data Collection System . . . . .	37
3.3.1 Shipboard and In-Water Instrumentation . . .	38
3.3.2 Sensors . . . . .	40
3.3.3 Sources . . . . .	42
3.4 Analysis System and Procedures . . . . .	43
3.4.1 Hewlett-Packard Fourier System . . . . .	43
3.4.2 Received Energy Calculations . . . . .	44
3.4.3 Dispersion Analysis . . . . .	47
3.4.4 Seismic-Refraction Analysis . . . . .	53
3.5 Data Characterizing the Sediments . . . . .	58

## TABLE OF CONTENTS (continued)

<u>Chapter</u>	<u>Page</u>
IV. BOTTOM-ABSORPTION ANALYSIS - DAYTONA BEACH EXPERIMENTS . .	59
4.1 Introduction . . . . .	59
4.2 Experiments . . . . .	59
4.3 Analysis of Data--Site 1 . . . . .	63
4.3.1 Received-Energy and Mode-Attenuation Coefficients--Site 1 . . . . .	63
4.3.2 Bottom Model--Site 1 . . . . .	66
4.3.3 Experimental Sediment Absorption--Site 1 . .	71
4.3.4 Predicted Sediment Absorption--Site 1 . . .	73
4.3.5 Discussion of Results--Site 1 . . . . .	75
4.4 Analysis of Data--Site 2 . . . . .	81
4.4.1 Received-Energy and Mode-Attenuation Coefficients--Site 2 . . . . .	83
4.4.2 Bottom Model--Site 2 . . . . .	83
4.4.3 Experimental Sediment Absorption--Site 2 . .	87
4.4.4 Predicted Bottom Absorption--Site 2 . . . .	87
4.4.5 Discussion of Results--Site 2 . . . . .	91
4.5 Comparison of Results at Site 1 and Site 2 . . . .	95
V. BOTTOM-ABSORPTION ANALYSIS - CORPUS CHRISTI EXPERIMENTS .	98
5.1 Introduction . . . . .	98
5.2 Experiments . . . . .	98
5.3 Analysis of Data . . . . .	99
5.3.1 Received-Energy and Mode-Attenuation Coefficients . . . . .	102
5.3.2 Bottom Model . . . . .	105
5.3.3 Experimental Bottom Absorption . . . . .	110
5.3.4 Predicted Bottom Absorption . . . . .	110
5.4 Discussion of Results . . . . .	113



## TABLE OF CONTENTS (continued)

<u>Chapter</u>	<u>Page</u>
VI. BOTTOM-ABSORPTION ANALYSIS - PANAMA CITY EXPERIMENTS . . .	117
6.1 Introduction . . . . .	117
6.2 Experiments . . . . .	117
6.3 Analysis of Data . . . . .	119
6.3.1 Mode-Attenuation Coefficients . . . . .	120
6.3.2 Bottom Model . . . . .	120
6.3.3 Experimental Bottom Absorption . . . . .	125
6.3.4 Predicted Bottom Absorption . . . . .	127
6.4 Discussion of Results . . . . .	127
VII. PREDICTION OF TRANSMISSION LOSS - SCOTIAN SHELF EXPERIMENTS . . . . .	133
7.1 Introduction . . . . .	133
7.2 Experiments . . . . .	133
7.3 Calculation of Experimental Transmission Loss . . .	134
7.4 Calculation of Predicted Transmission Loss . . . . .	136
7.4.1 Range-Dependent Model . . . . .	136
7.4.2 Geoacoustic Model . . . . .	137
7.5 Comparison of Measured and Predicted Transmission Loss . . . . .	143
7.5.1 Experimental Transmission Loss . . . . .	147
7.5.2 Predicted Transmission Loss . . . . .	147
7.5.3 Comparison . . . . .	148
VIII. SUMMARY AND CONCLUSIONS . . . . .	152
8.1 Discussion of Results . . . . .	153
8.1.1 Environmental Effects . . . . .	153
8.1.2 Predicted Bottom Absorption . . . . .	156
8.1.3 Accuracy of Predicted Absorption . . . . .	160
8.2 Conclusions . . . . .	162
BIBLIOGRAPHY . . . . .	166
APPENDIX A: Normal-Mode Integral Equation . . . . .	172

## LIST OF SYMBOLS

<u>Symbol</u>	<u>Units</u>	<u>Definition</u>
$A_1, A_2$		Constants of integration
$A_n(\eta_x, \eta_y)$		Series expansion constant
$a_1, a_2, a_3$		Constants
$a$	cm	Pore-size parameter
$\bar{C}$	dyne/cm <sup>2</sup>	Complex elastic parameter
$c$	m/sec	Speed of sound in seawater
$c(z)$	m/sec	Sound speed varying in the depth (z) coordinate
$D$	dyne/cm <sup>2</sup>	Elastic parameter
$d$	mm	Sediment mean grain diameter
$E$	dyne/cm <sup>2</sup>	Real part of Young's modulus
$E^*$	dyne/cm <sup>2</sup>	Imaginary part of Young's modulus
$\bar{E}$	dyne/cm <sup>2</sup>	Complex Young's modulus
$e$		Dilatational strain
$F$		Fluid flow correction factor
$f$	Hz	Frequency variable
$H$	m	Water depth
$H_0^{(1)}$		Zero-order Hankel function of first kind
$\bar{H}$	dyne/cm <sup>2</sup>	Complex elastic parameter
$h$	m	Layer thickness
$K$	cm <sup>2</sup>	Sediment permeability
$K_A$	dB/km · Hz <sup>n</sup>	Sediment-absorption coefficient
$k_f$	dyne/cm <sup>2</sup>	Fluid bulk modulus
$k_r$	dyne/cm <sup>2</sup>	Frame material bulk modulus

## LIST OF SYMBOLS (continued)

<u>Symbol</u>	<u>Units</u>	<u>Definition</u>
$\bar{k}_b$	dyne/cm <sup>2</sup>	Complex frame bulk modulus
$k_b^*$	dyne/cm <sup>2</sup>	Imaginary part of frame bulk modulus
$k_b$	dyne/cm <sup>2</sup>	Real part of frame bulk modulus
$k$	1/m	Wave number
$k_n$	1/m	Modal wave number
$\bar{k}_n$	1/m	Average wave number
$\ell$	1/m	Complex wave number in sediment
$M_z$	phi	Sediment mean grain size
$\bar{M}$	dyne/cm <sup>2</sup>	Complex elastic parameter
$m$	g/cm <sup>3</sup>	Tortuosity parameter for sediment
$n$		Summation index
$p$	dyne/cm <sup>2</sup>	Acoustic pressure
$\phi$		Grain-size measure ( $-\log_2 d$ )
$R$	km	Measured experimental range
$r$		Range variable
$t$		Time variable
$t_1, t_2$	sec	Arrival time for a particular frequency
$t_w$		Arrival time for the water wave
$U(\eta_x, \eta_y, z)$		Double Fourier Transform of velocity potential
$U_n(z)$		Mode amplitude function at the receiver
$U_n(z_o)$		Mode amplitude function at the source
$u_n$	m/sec	Group velocity
$v_1, v_2, v_m$		Volume fractions

## LIST OF SYMBOLS (continued)

<u>Symbol</u>	<u>Units</u>	<u>Definition</u>
$v$	m/sec	Velocity
$v_n$	m/sec	Phase velocity
$v_s$	m/sec	Shear wave velocity
$v_E$	m/sec	Longitudinal wave velocity
$\alpha$		Pore orientation parameter
$\alpha_A$	dB/km	Sediment volume absorption
$\beta$		Porosity of sediment
$\gamma$		Total energy ratio [ $\gamma^{(1)} + \gamma^{(2)}$ ]
$\gamma_n$		Modal energy ratio
$\gamma^{(1)}, \gamma^{(2)}$		Energy ratio in sub-bottom layers
$\delta(x)$	1/m	Dirac delta function
$\delta_{mn}$		Orthogonal delta function [ $\delta_{mn} = 0, n \neq m; \delta_{mn} = 1, n = m$ ]
$\delta_1, \delta$	dB/km	Mode-attenuation coefficient for the first mode
$\delta_n$	dB/km	Mode-attenuation coefficient for the $n^{\text{th}}$ mode
$\bar{\delta}_n$	dB/km	Average mode-attenuation coefficient
$\zeta$		Fluid flow variable
$\eta_x, \eta_y$		Transform variables
$\eta$	dyne-sec/cm <sup>2</sup>	Fluid viscosity
$\kappa$		Viscous correction parameter
$\lambda$	m	Acoustic wavelength

## LIST OF SYMBOLS (continued)

<u>Symbol</u>	<u>Units</u>	<u>Definition</u>
$\bar{\mu}$	dyne/cm <sup>2</sup>	Complex frame shear modulus
$\mu^*$	dyne/cm <sup>2</sup>	Imaginary part of frame shear modulus
$\mu$	dyne/cm <sup>2</sup>	Real part of frame shear modulus
$\nu_n$		Eigenvalue
$\rho$	g/cm <sup>3</sup>	Bulk density of sediment
$\rho_f$	g/cm <sup>3</sup>	Fluid density
$\rho_r$	g/cm <sup>3</sup>	Frame mineral constituent density
$\sigma_\phi$	phi	Graphic standard deviation of sediment grain size
$\phi(x,y,z)$	1/m	Velocity potential
$\omega$	1/sec	Radian frequency
$\nabla^2$		The Laplacian $\left[ \frac{\partial^2}{\partial x^2} + \frac{\partial^2}{\partial y^2} + \frac{\partial^2}{\partial z^2} \right]$
$\Delta_s$		Log decrement for shear vibration
$\Delta_E$		Log decrement for longitudinal vibration

## LIST OF FIGURES

<u>Figure</u>	<u>Page</u>
1. Three-Layer Fluid Model . . . . .	9
2. Data Collection System . . . . .	39
3. LC-10 Array Configuration--Daytona Beach Site . . . . .	41
4. Energy Calculation--Single Hydrophone . . . . .	45
5. Mode Amplitude and Array Processing . . . . .	48
6. Energy Calculation--Array Type Processing . . . . .	49
7. Geometrical Dispersion in Shallow Water . . . . .	51
8. Seismic-Refraction Relations . . . . .	55
9. Refracted Arrivals--Range-Time Plot . . . . .	56
10. Daytona Beach Test Area . . . . .	60
11. Depth and Sound Velocity Profiles--Daytona Beach Site 2 . . . . .	62
12. Depth Profiles--Daytona Beach Site 2 . . . . .	64
13. Relative Energy Levels--Daytona Beach Site 1, Leg E . . . . .	68
14. Relative Energy Levels--Daytona Beach Site 1, Leg F . . . . .	69
15. Daytona Beach Experimental and Model Dispersion--Site 1 . . . . .	70
16. Comparison of Experimental and Predicted Bottom Absorption--Daytona Beach Site 1 . . . . .	78
17. Removal of Higher Order Modes at 750 Hz--Daytona Beach Site 1, Range 1 km . . . . .	80
18. Fathometer Record--Daytona Beach Site 1, Leg E (5.6 - 7.4 km) . . . . .	82
19. Relative Energy Levels--Daytona Beach Site 2, Leg J . . . . .	85
20. Daytona Beach Experimental and Model Dispersion--Site 2 . . . . .	89
21. Comparison of Experimental and Predicted Bottom Absorption--Daytona Beach Site 2 . . . . .	94
22. Corpus Christi Test Area . . . . .	100

## LIST OF FIGURES (continued)

<u>Figure</u>		<u>Page</u>
23.	Depth Profile--Corpus Christi, Long-Range Leg . . . . .	101
24.	Relative Energy Levels--Corpus Christi, Short-Range Data .	103
25.	Relative Energy Levels--Corpus Christi, Long-Range Data . .	106
26.	Corpus Christi Bottom Model . . . . .	108
27.	Comparison of Experimental and Predicted Bottom Absorption--Corpus Christi . . . . .	115
28.	Panama City Test Sites . . . . .	118
29.	Comparison of Experimental and Predicted Bottom Absorption--Panama City . . . . .	130
30.	Depth and Sound Velocity Profiles--Scotian Shelf . . . . .	135
31.	Bottom Structure--Scotian Shelf . . . . .	140
32.	Comparison of Experimental and Predicted Transmission Loss--Scotian Shelf, 38 m Depth . . . . .	145
33.	Comparison of Experimental and Predicted Transmission Loss--Scotian Shelf, 79 m Depth . . . . .	146
34.	Contour for $\eta_x$ Integration . . . . .	173

## LIST OF TABLES

<u>Table</u>	<u>Page</u>
1. Absorption Regression Equations . . . . .	31
2. Test Sites and Bottom Types . . . . .	35
3. Mode-Attenuation Coefficients ( $\delta$ )--Site 1, Daytona Beach .	67
4. Energy Distribution ( $\gamma$ ) and Bottom-Absorption Coefficients ( $\alpha_A$ )--Site 1, Daytona Beach . . . . .	72
5. Site 1 Grab-Sample Data--Daytona Beach . . . . .	74
6. Biot Sediment Model Parameters--Site 1, Daytona Beach . . .	76
7. Predicted Bottom Absorption ( $\alpha_A$ )--Daytona Beach . . . . .	77
8. Mode-Attenuation Coefficients ( $\delta$ )--Site 2, Legs G and H, Daytona Beach . . . . .	84
9. Mode-Attenuation Coefficients ( $\delta$ )--Site 2, Leg J, Daytona Beach . . . . .	86
10. Summary of Seismic-Refraction Work--Site 2, Daytona Beach .	88
11. Energy Distribution ( $\gamma$ ) and Bottom-Absorption Coefficients ( $\alpha_A$ )--Site 2, Daytona Beach . . . . .	90
12. Grab-Sample and Core Data--Site 2, Daytona Beach . . . . .	92
13. Sediment Model Parameters--Site 2, Daytona Beach . . . . .	93
14. Predicted Sediment Absorption ( $\alpha_A$ )--Site 2, Daytona Beach .	93
15. Power-Law Fits to Bottom-Absorption Coefficients ( $\alpha_A$ )--Sites 1 and 2, Daytona Beach . . . . .	97
16. Short-Range Mode-Attenuation Coefficients ( $\delta$ )-- Corpus Christi . . . . .	104
17. Long-Range Mode-Attenuation Coefficients ( $\delta$ )-- Corpus Christi . . . . .	107
18. Seismic-Refraction Data--Corpus Christi . . . . .	109
19. Energy Distribution ( $\gamma$ ) and Bottom-Absorption Coefficients ( $\alpha_A$ )--Corpus Christi . . . . .	111



## LIST OF TABLES (continued)

<u>Table</u>	<u>Page</u>
20. Core Data-Maximum and Minimum Grain Sizes--Corpus Christi .	112
21. Biot Sediment Model Parameters and Predicted Bottom Absorption ( $\alpha_A$ )--Corpus Christi . . . . .	114
22. Mode-Attenuation Coefficients ( $\delta$ )--Panama City . . . . .	121
23. Other Bottom Models for Panama City . . . . .	122
24. Environmental Models--Legs C and D, Panama City . . . . .	124
25. Energy Distribution ( $\gamma$ ) and Bottom-Absorption Coefficients ( $\alpha_A$ )--Legs C and D, Panama City . . . . .	126
26. (a) Biot Sediment Model Parameters--Panama City . . . . .	128
(b) Predicted Bottom Absorption ( $\alpha_A$ )--Panama City . . . . .	128
27. Power-Law Fits to Bottom-Absorption Coefficients ( $\alpha_A$ )-- Panama City . . . . .	131
28. Seabed Parameters--Scotian Shelf . . . . .	141
29. Effect of Methane Concentration . . . . .	144
30. (a) Bottom Parameters for Sensitivity Study--Panama City Leg C . . . . .	155
(b) Sensitivity to Bottom Parameters--Panama City Leg C .	155
31. Data Summary . . . . .	158

## ACKNOWLEDGMENTS

The author wishes to express his gratitude to Dr. Suzanne T. McDaniel for the advice and guidance that she provided throughout this study. Her interest and the many hours spent discussing the thesis are gratefully acknowledged. The author is also indebted to Dr. Robert W. Farwell and the other members of his doctoral committee for their suggestions in the writing of this thesis. The grain-size data provided by Dr. Lewis King of Bedford Institute of Oceanography, Dartmouth, Nova Scotia, and Dr. Orrin Pilkey, Duke University, are greatly appreciated. The author also appreciates the discussions and assistance provided by co-workers Louis Rubano, Jess Rollin, and Isabelle Sechrist.

This research was performed at the Applied Research Laboratory of The Pennsylvania State University under contract with the Naval Sea Systems Command.

## CHAPTER I

### INTRODUCTION

The transmission of sound in the ocean has been studied for many years. These studies have frequently been directed toward the measurement and analysis of the ways in which the sound waves are attenuated as they propagate out from the source of acoustic energy. In spite of this effort, many problems remain unsolved. This study attempts to expand the body of knowledge related to one aspect of the attenuation problem.

Normal-mode theory has been most successful in describing qualitative propagation effects for range-invariant, shallow-water environments. Given the relatively simple assumptions of the theory, comparisons of experimental and calculated propagation loss do not always correlate well. Weston (1967) recognized this problem and suggested such reasons as boundary-related losses and losses of biological origin. Boundary losses, in particular those related to the seabed, are the primary concern in this study.

The work of Pekeris (1948) was probably the first attempt to explain shallow-water propagation in terms of normal-mode theory. Perturbations of the basic theory, to account for boundary losses, were introduced by Kornhauser and Raney (1955), and Tolstoy (1958). Most recently, the theory has been successfully compared with experimental propagation results by Kibblewhite and Denham (1966), Ferris (1972), and Ingenito (1973).

At-sea measurements and model tank experiments by Eby et al. (1960) have demonstrated the validity of the theory and its modification for lossy bottoms.

As can be seen from this discussion, the theory and its modification for lossy bottoms have been shown to work. However, suppose it is desired to predict propagation loss for an area where a limited quantity of bottom information such as bottom type (i.e., sand, mud, etc.) and historical sound-velocity information is available. The question arises: Is it possible to predict modal-attenuation coefficients and sufficient sub-bottom information so that transmission loss may be predicted through the use of a normal-mode model? The answer to this question is heavily dependent upon our ability to predict bottom absorption, a topic to be addressed next.

Volume absorption in the sediment is generally the dominant loss mechanism for flat gravel, sand, or mud bottoms. The physical basis for this loss and mathematical models describing propagation in a fluid-filled porous sediment have been proposed by Morse (1952), Biot (1956, 1962), Brutsaert (1964), and Walton (1977). Generally, two sources of dissipation have been considered; that is, viscous losses due to fluid movement within the skeletal frame and friction losses due to movement between particles within the frame itself. The work of Biot and, more recently following his theory, the work of Stoll and Bryan (1970), and Stoll (1974, 1977, 1979) have found the greatest acceptance of the mathematical theories. The work of Hamilton (1972, 1974), mostly of an empirical nature, has also received some acceptance for predicting absorption values.

In this study, the determination of volume absorption in the sediment is approached from two aspects. First, bottom absorption is obtained as a function of frequency from transmission loss data and calculated mode-attenuation coefficients. Second, using data from grab-sample and core analyses as input to the sediment models of Biot and Hamilton, bottom absorption is calculated as a function of frequency. After establishing, by comparison with acoustic data, that the sediment model can be used to predict bottom absorption, the sediment model and other seabed information is used in a normal-mode model to predict transmission loss in test areas where comparative data is available.

Without adequate experimental data, the study would be impossible. Fortunately, propagation data is available for experiments performed off the Florida and Texas coasts, and one experiment performed on the Scotian Shelf. These sites, in general, are well-documented with regard to the sediments and sub-bottom structure present.

Following the introductory material presented in this chapter, a discussion of normal-mode theory and the theory relating to propagation in fluid-filled porous media is presented in Chapter II. The implementation of these theories for solution on a digital computer is discussed and, finally, the modification of the basic normal-mode program for range-dependent propagation modeling (i.e., adiabatic normal-mode theory) is also considered in Chapter II. The normal-mode models are based on the computer model of Miller and Ingenito (1975).

The experimental procedures are discussed in Chapter III. The geometry, type of experiments, water depth, bottom types, etc., relating to each of the experimental at-sea programs is first discussed.

A description of the data collection system follows and includes a brief system description, bandwidths, hydrophone data, etc. The analysis procedures described next include operations performed with the Hewlett-Packard Fourier Analyzer and a description of dispersion analysis and seismic-refraction analysis. Finally, the grab-sample and core analyses performed by several different laboratories are discussed.

The analysis of experimental data begins in Chapter IV. The data considered in this chapter is from a test site off the coast of Daytona Beach, Florida, with a nominal water depth of 19 m. Also discussed in this chapter are experimental data from a second site off Daytona Beach having a water depth of 30 m. Experimental data from Corpus Christi, Texas, for a water depth of 30 m are analyzed in Chapter V. Chapter VI discusses data for two sites with nominal water depths of 18 and 30 m off the coast of Panama City, Florida.

The analysis in Chapters IV through VI serves to establish the validity of the sediment model for predicting bottom absorption. In Chapter VII, transmission loss predictions are made with bottom absorption obtained from the sediment models for a region off the coast of Nova Scotia in a range-dependent environment. In Chapter VIII, the study is summarized, and conclusions are made concerning the validity and failings of the study.

## CHAPTER II

### BACKGROUND

#### 2.1 Normal-Mode Theory

In the study of sound-transmission problems, the solutions generally fall into two categories based primarily upon water depth. Deep-water problems consider those situations where the water depth is greater than approximately 100 fathoms. Solutions to these problems are frequently obtained in terms of rays perpendicular to the wavefronts which emanate from the source. Shallow-water problems are then concerned with water depths of less than 100 fathoms and frequently result in solutions in terms of the normal modes set up in the water column along the transmission path. As might be expected, the separation between the two types of solutions is not that clear; for example, very low-frequency waves in deep water may yield to normal-mode solutions, and conversely, high-frequency waves in shallow water will obey ray theory. Generally, ray theory is applied where the wave length is a small fraction of the water depth. For the water depths of interest in this study (less than 33 fathoms), both types of solutions have some validity since the frequencies range from 2 to 1000 Hz. The emphasis in this study will be upon normal-mode solutions, although the ray analogy will frequently be used to explain normal-mode theory.

A solution in terms of normal modes is an exact solution to the wave equation for certain simple boundary-value problems. If the boundary conditions are those of a free surface and a rigid bottom, we have perfect reflection at the surface and bottom, and an ideal

waveguide results. The solution in the depth coordinate consists of standing-wave patterns (e.g., as in an organ pipe), or the normal modes of vibration of the system. For shallow-water propagation in the ocean, the problem is more complex; however, the same concepts apply. The first and simpler of the normal-mode models of the ocean was that of Pekeris (1948). This model consists of an isovelocity water layer over another fluid layer of infinite depth. Densities and compressional sound speeds are specified in each layer, and the water depth as well as the other parameters must be invariant with range. The solution indicates that the net propagation of energy is along the channel axis and that the velocity of this propagation will be a function of frequency.

To elaborate on the normal-mode concept, we can think of shallow-water propagation in terms of ray theory. The singular characteristic which distinguishes shallow-water from deep-water propagation is the frequency interaction of the sound field with the ocean surface and bottom. If we consider propagation at some distance from the source, the wave fronts will strike the surface and bottom as plane waves. For each encounter, the wave will undergo a phase shift at the surface and bottom. The formation of standing waves requires constructive interference between consecutive downgoing (or upgoing) rays striking the bottom at the same angle. For this to occur, the total phase shift due to surface, bottom, and path length must be some multiple of  $360^\circ$ . Since the phase shift due to the path length is a function of frequency, a set of discrete (harmonically related) frequencies will satisfy the above criteria for any incidence angle.



Other frequencies will result in destructive interference for this incidence angle. Thus, the standing-wave patterns set up in the sound channel are referred to as the normal modes of the channel. The propagation velocity along the channel axis, termed the phase velocity, is dependent upon the incidence angle through a simple relation; thus, a particular phase velocity is associated with a group of discrete frequencies. The multiple reflections and consequent interference which develops thus causes a variation in propagation velocity with frequency, termed geometrical dispersion. With a similar argument, the combined effects of all the preferred angles for a particular frequency may be summed to create the mode-amplitude distribution in the water column. That is, for any frequency, the pressure amplitude will vary with depth in a predictable manner, this variation being different for each mode. The only loss predicted by the theory is inversely proportional to the square root of the range, termed cylindrical spreading.

2.1.1 Formal development of normal-mode theory. In many texts [Officer (1958), Tolstoy and Clay (1966)], the formal derivation of the normal-mode solution starts with the general wave equation,

$$\nabla^2 \phi = \frac{1}{c^2} \frac{\partial^2 \phi}{\partial t^2} ,$$

for the velocity potential  $\phi$ . If the time dependence is harmonic, that is,

$$\phi(t) = e^{-i\omega t} ,$$

then the Helmholtz equation which results is only a function of the space variables, giving:

$$\nabla^2 \phi + \frac{\omega^2}{c^2} \phi = 0 .$$

At this point, many derivations assume a cylindrical coordinate system  $(r, \theta, z)$ , with symmetry in the  $\theta$  coordinate, and assuming range independent parameters, the separation of variable approach may be used to obtain equations in  $r$  and  $z$ . The equation in  $r$  is Bessel's equation which leads to a Bessel function solution (for outward propagation of energy) for the  $r$  coordinate. The  $z$  solution is that of an ordinary second-order differential equation with constant coefficients. It is assumed that the sound velocity  $c$  is a function of only the depth coordinate. The boundary conditions for the Pekeris model are that of a pressure release surface at the air-water interface, where the  $z$  dependent solution must go to zero, and continuity of pressure and the vertical velocity component across the water-bottom boundary. Within the bottom half-space, the solution must decay to zero with increasing depth.

The source conditions are applied by deriving a frequency-dependent constant which matches the spherical point source to the complete cylindrical solution of the wave equation. As the complete solution involves integration of the product solutions for  $r$  and  $z$  in the  $k$  (wave number) plane for multi-valued  $k$ , complex integration using Cauchy's residue theorem is required. The residue sum for this integration in the complex plane then yields the normal modes.

A more direct derivation of the normal-mode equation is presented by Ingenito et al. (1978). The Pekeris model may be used, but to provide a better introduction for the computer model, the three-layer normal-mode model in Figure 1 will be assumed. In this model, all layers are assumed to be fluid layers; hence, compressional velocities  $[c_1(z), c_2(z), c_3]$  are assumed throughout. A cartesian coordinate

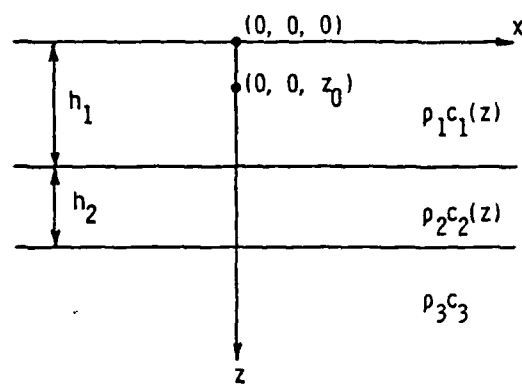


Figure 1. Three-Layer Fluid Model

system will be used for most of the derivation, and a transformation to cylindrical coordinates will be applied near the end. The ocean surface is assumed to lie in the  $x, y$  plane, while the  $z$  coordinate increases with depth.

Assume a unit strength harmonic point source of angular frequency  $\omega$  at a depth  $z_0$  as shown. If the time dependence is dropped, the velocity potential  $\phi(x, y, z)$  must satisfy the equation

$$\nabla^2 \phi + \left[ \frac{\omega}{c(z)} \right]^2 \phi = -\delta(x)\delta(y)\delta(z - z_0) \quad (1)$$

The dimensional requirements of Equation (1) may be satisfied by noting that in the absence of boundaries,  $\phi$  will have the solution  $\phi = \frac{1}{4\pi R} e^{ikR}$ , where  $R = \sqrt{x^2 + y^2 + z^2}$ , and both sides of Equation (1) will have the same dimensions. We may then find  $\phi$  at any point  $(x, y, z)$  relative to the velocity potential at a unit distance.

The boundary conditions to be satisfied are those stated earlier. That is, at the surface,

$$\phi(x, y, 0) = 0 \quad (2)$$

to satisfy the pressure-release condition. At the boundary between medium 1 and 2, where  $z = H_1$ , we have:

$$\rho_1 \phi^{(1)}(x, y, H_1) = \rho_2 \phi^{(2)}(x, y, H_1) \quad (3)$$

to satisfy continuity of pressure, and

$$\left. \frac{\partial \phi^{(1)}}{\partial z} \right|_{z=H_1} = \left. \frac{\partial \phi^{(2)}}{\partial z} \right|_{z=H_1} \quad (4)$$

to satisfy the condition on the continuity of the vertical component of velocity. At  $z = H_1 + H_2$ , in a similar manner, the conditions are:

$$\rho_2 \phi^{(2)}(x, y, H_1 + H_2) = \rho_3 \phi^{(3)}(x, y, H_1 + H_2) \quad (5)$$

and

$$\left. \frac{\partial \phi^{(2)}}{\partial z} \right|_{z=H_1+H_2} = \left. \frac{\partial \phi^{(3)}}{\partial z} \right|_{z=H_1+H_2} . \quad (6)$$

The notations  $\phi^{(1)}$ ,  $\phi^{(2)}$ , and  $\phi^{(3)}$  identify the velocity potential in the three regions of Figure 1. The two final conditions are that radiation is assumed outward from the source, and the field must decay to zero in the half-space of medium 3.

To solve Equation (1), the double Fourier transform will be used.

That is,

$$\phi(x, y, z) = \frac{1}{(2\pi)^2} \int_{-\infty}^{\infty} \int_{-\infty}^{\infty} U(\eta_x, \eta_y, z) e^{i(\eta_x x + \eta_y y)} d\eta_x d\eta_y \quad (7)$$

and

$$U(\eta_x, \eta_y, z) = \int_{-\infty}^{\infty} \int_{-\infty}^{\infty} \phi(x, y, z) e^{-i(\eta_x x + \eta_y y)} dx dy . \quad (8)$$

Substituting Equation (7) into Equation (1) yields an integro-differential equation which may be solved using Equation (8) and the shifting property of the Dirac Delta function. Thus, noting that  $\psi^2 = \eta_x^2 + \eta_y^2$ , and  $k^2(z) = \omega^2/c^2(z)$ , we have:

$$\frac{d^2 U}{dz^2} + [k^2(z) - \psi^2] U = -\delta(z - z_0) , \quad (9)$$

a non-homogeneous differential equation for  $U(\eta_x, \eta_y, z)$ . To solve Equation (9), it is assumed that  $U_n(z)$  is the eigenfunction and that  $k_n$  is the eigenvalue of the following equation:

$$\frac{d^2 U_n}{dz^2} + [k^2(z) - k_n^2] U_n = 0 , \quad (10)$$

where both must satisfy the boundary conditions (2) through (6).

Letting  $v_n^2 = k^2(z) - k_n^2$ , and following the procedure of Clay and Medwin (1977), we find that for the  $n^{\text{th}}$  and  $m^{\text{th}}$  eigenfunctions to satisfy the boundary conditions in each layer, the following condition must hold:

$$\int_0^\infty \rho U_n(z) U_m(z) dz = \delta_{mn} . \quad (11)$$

That is, the eigenfunctions  $U_n(z)$  form an orthonormal set satisfying Equation (11), where  $\rho$  will assume the value specified in each layer.

At this point, the meaning of  $k_n$  and its effect on the eigenvalue spectrum ( $v_n$ ) must be considered. Physically,  $k_n = \frac{\omega}{v_n}$ , where  $v_n$  is the phase velocity, and  $k_n$  is the wave number in the direction of propagation. The  $v_n$  spectrum may be either discrete or continuous. If we assume that  $c_3 > \max [c_1, c_2]$ , then the spectrum will be discrete if

$$c_3 > v_n > \max [c_1(z), c_2(z)] . \quad (12)$$

The discrete spectrum represents energy which is trapped in the sound channel due to perfect reflection at the surface and bottom. If Equation (12) is not satisfied, the spectrum will be continuous, but these modes will be highly damped with increasing range since they occur due to partial reflection at the bottom. Thus, the continuous modes are important at only very short ranges and will hence be neglected in all further discussions.

Equation (9) may now be solved by assuming a solution composed of an expansion of the eigenfunctions; that is,

$$U(\eta_x, \eta_y, z) = \sum_n A_n(\eta_x, \eta_y) U_n(z) \quad . \quad (13)$$

The constant  $A_n(\eta_x, \eta_y)$  may be evaluated using the orthonormal relation in Equation (11) as:

$$A_n(\eta_x, \eta_y) = \frac{\rho(z_o) U_n(z_o)}{\psi^2 - k_n^2} \quad . \quad (14)$$

The solution to Equation (9) is then:

$$U(\eta_x, \eta_y, z) = \rho(z_o) \sum_n \frac{U_n(z) U_n(z_o)}{\psi^2 - k_n^2} \quad . \quad (15)$$

Thus, transforming back to the space domain,

$$\phi(x, y, z) = \frac{\rho(z_o)}{(2\pi)^2} \int_{-\infty}^{\infty} \int_{-\infty}^{\infty} \sum_n \frac{U_n(z_o) U_n(z)}{\psi^2 - k_n^2} e^{i(\eta_x x + \eta_y y)} d\eta_x d\eta_y \quad . \quad (16)$$

In order to solve Equation (16), we must evaluate the integral

$$I = \int_{-\infty}^{\infty} \int_{-\infty}^{\infty} \frac{e^{i(\eta_x x + \eta_y y)}}{\psi^2 - k_n^2} d\eta_x d\eta_y$$

in terms of polar coordinates  $(r, \theta)$ . This is done in Appendix A and yields the result that

$$I = i\pi^2 H_o^{(1)}(k_n r) \quad .$$

The desired relation for the velocity-potential solution in cylindrical coordinates is thus:

$$\phi(r, z) = \frac{1}{4} \rho(z_o) \sum_n U_n(z_o) U_n(z) H_o^{(1)}(k_n r) \quad . \quad (17)$$

In Equation (17),  $U_n(z_o)$  is the mode-amplitude function at the source.  $U_n(z)$  is the mode-amplitude function at the receiver, and  $H_o^{(1)}(k_n r)$  is the zero-order Hankel function of the first kind. At long ranges from the source, the Hankel function may be replaced by its asymptotic approximation. That is,

$$H_o^{(1)}(k_n r) \sim \sqrt{\frac{2}{\pi k_n r}} e^{i(k_n r - \frac{\pi}{4})}.$$

The velocity potential as a function of time at long ranges can then be expressed as:

$$\phi(r, z) e^{-i\omega t} = i\rho(z_o) \sqrt{\frac{1}{8\pi r}} e^{-i\frac{\pi}{4}} \sum_n \frac{U_n(z_o) U_n(z)}{\sqrt{k_n}} e^{i(k_n r - \omega t)}. \quad (18)$$

As can be seen, the field at a range  $r$  and a depth  $z$  diminishes as  $1/\sqrt{r}$  and propagates with a phase velocity of  $\omega/k_n$ . A broadband source such as an explosive charge will contain many frequencies with propagation velocities  $u_n$  (the group velocity) related to the phase velocity by:

$$u_n = \frac{\partial \omega}{\partial k_n}.$$

The pressure field is related to the velocity potential by the equation

$$p = \rho \frac{\partial \phi}{\partial t},$$

so that the variations in the pressure field with depth due to the source are proportional to  $U_n(z_o)$  and those due to the receiver are proportional to  $U_n(z)$ .



The computer implementation of the normal-mode calculation is based on solving the eigenvalue problem in each of the three layers. This requires solving the differential equation, i.e., Equation (10), for the boundary conditions at the upper and lower interfaces. In reality, the differential equations are replaced by difference equations for a numerical solution and the sound-speed profile  $c(z)$  is approximated so that each of the layers is divided into many layers, each having a constant sound speed. The solution is initiated in the third layer where an exact solution involving only one unknown constant may be written [from the requirement that  $U_n^{(3)}(z) \rightarrow 0$  as  $z \rightarrow \infty$ ]. A trial value of  $k_n$  is assumed, and  $U_n^{(3)}$  and its derivatives are calculated. The boundary conditions are then satisfied, and the solution proceeds upward within each layer until the surface is reached where  $U_n^{(1)}(0)$  must be zero or less than some pre-selected small number. The procedure is repeated until this last condition is satisfied.

The transmission loss may be calculated from the solution obtained for  $U_n$  and  $k_n$ . That is, the modal pressure sum may be obtained from Equation (18), and then the energy in each mode calculated. The incoherent transmission loss expressed in decibels for unit source strength may then be expressed as:

$$TL = 10 \log_{10} \left\{ 2\pi\rho^2(z_o) \sum_n \left[ \frac{U_n(z_o)U_n(z)}{\sqrt{k_n r}} \right]^2 \right\}, \quad (19)$$

where  $U_n(z)$  and  $k_n$  are evaluated numerically at the receive point of interest.

Certain modeling situations involving near-surface, consolidated (and maybe some semi-consolidated) bottom structures with high shear velocities require a solid-bottom model as opposed to the fluid model just described. Ingenito et al. (1978) derives this type of model, replacing the fluid half-space (layer 3) with a solid half-space. The primary difference in the solution is that two eigenfunctions must now be determined in the half-space, one for the compressional wave and one for the shear wave. The boundary conditions at  $z = H_1 + H_2$  also involve the shear eigenfunction and must force this solution to become zero within the upper two fluid layers. A complete description of the implementation of both fluid and solid normal-mode computer models is presented by Miller and Ingenito (1975).

2.1.2 Loss mechanisms. In the preceding discussion, the assumption was made that for large  $r$ , all of the energy was trapped within the sound channel. This resulted from the assumption of perfect reflection at the water-sediment interface. The model thus predicts transmission loss due only to geometrical spreading (i.e.,  $1/\sqrt{r}$  or cylindrical spreading). As frequently happens, however, this model of the ocean and bottom is too simple. A physically realistic ocean bottom will absorb energy from all the incident rays; shear waves will be generated due to the incident compressional waves; and finally, bottom roughness will cause energy to be scattered at unfavorable angles resulting in attenuation. The net effect is that, due to these mechanisms, propagation losses in the real ocean environment are much greater and have more variability than the basic theory predicts.

As noted, three loss mechanisms associated with the bottom have been identified; that is, absorption of compressional waves, scattering losses, and conversion of compressional waves to shear waves. Losses due to bottom absorption were noted in Chapter I; and, since they are of primary interest in this study, they will be discussed at length near the end of this chapter. The other loss mechanisms are described briefly in the following paragraphs.

Loss due to scattering can be viewed as resulting from the transfer of energy between propagating normal modes due to the roughness of the ocean floor. McDaniel (1977) has analyzed this loss mechanism and shows that, for the higher frequencies (greater than 200 Hz), the loss due to mode conversion can be of the same magnitude as volume absorption. The loss results from the transfer of energy to higher-order modes, which in turn have larger attenuation coefficients resulting in greater loss than if conversion were not present. A sloping bottom may also cause this same type of loss (i.e., mode conversion); however, Pierce (1965) has shown that if the water depth varies slowly with range, mode conversion may be neglected. The basic normal-mode theory may be modified to handle this situation. The modified theory is termed adiabatic normal-mode theory and is discussed in the latter part of this chapter.

Loss due to conversion to shear waves will be present for those sediments capable of supporting shear waves. Hamilton (1969) has found that most porous, marine sediments will support shear waves. The loss due to conversion to shear waves is treated by Officer (1958), Eby et al. (1960), and Williams and Eby (1962) by deriving a plane-wave reflection coefficient for the case of a rigid bottom, and then using

this coefficient to include a loss per bounce in the Pekeris model. For shear velocities on the order of 400 m/sec or greater, this loss mechanism may be the largest of the three.

In the model for normal-mode propagation, all layers are considered lossless. In order to account for the attenuation associated with real ocean sediments, the bottom layers must be modified to represent a lossy medium. This is done, following Kornhauser and Raney (1955), and Tolstoy (1958), by multiplying the basic solution [Equation (18)] by an exponential attenuation factor,  $e^{-\delta_n r}$ , where  $\delta_n$  is the mode-attenuation coefficient. The modal sum for the velocity potential then becomes:

$$\phi(r,z)e^{-i\omega t} = i\rho(z_0) \left[ \frac{1}{8\pi r} e^{-i\frac{\pi}{4}} \right] \times \left\{ \sum_n \frac{U_n(z_0)U_n(z)}{\sqrt{k_n}} e^{i[(k_n + i\delta_n)r - \omega t]} \right\} \quad (20)$$

It may be shown [Kornhauser and Raney (1955), and Ingenito (1973)] that  $\delta_n$  can be equated, if we assume all the attenuation is due to the absorbing bottom, to the product of a bottom-absorption coefficient  $\alpha_A$  and a modal energy ratio,  $\gamma_n$ , equal to the fraction of the total energy trapped in the bottom. That is, for the second layer,  $\delta_n = \gamma_n^{(2)} \alpha_A$ , where

$$\gamma_n^{(2)} = \frac{\frac{\rho_2 \omega}{k_n} \int_{H_1}^{H_1+H_2} \frac{|U_n^{(2)}|^2}{c_2(z)} dz}{\rho \int_0^\infty \frac{|U_n|^2}{c(z)} dz} \quad (21)$$

With this background, the scope of the study can be narrowed to specify one aspect of the problem. That is, if the mode-attenuation coefficient for any mode (e.g., the first mode) is known, and if a computer implementation of the normal-mode equations is available so that  $\gamma_1$  may be calculated, then the bottom-absorption coefficient may be calculated as well.

In general, the experimental data obtained at sea will yield transmission loss as a function of range. To generate this information, received energies are calculated at a particular frequency and subtracted from known source levels at each range point of interest, the difference being the transmission loss. The mode-attenuation coefficient may be calculated for any mode and frequency by (1) first isolating the received energy in that mode, (2) calculating the transmission loss for the mode, (3) applying a correction for cylindrical spreading losses, and (4) computing the slope of the corrected transmission loss versus range curve. The computed slope, with units of dB/km, is the mode-attenuation coefficient for the isolated mode and the frequency of interest. A summary of the research documenting the use of these techniques is presented in the following paragraphs.

2.1.3 Previous shallow-water studies. Although the study of mode attenuation or bottom loss was not the primary concern, the work of Worzel and Ewing (1948) was probably the first experimental work at sea with explosive charges to be tested against normal-mode theory. During the same period, Pekeris (1948) had developed normal-mode theory for sound-propagation problems in shallow water and was able to explain

many of the observed results of Worzel and Ewing with the theory. Eby et al. (1960) performed model experiments with a water layer over a Hycar rubber bottom. Over the range of test frequencies, 55 to 600 kHz, experimental mode-attenuation coefficients compared well with theory at the low end of the range, but toward the upper end, losses attributed to conversion to shear waves caused higher than expected attenuation. Tolstoy (1958) performed normal-mode experiments in 22.6 m of water off the Atlantic coast and found that mode-attenuation coefficients for the first mode ranged from 3.57 to 5.13 dB/km over a frequency range of 88 to 148 Hz. Kibblewhite and Denham (1966) performed experiments in water depths ranging from 91 to 274 m off the New Zealand coast. Their results led them to conclude that the attenuation was dominated by absorption and conversion to shear at low frequencies (less than 50 Hz), and that scattering dominated around 100 Hz (where an attenuation minimum occurred) and also at higher frequencies. More recently, Ferris (1972) and Ingenito (1973) collaborated on measurements performed in the Gulf of Mexico at frequencies of 400 and 750 Hz. They obtained good agreement between theoretical and experimental mode-amplitude distributions for the first two modes along a constant-depth (31 m) propagation path over a hard-sand bottom. Finally, Ingenito and Wolf (1976) made measurements off the Yucatan Peninsula along a constant-depth (30 m) track overlying a near-surface limestone layer. Conversion due to shear was found to be the dominant loss mechanism for this high-velocity layer (1900 m/sec compressional and 1000 m/sec shear).

2.1.4 Range-dependent modeling. A basic assumption involved in the derivation of the normal-mode equation [Equation (18)] was that all parameters were independent of range, permitting the separation of range and depth solutions. While this assumption is not unduly restrictive, there being many situations where sound-velocity profiles, water depths, etc., do not vary substantially with range, it is often desirable to study propagation under range-dependent conditions. To apply normal-mode theory to these situations, the adiabatic approximation is used; that is, it is assumed that each normal mode propagates independently with no exchange of energy between modes (i.e., no mode coupling). As noted earlier, McDaniel (1977) found that losses due to mode coupling increased for the higher frequencies; hence, it is expected that use of the adiabatic approximation will be limited to the lower frequencies. The range-dependent calculation of transmission loss is then made using the range-independent model with the assumption that the modes adapt to the environment at the point of interest, i.e., locally, propagation is independent of range.

These assumptions have been tested in experimental work by Eby et al. (1960), and Ingenito et al. (1978), and treated theoretically by Pierce (1965). The range-dependent model may be implemented (Ingenito et al.) by modifying Equation (20) so that the modal wave number  $k_n$  and attenuation coefficient  $\delta_n$  are replaced by comparable quantities  $\bar{k}_n$  and  $\bar{\delta}_n$  which are averaged over the propagation path. That is,

$$\bar{k}_n = \frac{1}{r} \int_0^r k_n(r) dr$$

and

$$\bar{\delta}_n = \frac{1}{r} \int_0^r \delta_n(r) dr .$$

The expression for the incoherent transmission loss then becomes [following Equation (19)]:

$$TL = 10 \log_{10} \left\{ 2\pi\rho^2(z_o) \sum_n \left[ \frac{U_n(z_o)U_n(z)}{\sqrt{k_n r}} e^{-\bar{\delta}_n r} \right]^2 \right\} . \quad (22)$$

The procedure is then to specify parameters for the water and seabed at a number of range points along the propagation track. The range-independent model discussed previously is run at these range points and  $U_n(z_o)$ ,  $\bar{k}_n$ , and  $\bar{\delta}_n$  calculated. The receive function  $U_n(z)$  is calculated only at the zero range point. If ranges are required other than those at which the water and bottom parameters have been specified, interpolation of  $U_n(z_o)$  between specified range points is required.

## 2.2 Geoacoustic Models of the Ocean Bottom

In specifying models of the ocean bottom, the principal acoustic parameters of interest are the density, compressional and shear velocities, and the bottom-absorption coefficient. Related to these acoustic properties of the model, by largely empirical formulations, are engineering properties such as porosity, grain-size and distribution, and the elastic constants (such as the bulk modulus and rigidity modulus). In addition, a complete geoacoustic model details the thickness and properties of the sediment and rock layers down to a depth which is dependent on the lowest frequency of interest.



Several different techniques are required to formulate such a model. For the deeper layers, the required acoustic parameters must be determined by indirect methods such as seismic-refraction and dispersion analysis, reflection profiling, or literature surveys. The surficial sediments may be sampled through the use of corers and grab samples. Analysis of the cores or grab samples will provide many of the engineering properties such as grain-size data (and porosity for cores). With this data, absorption coefficients may be predicted using a sediment model for the upper few meters of the seabed.

2.2.1 Sediment model of Biot. As discussed in Chapter I, the work of Biot (and more recently, Stoll) and Hamilton has dominated the literature with regard to sound absorption in marine sediments. In the following paragraphs, the model of Biot will be derived, using Stoll's development, and the work of Hamilton discussed. In Chapter III, the experimental techniques (such as seismic-refraction and dispersion analysis) for determining sub-bottom parameters will be discussed.

The theory developed by Biot is a comprehensive description of the response of linear, porous materials containing compressible fluid. Stoll clarifies and presents an abbreviated version of Biot's development forming the basis for the following discussion.

The development of Stoll begins with a pair of coupled differential equations derived by Biot for the motion of the skeletal frame and the motion of the viscous pore fluid relative to the frame. That is, for the frame,

$$\nabla^2(\bar{H}\epsilon - \bar{C}\zeta) = \frac{\partial^2}{\partial t^2}(\rho_e - \rho_f\zeta) \quad , \quad (23)$$

and for the fluid relative to the frame,

$$\nabla^2 (\bar{C}e - \bar{M}\zeta) = \left[ \frac{\partial^2}{\partial t^2} (\rho_f e - m\zeta) \right] - \frac{\eta F}{\kappa} \frac{\partial \zeta}{\partial t} . \quad (24)$$

Solutions for  $e$ , the dilatational strain of the frame, and  $\zeta$ , the increment of fluid flow, are assumed to be of the form

$$e = A_1 e^{i(\omega t - \ell x)} \quad (25)$$

and

$$\zeta = A_2 e^{i(\omega t - \ell x)} . \quad (26)$$

If Equations (25) and (26) are substituted in Equations (23) and (24), two equations in  $A_1$  and  $A_2$  result. If solutions exist for  $A_1$  and  $A_2$ , it must hold that the determinant of the coefficients of  $A_1$  and  $A_2$  equals zero. Stoll's determinant relation then results as:

$$\begin{vmatrix} \bar{H}\ell^2 - \rho\omega^2 & \rho_f\omega^2 - \bar{C}\ell^2 \\ \bar{C}\ell^2 - \rho_f\omega^2 & m\omega^2 - \bar{M}\ell^2 - i \frac{\omega F \eta}{K} \end{vmatrix} = 0 . \quad (27)$$

A solution for the complex variable  $\ell$  will yield the absorption (the imaginary part) and phase velocity (the real part) for two types of compressional waves. A relation similar to Equation (27) will yield a comparable solution for the shear wave. The first compressional wave is the usual one associated with fluids; the second wave has lower velocity and is greatly attenuated. Recently, Plona (1980) observed the second wave at ultrasonic frequencies in a fluid-saturated porous medium consisting of water and sintered glass spheres. Only the first compressional wave is considered here.

If the determinant in Equation (27) is reduced, the following fourth-order complex equation is obtained:

$$a_1 \ell^4 + a_2 \ell^2 + a_3 = 0. \quad (28)$$

The constants  $a_1$ ,  $a_2$ , and  $a_3$  are complex and are defined as follows:

$$a_1 = \bar{C}^2 - \bar{H} \bar{M}, \quad (29)$$

$$a_2 = (\bar{H}m + \rho \bar{M} - 2\bar{C}\rho_f)\omega^2 - i \frac{\omega F \eta}{K} \bar{H} \quad (30)$$

and

$$a_3 = (\rho_f^2 - \rho m)\omega^4 + i \frac{\omega^3 F \eta}{K} \rho. \quad (31)$$

In Equations (29), (30), and (31),  $\rho$  is the saturated density;  $\rho_f$  is the density of the pore fluid;  $K$  is the sediment permeability;  $\eta$  is the fluid viscosity; and  $\omega$  is the radian frequency. The complex constants ( $\bar{C}$ ,  $\bar{H}$ , and  $\bar{M}$ ) are functions of fluid, frame, and frame material bulk moduli ( $k_f$ ,  $\bar{k}_b$ , and  $k_r$ , respectively) frame shear bulk modulus  $\bar{\mu}$ , porosity  $\beta$ , and a parameter  $m$  representing the tortuosity of the pore spaces. The constants are defined by Stoll as follows:

$$\bar{C} = \frac{k_r(k_r - \bar{k}_b)}{D - \bar{k}_b}, \quad (32)$$

$$\bar{H} = \frac{(k_r - \bar{k}_b)^2}{D - \bar{k}_b} + \bar{k}_b + \frac{4\bar{\mu}}{3} \quad (33)$$

and

$$\bar{M} = \frac{k_r^2}{D - \bar{k}_b}, \quad (34)$$

where

$$D = k_r \left[ 1 + \beta \left( \frac{k_r}{k_f} - 1 \right) \right] \quad (35)$$

In Equations (30) and (31), the term  $\frac{F\eta}{K}$  represents the frequency-dependent viscous effects through the correction factor  $F$  derived by Biot. The correction factor  $F$  is defined as a function of  $\kappa$ , where

$$F = F(\kappa) = \frac{1}{4} \frac{\kappa T(\kappa)}{1 - \frac{2T(\kappa)}{i\kappa}} \quad (36)$$

$$\kappa = a(\omega \rho_f / \eta)^{1/2} \quad (37)$$

and

$$T(\kappa) = \frac{\text{ber}'(\kappa) + i \text{bei}'(\kappa)}{\text{ber}(\kappa) + i \text{bei}(\kappa)} \quad (38)$$

The functions  $\text{ber}(\kappa)$  and  $\text{bei}(\kappa)$  are real and imaginary parts of the Kelvin function, and  $a$  is a pore-size parameter. The functions  $\text{ber}'(\kappa)$  and  $\text{bei}'(\kappa)$  are the derivatives of the Kelvin functions.

To account for the unknown nature of the pore size and shape, the parameters  $m$  and  $a$  are introduced. The parameter  $m$  is defined as:

$$m = \alpha \rho_f / \beta \quad ,$$

where  $\alpha$  equals one for a system of uniform pores with axes parallel to the pressure gradient and three for a random orientation of uniform pores. In practice,  $\alpha$  must be treated as an experimental parameter. The parameter  $a$  is related to pore size and permeability and will be discussed later. The essential difference between  $a$  and  $m$  is in their usage;  $m$  has an inertial effect on fluid flow, reducing this flow for the more random pore orientation;  $a$  affects the viscous

resistance to fluid flow and results in an increased attenuation for high frequencies.

The inelastic nature of the frame is included in the model by making the frame bulk modulus  $k_b$  and the frame shear modulus  $\mu$  complex:

$$\bar{k}_b = k_b + ik_b^*$$

and

$$\bar{\mu} = \mu + i\mu^* \quad (39)$$

The real and imaginary components of  $\bar{k}_b$  are calculated by Stoll and Bryon (1970) as:

$$k_b = \frac{(\mu E - \mu^* E^*)(9\mu - 3E) + (\mu^* E + E^* \mu)(9\mu^* - 3E^*)}{(9\mu - 3E)^2 + (9\mu^* - 3E^*)^2}$$

and

$$k_b^* = \frac{(\mu^* E + E^* \mu)(9\mu - 3E) - (\mu E - \mu^* E^*)(9\mu^* - 3E^*)}{(9\mu - 3E)^2 + (9\mu^* - 3E^*)^2} \quad (40)$$

where  $E$  and  $E^*$  are the real and imaginary parts of the Young's modulus. The real part of the shear modulus  $\mu$  is calculated from experimental values of the shear velocity  $v_s$  obtained in experiments by Hardin and Richart (1963), and Hardin (1965) on the torsional vibration of a thin rod of the frame material. That is,

$$\mu = \rho v_s^2 \quad (41)$$

In the same experiments, values of the log decrement for shear  $\Delta_s$  were obtained, permitting the calculation of  $\mu^*$  from the basic equation for  $\Delta_s$  as

$$\Delta_s = \frac{\pi \mu^*}{\mu} \quad (42)$$

The Young's modulus for longitudinal vibration ( $E$ ) is calculated from experiments on the longitudinal vibration of a thin rod of the frame material (also, see Hardin and Richart, and Hardin), where  $E$  governs the longitudinal velocity of propagation  $v_E$  through the relation:

$$v_E = \sqrt{\frac{E}{\rho}} \quad (43)$$

The complex part  $E^*$  is obtained, in a manner similar to  $\mu^*$ , from the log decrement for longitudinal vibrations; that is,

$$\Delta_E = \frac{\pi E^*}{E} \quad (44)$$

Thus, in summary,  $\bar{k}_b$  and  $\bar{\mu}$  are obtained from experimental values of  $\Delta_s$ ,  $\Delta_E$ ,  $v_s$ , and  $v_E$ .

It is necessary to use several data sources in order to obtain the remaining input parameters. The bulk moduli of the fluid and frame material can be approximated from handbook data once the frame material is determined by core analysis. The porosity may be estimated from data in Hamilton (1972), where porosity is plotted as a function of mean grain-size if data from core analysis is unavailable. The fluid and frame material density may be obtained from a handbook, and the saturated density for the medium may then be calculated from the equation

$$\rho = (1 - \beta)\rho_r + \beta\rho_f \quad (45)$$

The absolute viscosity of the pore fluid  $\eta$  is a standard value (0.01 dyne-sec/cm<sup>2</sup> at 20°C) obtainable from a handbook.

In order to run the sediment model,  $k_r$ ,  $k_f$ ,  $\rho_f$ ,  $\rho_r$ ,  $K$ ,  $\gamma$ ,  $a$ ,  $v_E$ ,  $v_s$ ,  $\mu$ ,  $\beta$ ,  $\Delta_E$ , and  $\Delta_s$  must be supplied as input data, along with the desired frequency. The permeability  $K$  is calculated

from the sediment mean grain-size ( $d$  in mm) and phi deviation measures ( $\sigma_\phi$  in phi units) through the equation

$$K = 7.6d^2 e^{-1.31\sigma_\phi} \times 10^{-6} \quad (46)$$

from Krumbein and Monk (1942). The pore-size parameter  $a$  is then calculated from the relation

$$a = 3.87 \sqrt{K} \quad (47)$$

used by Stoll. The bulk modulus of the frame material  $k_r$  may be calculated using the Voigt-Reuss-Hill (VRH) averaging method described by Hamilton (1969). That is, if the frame is composed of several mineral types, an average value based on the fractional (by volume) concentration of each may be calculated from the equation (e.g., for a two-component frame):

$$k_r = \frac{k_1 k_2 (1 + v_1^2 + v_2^2) + v_1 v_2 (k_1^2 + k_2^2)}{2k_2 v_1 + 2k_1 v_2}, \quad (48)$$

where  $k_1$  and  $k_2$  are the bulk moduli of the two frame materials, and  $v_1$  and  $v_2$  are the fractional concentrations of each.

Finally, once the above parameters have been specified as input to the main program, computer subroutines are used to calculate the Kelvin functions, their derivatives and the roots of Equation (28).

2.2.2 Hamilton's approach to sediment absorption. The work of Hamilton, while mostly empirical, is based to some extent on linear viscoelastic theory as presented by Ferry (1961). The linear viscoelastic theory assumes that a complex ratio between stress and strain exists, and the damping or absorption is then represented by the phase

angle of the ratio. The absorption is predicted to vary as the first power of frequency.

The empirical work of Hamilton derives from many measurements on cores, artificial sediments, and short-range measurements. The results cover a frequency range of 5 Hz to 1 MHz, although the greatest amount of data is above 1 kHz. The work is described in Hamilton (1972, 1974, 1975). The technique for predicting the absorption of compressional waves is best described in Hamilton (1972), where regression equations for absorption as a function of mean grain-size and porosity are presented. The absorption data is presented as  $\alpha_A = K_A f^1$ , with  $K_A$  having units of dB/(m · kHz) and  $f$  expressed in kHz so that  $\alpha_A$  is in dB/m. In general, the absorption coefficient  $\alpha_A$  will be expressed in units of dB/km. As an example of the data given by Hamilton, Table 1 is extracted from the last reference. Given any mean grain-size and frequency, the absorption coefficient may be predicted according to Hamilton through the data in Table 1.

Data exists which appears to support both theories, the source of this data being measurements in cores, artificial sediments and in-situ measurements over very short ranges (1 to 2 m). The absorption measurements on cores and artificial sediments can be considered as measures of the intrinsic absorption in the sediment and rock material, while the in-situ measurements are considered as the "effective attenuation" measured from all sources.

Hamilton (1972 and 1975) has accumulated a very large body of data over a frequency range of 5 Hz to 1 MHz which appears to show nearly a linear dependence on frequency. This data includes both intrinsic measurements [McCann and McCann (1969), for example] and



TABLE 1  
 ABSORPTION REGRESSION EQUATIONS  
 [Hamilton (1972)]

$M_z$ Range (phi*)	Regression Equation for $K_A$
0 - 2.6	$K_A = 0.4556 + 0.0245 M_z$
2.6 - 4.5	$K_A = 0.1978 + 0.1245 M_z$
4.5 - 6.0	$K_A = 8.0399 - 2.5228 M_z + 0.20098 M_z^2$
6.0 - 9.5	$K_A = 0.9431 - 0.2041 M_z - 0.0117 M_z^2$

---

\*The phi unit is defined as  $M_z = -\log_2 d$ ,  
 where  $d$  is the mean grain diameter in mm.

effective attenuation measurements [Neprochnov (1971)]. Acoustic experiments conducted at sea by MacKenzie (1960) and Cole (1965) also appear to support Hamilton's theory.

Literature supporting the work of Biot and Stoll includes laboratory experiments by Busby and Richardson (1957), Shumway (1960), Nolle et al. (1963), Hampton (1967), and Johnston et al. (1979). The work of Hampton also reports measured velocity dispersion of approximately two percent over the frequency range of 5 to 200 kHz. Acoustic measurements reported by Ingenito (1973) indicate that attenuation varies as  $f^{1.75}$  with frequency.

## CHAPTER III

### EXPERIMENTAL PROCEDURES

#### 3.1 Background

In order to study the effects of sediment absorption on transmission loss, two types of information must be obtained experimentally. First of all, to measure the effectiveness of techniques developed for modeling the sediment and predicting its absorption, experimental sediment-absorption data must be available for the frequencies of interest. As discussed briefly in Chapter I, this experimental data is obtained by measuring the transmission loss in regions having a wide variety of bottom types. From the transmission-loss measurements, the attenuation attributable to sediment absorption may be assessed. Thus, the test sites and the methods used to obtain, process, and analyze the experimental data are of great importance. Secondly, the surficial sediments and sub-bottom structure must be well known so that sediment and sub-bottom modeling efforts will represent the bottom to the highest degree possible. Thus, good grab-sample and coring data are required to characterize the surficial sediments. Experiments, such as the seismic-refraction experiment, have been designed so that the data obtained will yield information on the sub-bottom structure. Analysis of the dispersive propagation effects provides another technique for characterizing the bottom parameters. Finally, reflection profiling may provide both surficial sediment data and evidence as to the shallow sub-bottom structure.

With this in mind, test sites were selected to provide a variety of sediment types; in most cases, regions were selected with constant depth and sloping bottoms having nominal water depths of 15 to 46 m. The Scotian Shelf test area was the one exception to these criteria, as a sloping bottom in deeper water was desired. The test sites selected are listed in Table 2 along with their general bottom type. As can be seen, a variety of bottom types are present.

In the following sections, the experimental geometry, sound sources, instrumentation, analysis system and procedures, and the source and types of sediment data used are discussed. This information, along with the theory discussed in Chapter II, provides the necessary background for understanding the analysis and comparisons of data in the later chapters.

### 3.2 At-Sea Experiments

From 1973 through 1978, experimental programs were conducted to measure the characteristics of acoustic waves propagating in shallow water. In addition, environmental measurements were made to determine seabed properties. Tests were performed at two different sites off Daytona Beach during the 1976 tests and at one site during the 1973 tests. Data is also reported for two sites off Panama City, one on the Scotian Shelf, and one off Corpus Christi.

The experiments were generally of three different types, all of which involved propagation over a track of constant depth and over a track from a source in deep water to a shallow-water receiver. Seismic-refraction experiments were designed to yield information about the sub-bottom structure. Short-range experiments were designed to

TABLE 2

## TEST SITES AND BOTTOM TYPES

<u>Test Site</u>	<u>Date of Tests</u>	<u>Bottom Type</u>
Panama City, Florida	June 1976	Sand
Daytona Beach, Florida	November 1973 November 1976	Sand
Corpus Christi, Texas	April 1977	Mud
Scotian Shelf	September 1978	Gravel

---

yield mode-amplitude and mode-attenuation data. The long-range experiments permitted calculation of mode-attenuation data at longer ranges, which has certain advantages if only the first mode is desired. Dispersion analysis was performed upon selected signals from all three types of experiments. The experiments are described as follows:

1. Short-range experiments employed small 7.1 g (1/4 oz) charges detonated at depths selected to suppress certain modes, while enhancing others. The receiver for these tests was a bottom-moored vertical array of hydrophones spanning the water column in 31 m of water. The maximum range for these tests was limited by line-of-sight for radio-frequency propagation, typically 12 m for the antenna placement used. Shots were deployed at range intervals of approximately 1 km. For these tests, the shot boat also served as the recording platform for data telemetered from the receiver.
2. Experiments to study propagation at longer ranges employed an aircraft (or another ship) to drop larger charges. The aircraft operations typically used 816 g (1.8 lb SUS) charges detonated at depths of 18.3 and 244 m. The maximum range was approximately 100 km, and the shot spacing in range was nominally 18 km. The receiver for these tests was usually a single hydrophone, one meter above the bottom, the output of which was telemetered to the support ship for recording.

3. The seismic-refraction experiments, designed to yield sub-bottom information, used 454 g (1 lb) charges detonated on the bottom. The maximum range and spacing were very similar to the short-range tests. The receiver was the single hydrophone and a three-axis geophone; again, the data were recorded aboard ship as the charges were dropped at increasing ranges. At some sites, the experimental procedure varied somewhat from those described here--these will be noted as they occur.

In addition to the acoustic information obtained during the experiments, other data such as sound-velocity profiles, cores, grab samples, sea conditions, and sub-bottom profiles were obtained whenever possible. On those occasions when this data could not be obtained during the experiment, the best available alternate data sources were used.

### 3.3 Data Collection System

The basic requirement of the data-collection system was to receive the acoustic signals which propagated through the water from the source, process the signals so they were suitable for recording on analog tape, and finally, record the signals. Two basic systems have been used for accomplishing this: (1) a system using a telemetry link to transfer data from the sensors to the recorder aboard a ship, and (2) a system using a cable, hardwiring the sensors to the recorder mounted on an oceanographic platform. The first system was used for all experiments except the Panama City tests where the second system was used. Both systems will be discussed, and the sensors and sources used will be described.

3.3.1 Shipboard and in-water instrumentation. The buoy system is pictured in Figure 2 and consists of a submerged unit, sensors, an underwater RF cable, and a small antenna buoy. The sensor outputs were processed by amplifying the signals, with preamplifiers and variable-gain amplifiers, and then filtering the signals to a frequency band dictated by the telemetry system. The processed signals were then used to frequency modulate, in an FM/FM process, a data transmitter. The transmitter was coupled to the antenna, mounted on a surface buoy, by an underwater RF cable. The submerged unit also contained batteries and several other sensors such as a leak detector, battery monitor, and a two-axis pitch sensor. Data were received at the ship and recorded on analog tape. Commands were sent from the ship to the buoy to change the amplifier gains and other buoy functions. System 3 dB bandwidths were 2 to 640 Hz for the hydrophone channels and 2 to 350 Hz for the geophone channels. Calibration of the system was performed by commanding a built-in autocalibrate signal.

The hard-wired system was very similar to the buoy system except the RF link was replaced with a multi-conductor cable. Preamps were mounted with the sensor as the in-water component of the system. Variable-gain amplifiers (VGA) were mounted on the fixed oceanographic platform where the data was recorded. The geophone system frequency response was the same, while the hydrophone response was modified to cover a range of 20 to 4000 Hz. Commands were sent directly via the cable to change the VGA and preamp gain.



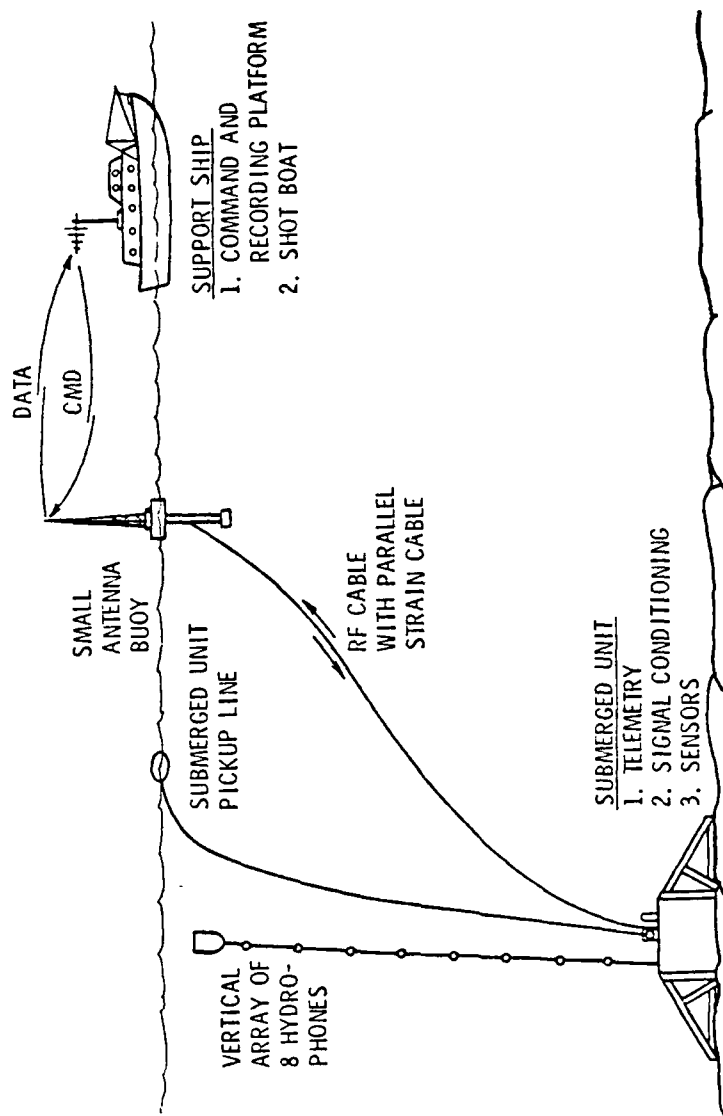


Figure 2. Data Collection System

3.3.2 Sensors. Two types of sensors were connected to the submerged unit, depending on the test to be performed. One sensor was the vertical array, while the other was the bottom-sensor unit consisting of a top-mounted and a bottom-mounted hydrophone and a three-axis geophone. The two systems were never operated together, since a change in the internal electronics accompanied the sensor change.

The vertical array used in the tests off Panama City and Daytona Beach consisted of eight omnidirectional LC-10 hydrophones spaced 3.7 m apart. The sensitivity of each hydrophone was approximately  $-210 \text{ dBv}/\mu\text{Pa}$ . In water depths of 31 m, the complete array was used, and the top of the supporting float was approximately 2 m below the surface. In a water depth of 18 m off Panama City, the top three hydrophones were tied together at the float 2 m below the surface. In a water depth of 18 m off Jacksonville, the top three hydrophones were tied back down the array and secured at the midway points between the lower hydrophones as shown in Figure 3.

In the Corpus Christi and Scotian Shelf tests, a new array was used that contained removable omnidirectional hydrophones having the same spacing and placement in the water column as the LC-10 array. The sensitivity of each hydrophone was  $-199 \text{ dBv}/\mu\text{Pa}$ . The upper hydrophones were tied back down the array for the shallow-depth tests using this array.

The hydrophones used in the bottom-sensor unit were the top hydrophone with a sensitivity of  $-185 \text{ dBv}/\mu\text{Pa}$ , and the bottom hydrophone, with a sensitivity of  $-195 \text{ dBv}/\mu\text{Pa}$ . The top hydrophone was omnidirectional, while the bottom hydrophone was more directional due to its inset location in the bottom bulkhead.

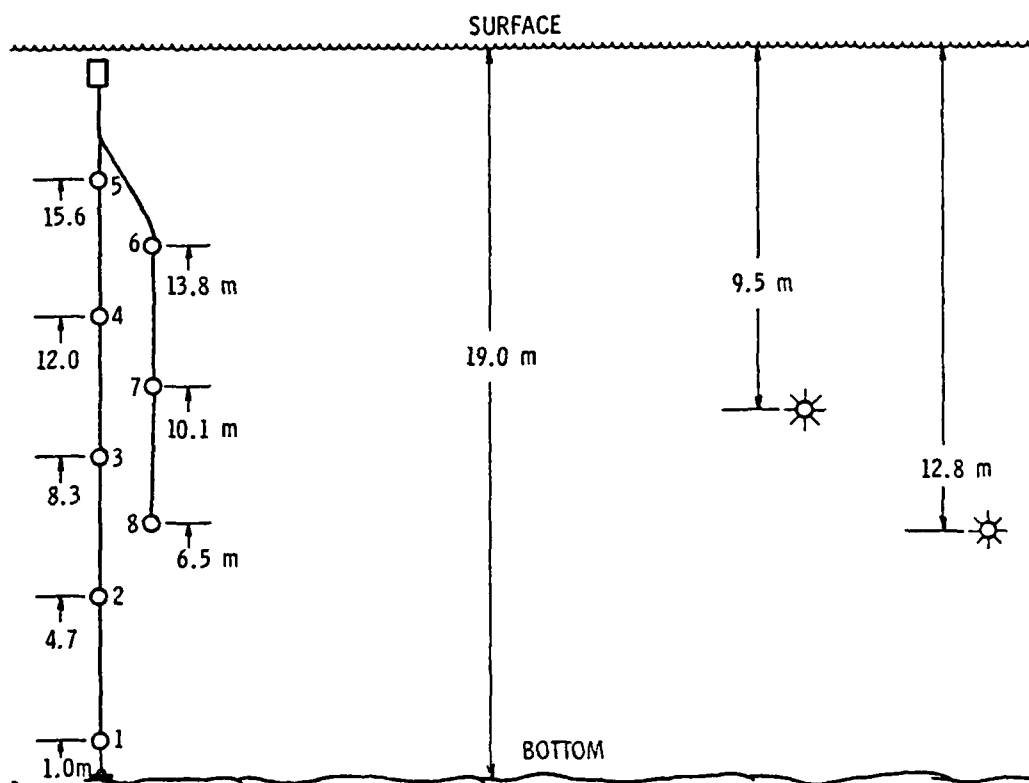


Figure 3. LC-10 Array Configuration--Daytona Beach Site

The three-axis geophone on the bottom-sensor package consisted of two horizontal and one vertical geophone mounted in three faces of an aluminum cube bolted to the inside face of the bottom bulkhead. The geophones were sensitive to particle velocity in the horizontal or vertical plane. The sensitivity of the geophones at 100 Hz with 5 dB of preamp gain was 2.75 V/cm/sec.

3.3.3 Sources. Several types of sources have been used, but the most widely used were the 7.1 g (1/4 oz), the 454 g (1 lb), and the 816 g [1.8 lb air-dropped SUS (Signal, Underwater Sound)] charges. The charges were composed of different explosive types, e.g., the 7 g charges were PETN; the weights given are the equivalent of the same weight of TNT. For all but the largest charge, the detonation depth was controlled by using a weighted charge at the end of a long cord of the desired length, suspended from a surface float. The SUS charge was preset to detonate at a particular pressure; detonation settings of 60, 800, and 1500 ft were available. Ship-launched charges were rigged with a long fuse to allow a separation in range between the ship and the detonation. The physics of the explosive process and the characteristics of the signals were discussed by Weston (1960).

In determining transmission loss in one-third-octave bands, the source level in the same frequency bands was required. Since it was not possible to measure this level for all combinations of charge weight, depth and frequency, procedures have been devised by Gaspin and Shuler (1971) for predicting these levels. Other researchers have noted errors at low frequency in the predicted source levels and have published procedures for making a low-frequency correction, e.g., Hughes (1976).

### 3.4 Analysis System and Procedures

In this section, the Hewlett-Packard Fourier Analyzer System is described. Its operation is related to the calculation of the received energy for both a single hydrophone and an array of hydrophones, the calculation of dispersion within a signal, and seismic-refraction analysis.

3.4.1 Hewlett-Packard Fourier System. The HP system consists of an HP 2100 A computer, a hard-wired Fast Fourier Transform Unit, an oscilloscope display, video terminal, digital tape unit, disc memory, and a control keyboard. In general, the system is designed to perform time-and-frequency-domain analysis of data containing frequencies from dc to 100 kHz. Input to the system is either via a two-channel analog input into a A/D converter or from the digital tape. Upon keyboard command, the unit can perform such operations as calculate forward and inverse Fourier transforms, power and cross-power spectra, coherence functions, auto- and cross-correlation, ensemble averaging in time and frequency, etc. Sampling and data-block size parameters are selectable; for most of the operations reported here, a sampling period of 500  $\mu$ sec was used which yields a frequency resolution of about 0.5 Hz for a block size of 4096 data words. These parameters give a maximum frequency of 1000 Hz and a maximum time window of about 2 sec. All input data are calibrated and carry a scale factor describing amplitude and a frequency code describing sampling parameters. Keyboard programs may be written for any sequence of steps involved in a computation. BASIC and FORTRAN programs may also be written for the HP 2100 A computer and called as a sub-program from a keyboard program.

3.4.2 Received energy calculations. Received signals are recorded at sea on analog tape along with a time code. By selecting the desired time on a synchronization unit, any point on the tape may be selected within one millisecond in time. The signal is low-pass filtered (0 to 1000 Hz) to prevent aliasing in the sampling operation, and at the selected time, the signal is strobed into the HP temporary storage as a digital signal. The signal is now ready for processing.

The purpose of processing the experimental data was to obtain the attenuation of the first mode. Where available, long-range data were used for this purpose since, in most cases, the energy was predominantly in the first mode. Short-range data were also used, but frequently these data were corrupted by strong contributions from the higher-order modes. When it was verified that only the first mode was present, the received energy was calculated from a single hydrophone output. When higher-order modes were present, the data were processed using array techniques involving several hydrophones.

The operations involved in the single hydrophone energy calculation are diagrammed in Figure 4. The signal was first filtered (anti-aliasing) and then stored in the temporary storage of the HP. The signal was then transformed into the frequency domain by the Fourier transform operation (F). The desired analysis filter was obtained by calling for this program as a subroutine, and the frequency-domain signal was then multiplied by the filter to give  $Y(f)$ , the filtered signal. The energy in the filtered signal was obtained using the equation:

$$\text{Energy} = \int_{f_1}^{f_2} |Y(f)|^2 df \quad .$$

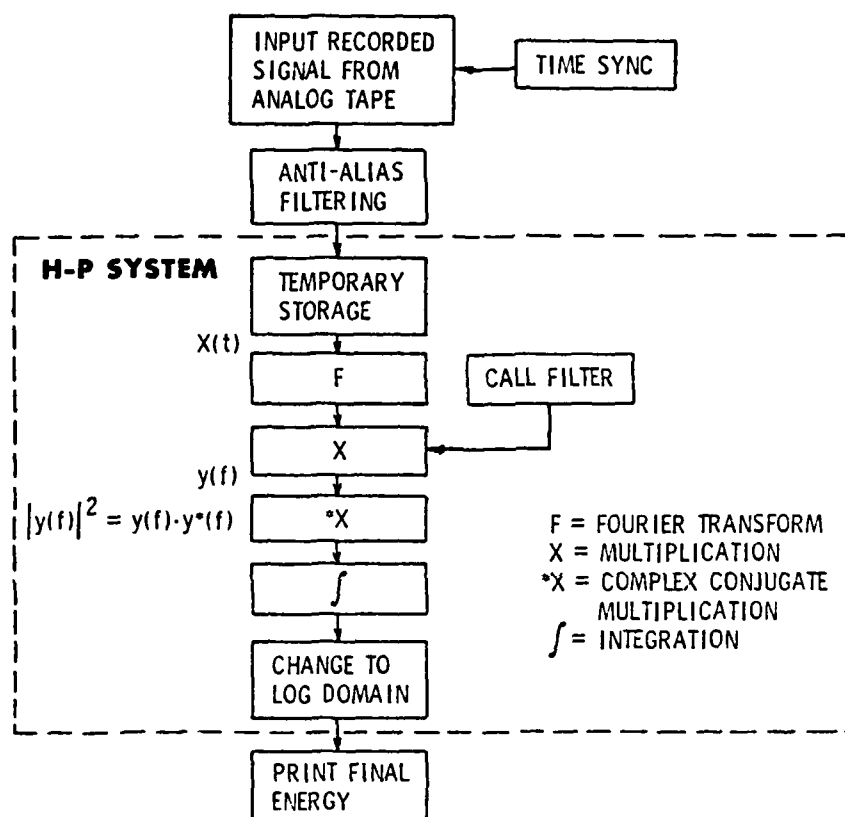


Figure 4. Energy Calculation--Single Hydrophone

Integration was performed as a summation at each frequency (or channel of the data word) from  $f_1$  to  $f_2$ . The energy levels were then converted to the logarithmic domain, and the final value in the block was printed to yield the energy level in dB.

Basically, two different types of analysis "filters" were used in processing the received energy. The first was a "filter" approximating the well known one-third-octave filter. As implemented on the HP analyzer, this filter was approximated by summing the energy in groups of channels within the 4096 channel data block. The frequency range of each group of channels represented approximately one-third of an octave in frequency. Nominal center frequencies of 25, 31.5, 40, 50, 63, 80, 100, 125, 160, 200, 250, 315, 400, 500, 630, 800, and 1000 Hz were used.

The other type of "filter" is an approximation to a finite-impulse-response filter having a Butterworth amplitude response curve. In many applications, the frequency-dependent phase response (or envelope delay) requires corrections when time delays or velocities are important. Because of this, filters have been constructed having Butterworth amplitude characteristics, but with zero phase terms. This is accomplished by setting the real part of each channel in the data block equal to the desired amplitude response, at that frequency, and setting the imaginary part equal to zero. With this type of filter, no delay correction is necessary. Low-pass, three-pole filters have been implemented, the frequency and time response tested, and the filters used to process dispersion data. For the array-processed data discussed next, bandpass filters were used having approximately one-half-octave bandwidths and center frequencies of 50, 100, 200, 400, 600, and 750 Hz.



As noted in the previous paragraph, the short-range data may have higher-order modes present. One way to extract the first-mode energy is to use modified array processing, which uses selected hydrophones from the array and the modal distribution of pressure in the water column to obtain a spatial separation of the first mode. This concept is illustrated in Figure 5 which shows a typical modal-pressure distribution in the water column for the first two modes and the array hydrophone locations. To cancel the second mode, hydrophones 2 and 7 are added and, since the phase of the second mode differs by  $180^\circ$  for these two signals, cancellation will occur. An implementation of this type of processing where all opposite phase hydrophone outputs are summed is described by Caswell (1979).

In this paper, the two hydrophones were processed as indicated in Figure 6. Signals A and B were cross-correlated to determine any phase shift due to tilting of the array away from vertical in the water. This phase error was determined as the number of shifts required for perfect alignment (the maximum cross-correlation value). Once this was determined, each signal was cleared of all the unwanted noise. One signal was shifted with respect to the other to correct the phase error, and the signals were then averaged. The remaining operations transformed the averaged signal back to the frequency domain to calculate the energy.

3.4.3 Dispersion analysis. The purpose of performing dispersion analysis is to infer characteristics of the ocean bottom by comparing experimental values of group velocity with those predicted by a normal-mode model. Dispersion is defined as a variation in the

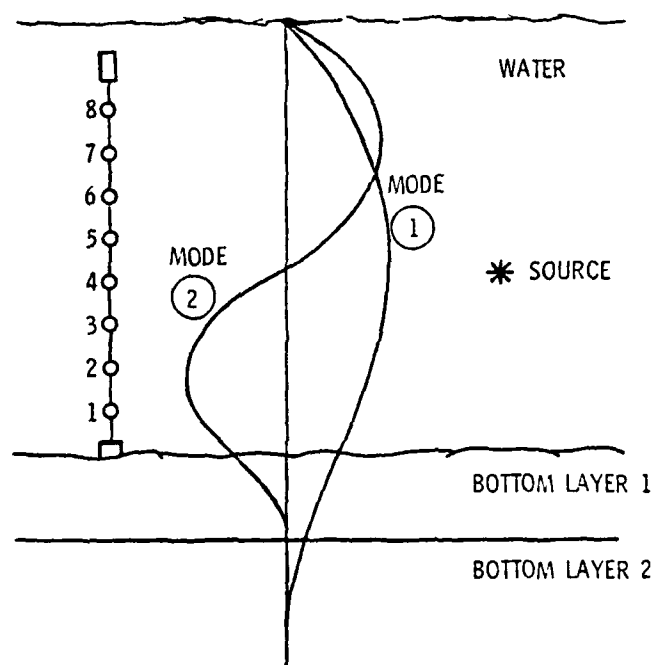


Figure 5. Mode Amplitude and Array Processing

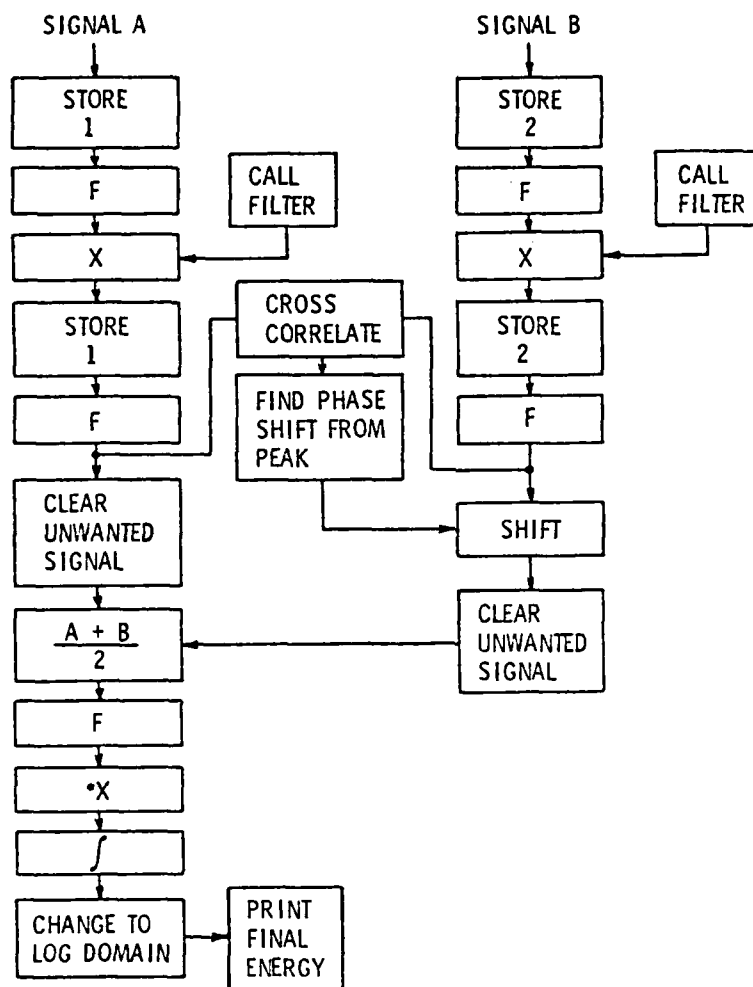


Figure 6. Energy Calculation--Array Type Processing

propagation velocity with frequency and as it results in this case, from the geometrical constraints imposed by the shallow-water sound channel, it is termed geometrical dispersion. Another type of dispersion, i.e., intrinsic dispersion, may result for example, from density variation within a material. For the shallow-water sound channel, dispersion is controlled by the water depth, the compressional sound speed in the water and sub-bottom layers, the layer thickness of sub-bottom layers, and the density in the water and bottom. This type of analysis was pioneered by Pekeris (1948) using the experimental results of Worzel and Ewing (1948).

Dispersive propagation for a water layer and a very thick bottom layer is illustrated in Figure 7 for the first mode. Part (a) shows a typical plot of the group velocity as a function of frequency, and part (b) illustrates how this behavior occurs in a typical, although idealized, shallow-water received signal. As can be seen, the signal starts with a low-frequency ( $f_c$ ) refracted arrival. At a time corresponding to the sound-speed in water ( $c$ ), a high-frequency water-wave arrival is superimposed upon the low-frequency rider wave ( $f_R$ ). The frequency of the water wave gradually decreases until the Airy-phase frequency ( $f_A$ ) is reached. The frequency then remains constant until the signal decays into the background noise. The refracted low-frequency arrival travels with the velocity of the bottom layer and has a characteristic frequency termed the cutoff frequency.

The experimental dispersion data was obtained by first filtering the signal with several zero-phase-shift, low-pass filters having different cutoff frequencies (e.g., 25, 50, 100, 200 Hz). Each

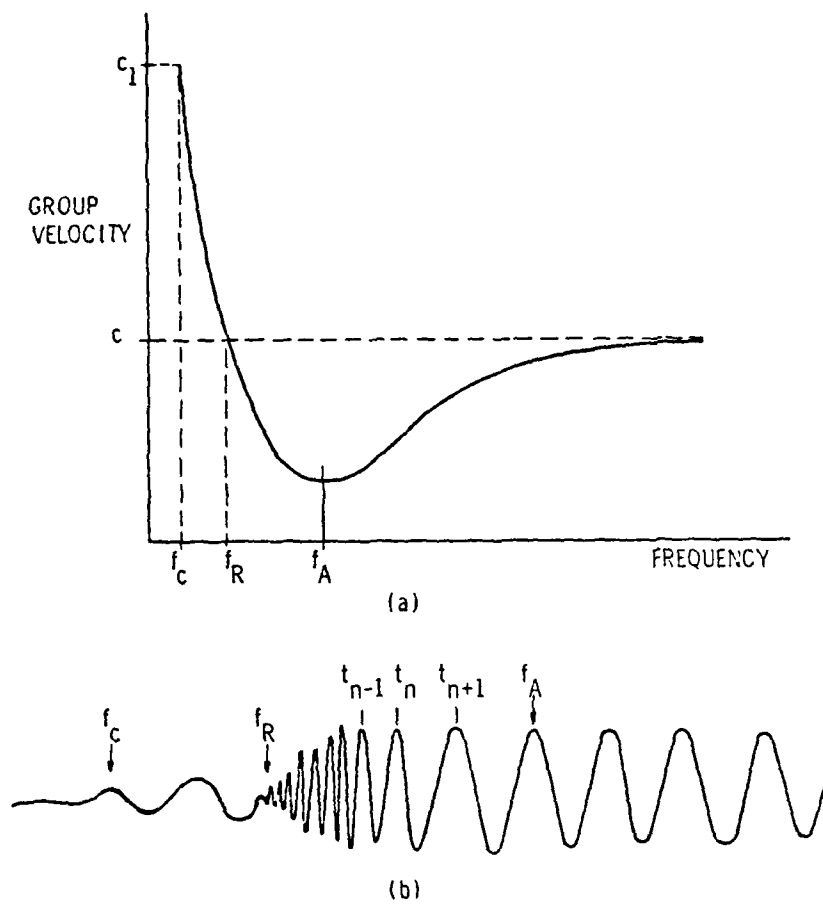


Figure 7. Geometrical Dispersion in Shallow Water

filtered signal was plotted in the time domain and the arrival times ( $t_n$ ) of signal peaks were listed. These were measured with respect to the water-wave arrival time since this velocity was known. The frequency of the  $n^{\text{th}}$  arrival was calculated from the relation

$$f_n = \frac{2}{t_{n+1} - t_{n-1}} ;$$

the group velocity was calculated from the equation

$$u_n = \frac{Rc}{R \pm t_n c} .$$

The times,  $t_n$ , were measured with respect to the water-wave arrival, for the range  $R$  and the known sound-speed in the water  $c$ . The plus (+) sign was used for arrivals after the water wave, and the minus (-) sign was used for the refracted arrivals occurring before the water wave. This procedure was followed for signals from several ranges and for each analysis filter used. If the water and bottom characteristics were independent of range, the plotted data for shots from different ranges should fall along the same curve.

Once the experimental values of  $f_n$  and  $u_n$  were determined, the analysis was continued by assuming values for the compressional sound speeds, layer thicknesses, and densities in the sub-bottom layer; it was assumed that the water velocity and depth were known. These parameters were then used as inputs to a normal-mode propagation model from which predicted values of group velocity were obtained as a function of frequency. These predicted values were then compared with the experimental values, the assumed bottom parameters changed, the model run again, and new values for the group velocity predicted for another comparison. The procedure was repeated until the predicted

values matched the experimental values with reasonable accuracy. Once this occurred, the most recent bottom model used was assumed to be the correct bottom model.

3.4.4 Seismic-refraction analysis. The use of dispersion analysis for determining ocean-bottom parameters has been discussed. However, an initial trial model must be provided as a starting point for the dispersion analysis. Frequently, this initial model is based on seismic-refraction analysis. This type of analysis relies on the fact that when sound rays strike the ocean bottom at the critical angle (assuming all velocities are increasing with depth), energy travels along the ocean-bottom interface with a velocity equal to the compressional sound speed in the bottom. Energy also penetrates to deeper layers, so that critical-angle refraction occurs at each velocity discontinuity (i.e., layer) found in the bottom. These interface waves are eventually refracted back toward the water layer where they may be received on a hydrophone. As noted, the key assumption is that the velocity in successively deeper layers is always increasing.

For the seismic-refraction experiments, charges were detonated on the bottom at 0.23 km range intervals for the first 1.9 km and then every 0.46 km out to the maximum range--usually 8 to 12 km. Long fuses were employed to insure bottom detonation. This required a range correction for the fuse-burn time. Ranges were calculated based on the signal received on a hydrophone deployed from the shot boat.

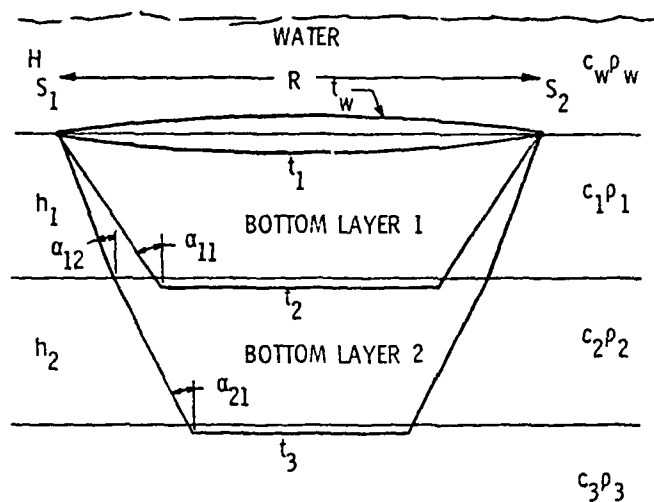
The theory and analysis of the refracted arrivals can be understood with the aid of the four-layer model in Figure 8. The model represents shots detonated on the seabed at point  $S_1$  and received on the seabed at point  $S_2$ . At the receiver, assuming a large separation  $R$ , the first signal arrives after traveling with time  $t_3$ , the next travels for  $t_2$  seconds, then  $t_1$ , and finally, at  $t_w$ , the water wave arrives. Implied in this sequence is that  $c_3 > c_2 > c_1 > c_w$  as stated earlier. With the exception of  $t_w$ , all are refracted arrivals that obey the travel-time relations in the lower part of the figure. Each of these is derived using Snell's law and geometrical ray theory. Snell's law is stated for this situation by the two assumptions in the figure, where it is implied that the refracted ray leaves the interface at an angle of  $90^\circ$ ; that is,

$$\frac{\sin \alpha_{11}}{c_1} = \frac{\sin 90^\circ}{c_2} = \frac{1}{c_2}.$$

Note that  $t_1$ ,  $t_2$ , and  $t_3$  are all linear functions of  $R$ . Thus,  $t_1$  as a function of  $R$  is a straight line with a slope of  $1/c_1$  and a zero intercept. A plot of  $t_2$  as a function of  $R$  has a slope of  $1/c_2$  and a time-axis intercept of  $(2h_1 \sqrt{c_2^2 - c_1^2})/c_1 c_2$ ;  $t_3$  obeys a similar relationship. This is illustrated in Figure 9.

With this background, the analysis procedure can be described as follows. The received signals were recorded with a high gain so that the refracted arrivals were clearly visible. Upon playback using the HP, they were plotted with an expanded scale so that the time of arrival could be measured with some accuracy. The first-arrival points were recorded and plotted for each shot. Since the range increased for each shot, these points were plotted as the crosses in Figure 9. Once





ASSUMPTIONS: (1)  $\frac{\sin \alpha_{11}}{c_1} = \frac{1}{c_2}$   
 (For critical angle entry)  
 (2)  $\frac{\sin \alpha_{12}}{c_1} = \frac{\sin \alpha_{21}}{c_2} = \frac{1}{c_3}$

TRAVEL TIME RELATIONS:

$$t_1 = \frac{R}{c_1}$$

$$t_2 = \frac{R}{c_2} + \frac{2h_1 \sqrt{c_2^2 - c_1^2}}{c_1 c_2}$$

$$t_3 = \frac{R}{c_3} + \frac{2h_1 \sqrt{c_3^2 - c_1^2}}{c_1 c_3} + \frac{2h_2 \sqrt{c_3^2 - c_2^2}}{c_2 c_3}$$

Figure 8. Seismic-Refraction Relations

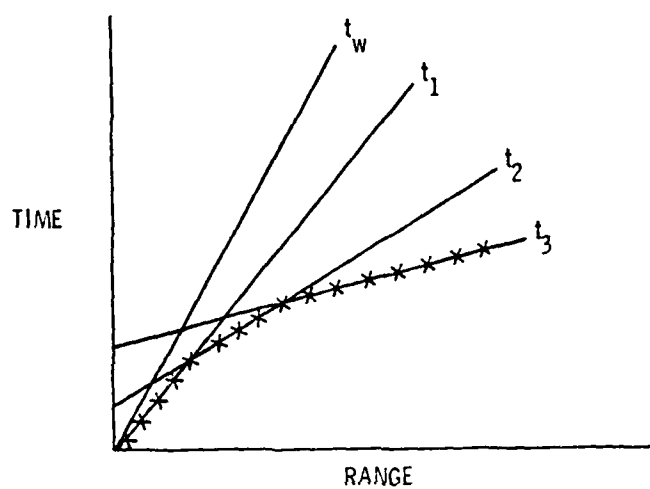


Figure 9. Refracted Arrivals--Range-Time Plot

the data was all plotted, points lying on the same line were obvious and could then be grouped together. A straight-line-fitting procedure was applied to each of these groups to obtain the slopes and intercepts. Thus, from the line identified as  $t_1$ , the velocity  $c_1$  was obtained, and knowing the intercept value,  $h_1$  was readily calculated. Finally, from  $t_3$ , the velocity  $c_3$  and thickness  $h_2$  were calculated. This procedure may be extended to any number of layers as noted by Officer (1958).

In reality, certain bottom structures require a more detailed analysis or may give incorrect results. For example, a thin layer may not appear as a first arrival, so frequently the arrival times of the secondary arrivals must be obtained as well--in most cases, a difficult task. If a low-velocity layer (a layer with a velocity less than the layer above it) occurs, all layer thicknesses calculated below the low-velocity layer will be in error. This problem is discussed by Dobrin (1976). We have assumed a flat, horizontal bottom structure; however, sloping bottoms may be analyzed using these techniques as well. In this case, the inverse slope is no longer the velocity, but is a function of the critical angle and the angle of the bottom slope. A modification to the experimental geometry, i.e., switching the source and receiver position, is frequently employed to resolve the unknown slope angle. Both Officer and Dobrin discuss this problem.

In general, seismic-refraction analysis gives good results where velocities are concerned, but has limits on the order of a wavelength or so for thickness measurements. Dispersion analysis is employed to give better resolution for detecting thin near-surface bottom layers.

### 3.5 Data Characterizing the Sediments

Several different types of input data are required in order to characterize the bottom for sediment-modeling purposes. The dispersion and seismic-refraction analyses are used to describe a large section of the seabed. The sediment model (discussed in Chapter II) may describe only the top few meters or so. The data required for this is grain-size and distribution, bulk density, porosity, etc., which may be obtained from surface grab-samples or cores. In certain cases, specialized acoustic-profiling systems (e.g., the Hunttec DTS System) can give some measure of the grain-size and distribution. With this data, as a minimum, the mean grain-size and sorting (i.e., standard deviation), the permeability, and pore-size parameter may be calculated for use in the model. The bulk density may be calculated once the porosity is estimated from empirical data. The desired output of the model is the sediment absorption as a function of frequency.

In all cases, attempts were made to obtain core and grab-sample data as part of the experimental program. In most cases, however, the available equipment was inadequate for obtaining data in the bottom types encountered. Because of this, core and grab-sample data collected by other researchers were frequently obtained by contractual analysis. Finally, where no other data could be obtained, the open literature was studied for the best available data. The availability, quantity, and type of sediment data are discussed on a site-by-site basis in the appropriate chapters.

## CHAPTER IV

### BOTTOM-ABSORPTION ANALYSIS

#### DAYTONA BEACH EXPERIMENTS

##### 4.1 Introduction

Experimental data obtained at two sites off the coast of Daytona Beach, Florida, is analyzed to determine the magnitude of losses attributable to absorption in the sedimentary layer. The experiments performed are discussed in detail in Chapter III, but are briefly reviewed here to establish the applicable environmental and experimental parameters for the test sites under discussion. The analysis procedures discussed in Chapter III are applied to recorded data to obtain mode-attenuation coefficients from which the experimental bottom-absorption losses are determined. The bottom models established for both sites and the techniques used to obtain them are discussed. Finally, the sediment data available for each site is presented, and the bottom absorption predicted by the sediment models is compared with the experimental values.

##### 4.2 Experiments

Experiments were performed during November of 1976 at two sites, depicted in Figure 10, off the coast of Daytona Beach, Florida. The water depth was nominally 19 m at the shallow site (Site 1) and 32 m at the deeper site (Site 2). In addition to the data analyzed from the 1976 experiment, certain data obtained in the vicinity of Site 2 during an earlier experiment (1973) were analyzed as well. Sound-velocity and

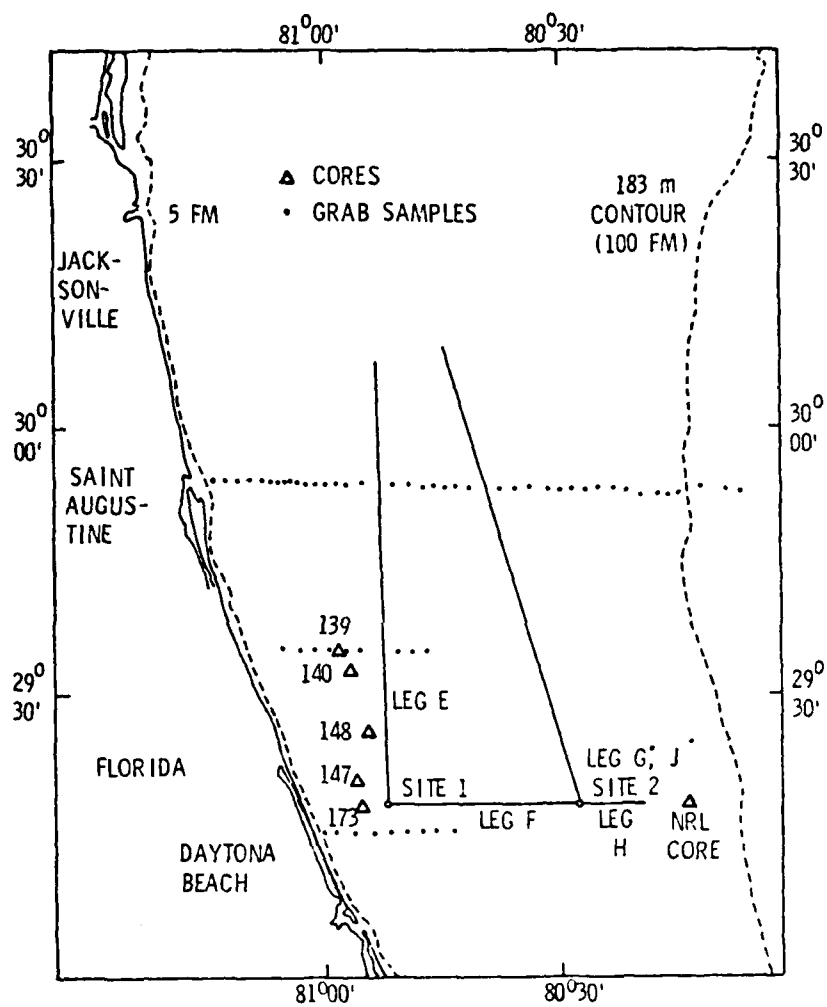


Figure 10. Daytona Beach Test Area

XBT data were obtained at the sites and along the propagation tracks. A 12 kHz fathometer was also operated along the tracks to obtain the bathymetry. Neither cores nor sub-bottom profiling data were obtained during the tests. Because of the lack of bottom data, grab-samples and cores were obtained from sources to be discussed later.

At Site 1, the experimental data obtained were from the mode-attenuation and seismic-refraction experiments. Sources for the mode-attenuation tests were 7.1 g charges detonated at depths of 9.5 and 12.8 m. The receiver was the vertical array and since the array length was greater than the water depth, it was folded back (see Figure 3) to provide closer spacing in the upper half of the water column. The variation in water depth and sound velocity with range along the constant-depth (Leg E) and deep-to-shallow (Leg F) legs are depicted in Figure 11. The long-range transmission loss experiment was not performed at this site due to adverse weather conditions. Signals selected from the constant-depth leg shots of the seismic-refraction experiment were used for dispersion analysis at this site.

The experiments performed at Site 2 were very similar to those performed at Site 1. Short-range, mode-attenuation data were obtained at Site 2 along both sloping (Leg H) and constant-depth (Leg G) tracks out to a range of 12 km. The water depth shown in Figure 12 was essentially constant over both legs. The small 7.1 g charges were detonated at 8.5 and 17 m and received on the same vertical array extended to its full length. Sound-velocity profiles taken indicated that the water was isovelocity.

Long-range propagation data were obtained at Site 2 out to a range of 95 km on the constant-depth (Leg J) track depicted in

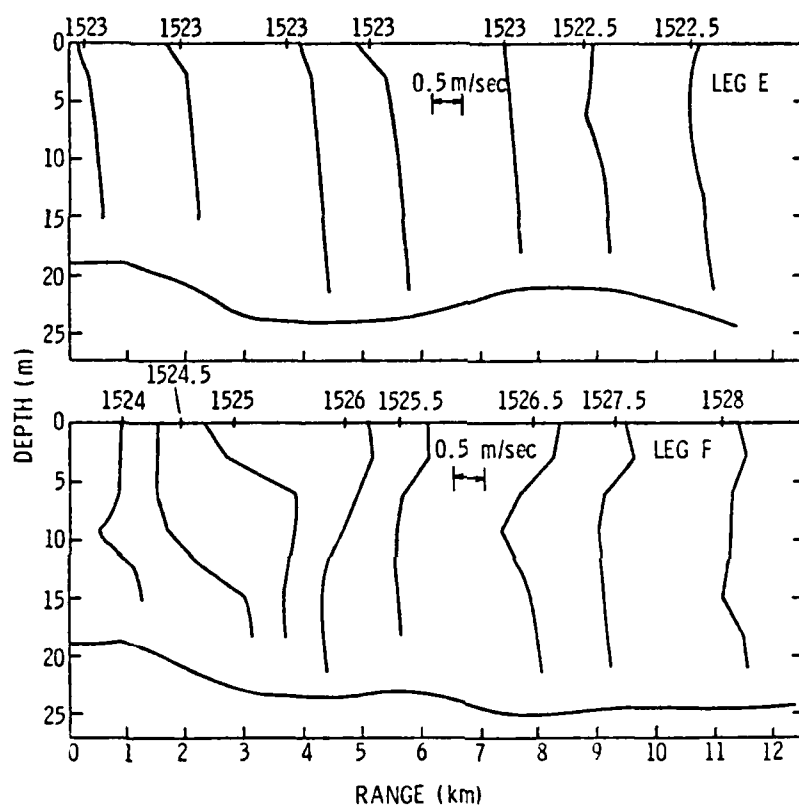


Figure 11. Depth and Sound Velocity Profiles--Daytona Beach Site 1



Figure 12. Air-dropped bathythermograph probes (AXBT's) indicated that temperatures varied little with water depth.

Seismic-refraction experiments were performed at Site 2, during both the 1976 and the 1973 tests. Also performed during the 1973 tests was a short-range seismic experiment using an array of 12 hydrophones placed in a straight line in contact with the bottom. Small 7.1 g charges were detonated on the bottom at approximately 31 m from the closest hydrophone, and arrival times were measured to calculate refracted-wave velocities. The water depth for this experiment was 43 m.

#### 4.3 Analysis of Data--Site 1

The objective of the data analysis for both Sites 1 and 2 was to show that bottom absorption can be predicted by the sediment model. To show this, experimental values of bottom absorption were calculated as a basis for comparison. This was accomplished by first calculating the received energy and then the mode-attenuation coefficients for the first mode from which the experimental bottom-absorption coefficients were obtained.

Since long-range data were not available for Site 1, short-range data were used. Hence, some consideration for higher-order modes was required and, consequently, modified array processing of the received signals (described in Chapter III) was performed. Signals received from the small charges detonated at 9.5 m were analyzed by these techniques.

##### 4.3.1 Received energy and mode-attenuation calculations--Site 1.

Short-range data were obtained along Leg E for ranges of 0.76 to 12.0

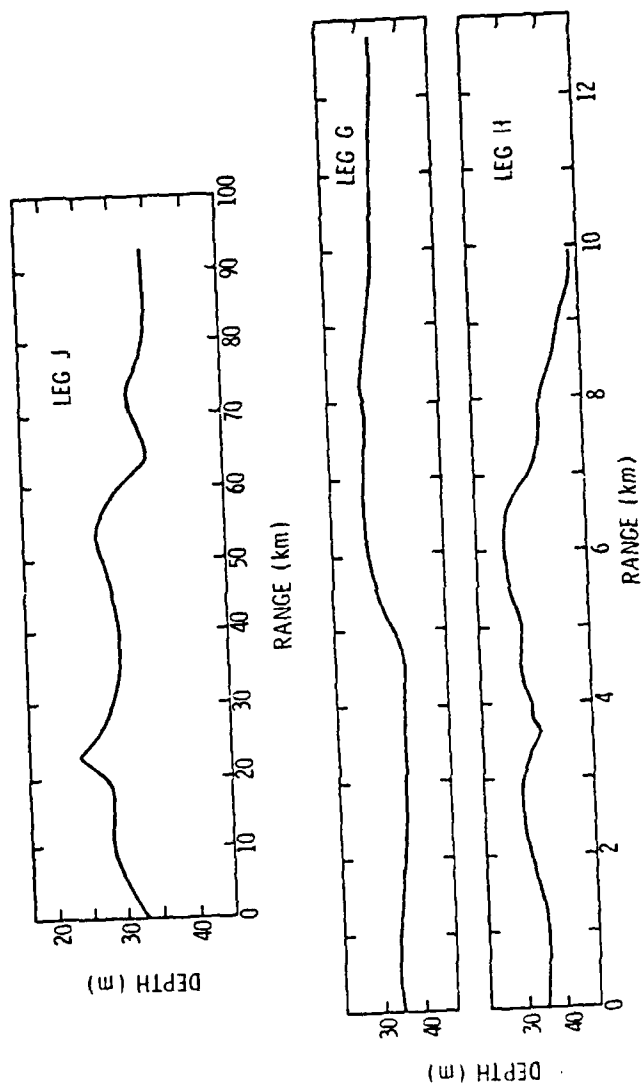


Figure 12. Depth Profiles--Daytona Beach Site 2

km and along Leg F for 0.5 to 15.9 km. Two shots were detonated at the 9.5 m source depth at each range point. Data were obtained over a frequency range of 50 to 750 Hz.

To obtain the received energy due only to the first mode, a summation of two hydrophones was performed in the laboratory in order to cancel the contribution of the higher modes. This calculation was performed by first selecting the two hydrophone signals having the best signal-to-noise ratio and location in the water column to obtain optimum cancellation of the second mode. For Leg E, the two hydrophones used were numbers 2 and 6, and for Leg F, numbers 2 and 7 were used. Analysis filters (one-half octave) centered at 50, 100, 200, 400, 600, and 750 Hz were used. The hydrophone pairs were processed as noted in Section 3.4.2 to obtain the received energy for the first mode.

In order to calculate the mode-attenuation coefficients, the received energy was corrected for system gain and cylindrical spreading. Since the mode-attenuation coefficients were defined as the slope of the line obtained by plotting the loss as a function of range, only range-dependent effects were considered. Hence, the source strength was not required for this calculation and the transmission loss was not calculated. The received energy was corrected for gain relative to the gain at one range and corrected for cylindrical spreading relative to the spreading loss at one range. Data were deleted for those shots where the signal-to-noise ratio was less than approximately 3 dB. The zero decibel reference for the relative energy calculation is defined as  $1 \text{ volt}^2\text{-sec}$ .

Using the relative energy levels, the mode-attenuation coefficients were obtained by performing a straight-line, least square

fit to the data at each frequency. The mode-attenuation coefficients are shown in Table 3 for Legs E and F along with the 95 percent confidence interval limits. The relative energy levels and straight line fits are plotted in Figures 13 and 14 for Legs E and F, respectively.

4.3.2 Bottom model--Site 1. To calculate the bottom absorption given the experimental mode-attenuation coefficient for the first mode ( $\delta$ ), the energy present in the sub-bottom layers ( $\gamma$ ) must be known. The normal-mode program gives this information; however, to run the program, a valid model for the sub-bottom structure must be obtained for use as input to the program.

Such a sub-bottom model has been determined by an analysis of the dispersion exhibited by shots received along the constant-depth track (as discussed in Chapter III). The experimental dispersion data is plotted in Figure 15 as the discrete points. Group velocities predicted by a four-bottom-layer normal-mode propagation model, using the water-bottom structure shown, are plotted as the solid line. Although the water depth varied along Legs E and F, as shown in Figure 11, a water depth of 20.5 m was used for both legs. The sound-velocity profile shown is from a range of 3.8 km along Leg F and is representative of those encountered along the track. The use of this profile for Leg E as well has little effect on the comparison of predicted and experimental data.

The bottom model shown in Figure 15 was selected on the basis of dispersion analysis and is consistent with the results of other researchers who have studied the test area. Meisburger and Field (1975) have conducted detailed surveys over the inner continental shelf from

TABLE 3

MODE-ATTENUATION COEFFICIENT ( $\delta$ )--SITE 1

## Daytona Beach

<u>Leg</u>	<u>Frequency (Hz)</u>	<u>Mode-Attenuation Coefficient (<math>\delta</math>) (dB/km)</u>	<u>95% Confidence Interval</u>	
			<u>Upper Limit</u>	<u>Lower Limit</u>
E	50	3.09	3.99	2.19
	100	1.29	1.59	0.99
	200	1.33	1.75	0.91
	400	1.08	1.39	0.77
	600	1.07	1.60	0.54
	750	1.43	1.71	1.15
F	50	2.78	3.35	2.21
	100	1.46	1.86	1.06
	200	1.27	1.53	1.01
	400	0.97	1.31	0.63
	600	1.03	1.41	0.65
	750	1.38	1.66	1.10

---

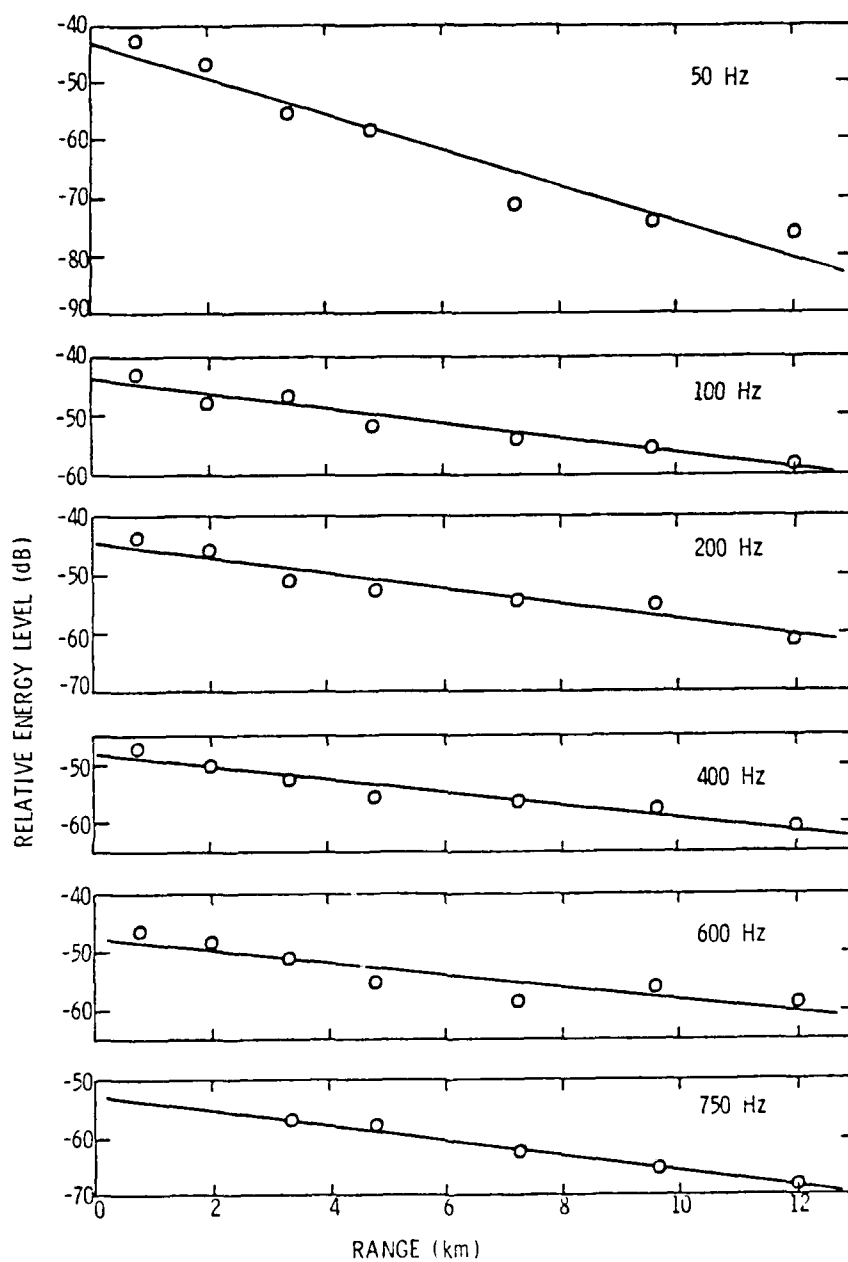


Figure 13. Relative Energy Levels--Daytona Beach Site 1, Leg E

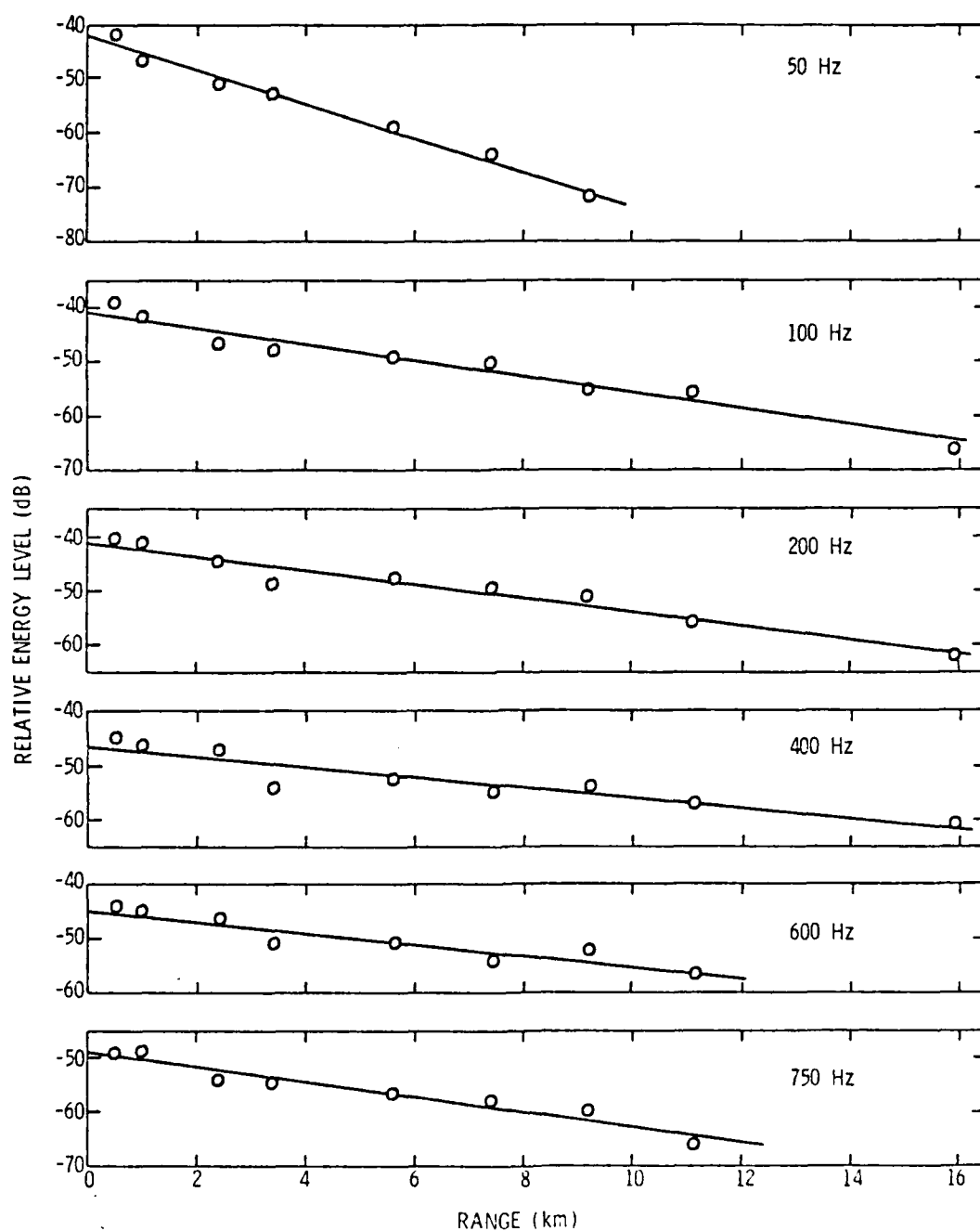


Figure 14. Relative Energy Levels--Daytona Beach Site 1, Leg F

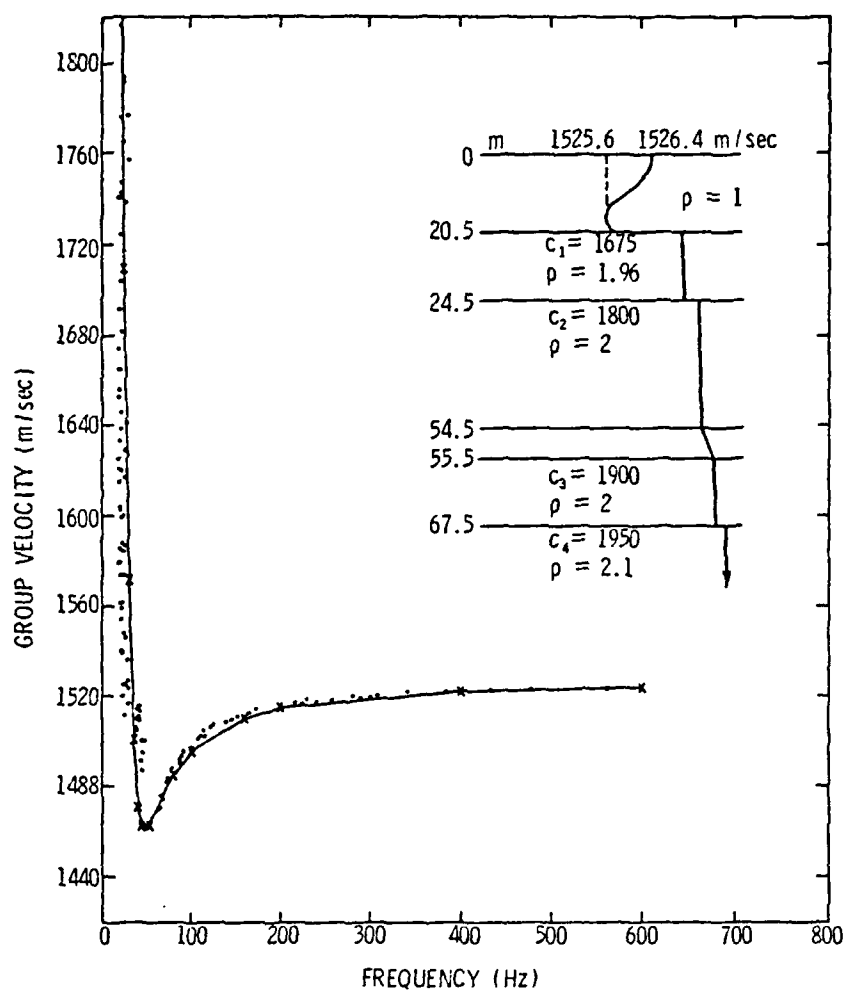


Figure 15. Daytona Beach Experimental and Model Dispersion--Site 1



Cape Canaveral to Georgia. Many grab-samples and cores were obtained to correlate with seismic-reflection lines run perpendicular to the shore. Two of these reflection lines bound Site 1 to the north and south and show primary reflectors (i.e., a layered structure) consistent with the bottom model of Figure 15. The velocities used in the present bottom model show reasonable agreement with seismic-refraction results obtained by Hersey et al. (1950), Antoine and Henry (1965), and Sheridan et al. (1966) off the Florida coast. The uppermost layer is reported to have a velocity between 1630 and 1810 m/sec for all of the results reported; the next layer has a velocity range of 2240 to 2690 m/sec. The layer thickness obtained by seismic-refraction analysis are generally much thicker than found by Meisburger and Field, and probably reflect the general insensitivity of the seismic-refraction techniques for showing small-scale changes in thickness.

4.3.3 Experimental sediment absorption--Site 1. With the four-layer normal-mode program and four-layer bottom model of Figure 15, mode-amplitude distributions of pressure throughout the water column and bottom were calculated and values for  $\gamma$  in each sub-bottom layer obtained. This data is listed in Table 4 where  $\gamma^{(1)}$  is the energy ratio for the first bottom layer, and  $\gamma^{(2)}$  is the ratio for the second, and so forth. The sum of the three is  $\gamma$ . The bottom-absorption coefficients  $\alpha_A$  for Leg E and Leg F were calculated by dividing the respective mode-attenuation coefficients by  $\gamma$ . These values of  $\alpha_A$  will be compared with the bottom absorption predicted by the sediment model.

TABLE 4

ENERGY DISTRIBUTION ( $\gamma$ ) AND BOTTOM-  
ABSORPTION COEFFICIENTS ( $\alpha_A$ )--SITE 1

Daytona Beach

Frequency (Hz)	$\gamma^{(1)}$	$\gamma^{(2)}$	$\gamma^{(3)}$	$\gamma$ [ $\gamma^{(1)} + \gamma^{(2)} + \gamma^{(3)}$ ]	Leg $\gamma$ $\alpha_A$ (dB/km)	Leg F $\alpha_A$ (dB/km)
50	0.10210	0.14250	0.00002	0.24477	12.62	11.36
100	0.05449	0.01541	- -	0.06990	18.45	20.89
200	0.01890	0.00090	- -	0.01980	67.18	64.14
400	0.00424	- -	- -	0.00425	253.97	228.11
600	0.00156	- -	- -	0.00156	684.46	658.88
750	0.00090	- -	- -	0.00090	1588.89	1536.89

4.3.4 Predicted sediment absorption--Site 1. As discussed in Chapter II, the model for a porous fluid-filled medium as developed by Biot and later refined by Stoll was used to predict sediment absorption and velocities. In order to apply this model, certain parameters describing the sediments in the test area are required. Ideally, the area should be well-sampled with deep cores analyzed to yield such parameters as mean grain-size, grain-size statistics, density, porosity, and mineralogy. At Site 1, both cores and grab-samples are available. The cores are numbers 139, 140, 147, 148, and 173, discussed by Meisburger and Field (1975), analyzed at the University of Texas at Arlington. The grab-samples (65 total) are reported by Milliman et al. (1972) and were analyzed at Duke University. The grab-samples provide the best coverage near Site 1 as may be seen in Figure 10 where both the cores and grab-samples are noted. The grab-sample analysis provided only the grain-size, grain-size statistics, and calcium carbonate content. However, empirical studies, such as performed by Hamilton (1969), may be used to relate grain-size to porosity and then to density. The pertinent grab-sample data is listed in Table 5. As can be seen in Figure 10, the northern and southern sample lines bound the site and propagation tracks on the north and south. A study of the mean grain-size ( $M_z$ ) of these samples reveals a gradual decrease in grain-size until a minimum is reached at sample 1482 along the north and sample 1478 along the south. The mean grain-sizes increase from the minima to the end of the sample lines. This behavior seems to indicate that a band of moderately-sorted, coarser sediments runs parallel to the shore across the site and both propagation tracks.

TABLE 5  
SITE 1 GRAB-SAMPLE DATA  
Daytona Beach

Northern Line				Southern Line			
Number	$M_z$ (phi)	$\sigma_\phi$ (phi)	Percent CaCO <sub>3</sub>	Number	$M_z$ (phi)	$\sigma_\phi$ (phi)	Percent CaCO <sub>3</sub>
1485	1.50		13.8	1474	2.51	0.33	8.6
1484	2.00	0.49	24.5	1475	2.68	0.36	15.4
1483	1.17	0.99	34.7	1476	2.00	0.39	24.9
1482	0.55	1.79	46.0	1477	1.63	0.52	36.7
1481	1.82	0.41	28.1	1478	0.40	1.85	62.1
1480	1.64	0.50	28.5	1479	1.73	0.51	37.4
Average	1.44	0.84	29.3	Average	1.82	0.67	30.8

Note:  $\phi = -\log_2 d$ ; d is the mean grain diameter in mm.

The two sample lines are characterized for modeling purposes by the average values noted in Table 5.

Based on these average mean grain-sizes and standard deviations, permeability and pore-size parameters ( $K$  and  $a$ ) were calculated as noted in Chapter II for use in the sediment model. The aggregate bulk modulus  $k_r$  for the minerals within the sediment frame was calculated using the VRH method (described in Chapter II) for a calcium carbonate content of 30 percent obtained from Table 5 and a 70 percent quartz sand content. Densities and porosities were estimated as noted earlier. The parameters describing the two sediment models used are listed in Table 6, and the resulting bottom absorption for the frequencies of interest are listed in Table 7.

4.3.5 Discussion of results--Site 1. The bottom absorption obtained from the mode-attenuation coefficients (the experimental data) and that predicted by the sediment models of Biot and Hamilton are compared in Figure 16. For the Biot model, good agreement is obtained between 100 and 400 Hz for the model representing a sediment with a mean grain-size of 1.44 phi. Much less attenuation is predicted by the model at 50 Hz than was measured. This occurs because the sediment model represents only a very shallow bottom layer, and, at 50 Hz, the sound waves penetrate into the third bottom layer. The additional attenuation due to these deeper layers results in the increased low-frequency attenuation. The Hamilton model predicts greater absorption at low frequency but less at high frequency, giving somewhat poorer agreement than the Biot model.

TABLE 6  
BIOT SEDIMENT MODEL PARAMETERS--SITE 1

Daytona Beach

$N_z$ (phf)	$\sigma_\phi$ (phf)	$K$ (cm <sup>2</sup> )	$a$ (cm)	$\beta$	$\rho$ (g/cm <sup>3</sup> )
1.44	0.84	$3.42 \times 10^{-7}$	$2.26 \times 10^{-3}$	0.390	2.04
1.82	0.67	$2.53 \times 10^{-7}$	$1.95 \times 10^{-3}$	0.405	2.02

Note: $k_r = 4.6 \times 10^{11}$ dyne/cm <sup>2</sup>	$v_E = 3.0 \times 10^4$ cm/sec
$k_f = 2.4 \times 10^{10}$ dyne/cm <sup>2</sup>	$v_s = 2.1 \times 10^4$ cm/sec
$\rho_r = 2.71$ g/cm <sup>3</sup>	$\alpha = 1.25$
$\rho_f = 1.0$ g/cm <sup>3</sup>	$\Delta_E = 0.15$
$\eta = 0.01$ dyne-sec/cm <sup>2</sup>	$\Delta_s = 0.20$

TABLE 7

PREDICTED BOTTOM ABSORPTION ( $\alpha_A$ )

Daytona Beach

$M_z$ (phi)	$C_\phi$ (phi)	Absorption ( $\alpha_A$ ) (dB/km)					
		50 Hz	100 Hz	200 Hz	400 Hz	600 Hz	750 Hz
1.44	0.84	5.10	18.43	68.75	249.66	500.53	707.32
1.82	0.67	3.98	13.96	51.57	191.59	401.60	590.58

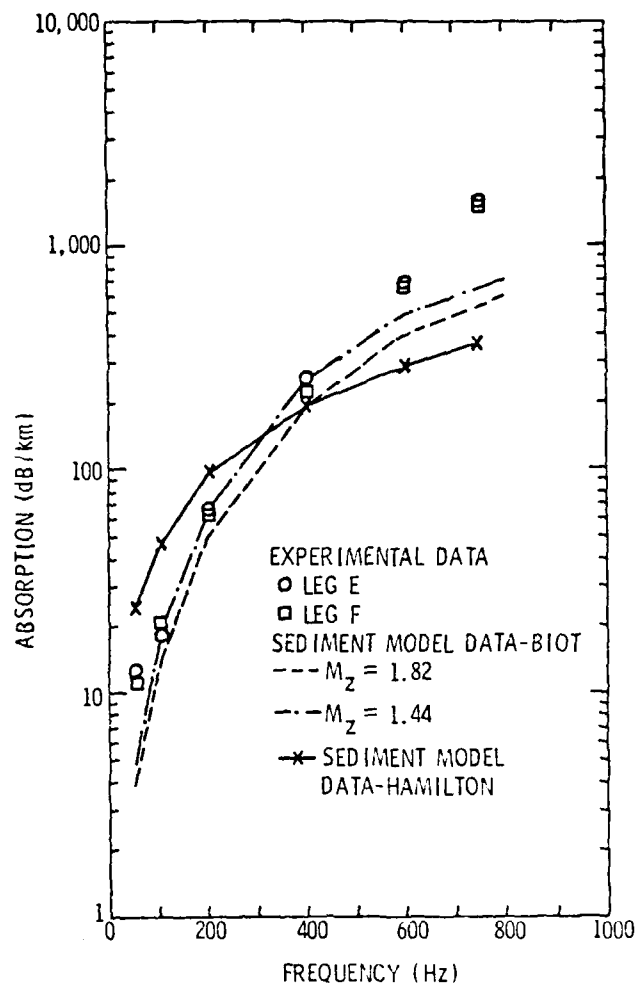


Figure 16. Comparison of Experimental and Predicted Bottom Absorption--Daytona Beach Site 1



At 600 and 750 Hz, the modal attenuation in Table 3 is greater than expected, based on the general decrease of the coefficient between 50 and 400 Hz. One possibility for this large attenuation coefficient is that higher-order modes are present at the shorter ranges and a gradual attenuation (or stripping) of these modes occurs resulting in a higher effective attenuation for the first mode as the range increases. This possibility was investigated by further processing on the hydrophone outputs which appeared to have the least contribution due to the higher modes. Typical 750 Hz signals are illustrated in Figure 17 where the upper signal has a great deal more energy in modes two and three than does the lower signal. In order to obtain the energy due only to the first mode, the signals were processed by removing all of the signal except the first mode due to the shock pulse. That is, only the signal between A and B in Figure 17 was retained. The result was that the mode-attenuation coefficient at 750 Hz was higher still. Thus, it has been concluded that mode stripping is not responsible for the high mode-attenuation coefficients at 600 and 750 Hz.

Another loss mechanism, associated with the higher frequencies, which was considered as a possible source of the 600 to 750 Hz attenuation is scattering due to any roughness associated with the surface and bottom. This mechanism was ruled out, however, since the seas were calm (sea state one or less) on the particular day of testing and the bottom variations change slowly with range.

The last source of attenuation to be examined as a possibility was attenuation of a biological origin. This possibility was first considered when large masses of somewhat random reflectors were noted on the 12 kHz fathometer records obtained as the ship dropped shots

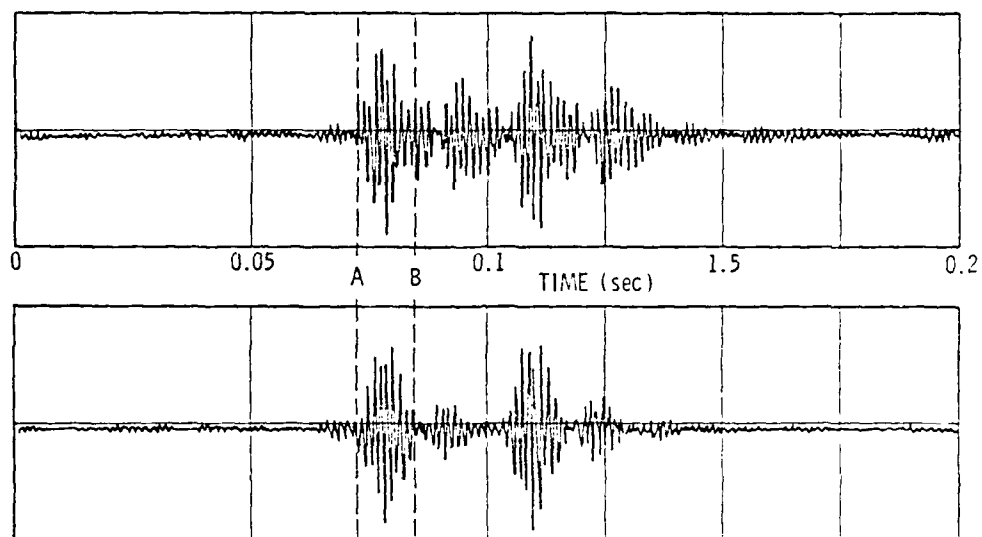


Figure 17. Removal of Higher Order Modes at 750 Hz--  
Daytona Beach Site 1, Range 1 km

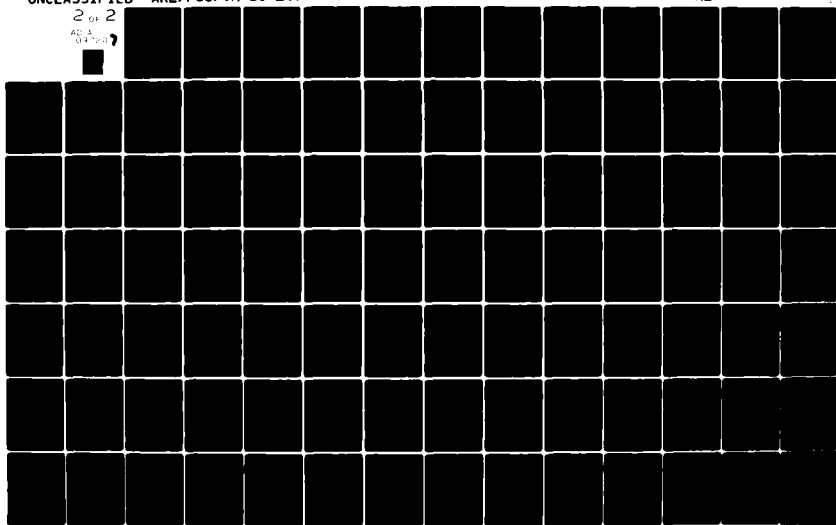
AD-A097 207

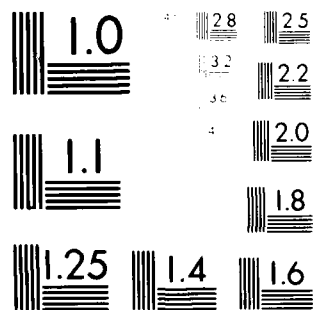
PENNSYLVANIA STATE UNIV UNIVERSITY PARK APPLIED RESE--ETC F/G 20/1  
AN EXPERIMENTAL INVESTIGATION OF OCEAN SEDIMENT EFFECTS UPON LO--ETC(U)  
DEC 80 J H BEEBE  
N00024-79-C-6043  
NL

UNCLASSIFIED

2 of 2

AD-A  
097 207





### Minimality Resolution Test (MRT)

$\forall \alpha, \beta \in \mathcal{A} \quad \alpha \leq \beta \Rightarrow \alpha \leq \beta \vee \alpha \leq \beta$

$\frac{1}{2} \times \frac{1}{2}$      $\frac{1}{2} \times \frac{1}{2}$      $\frac{1}{2} \times \frac{1}{2}$      $\frac{1}{2} \times \frac{1}{2}$      $\frac{1}{2} \times \frac{1}{2}$

along Legs E and F. An example of this is shown in Figure 18. It is assumed that the reflectors are some type of fish as they are present in varying degree along both Legs E and F. This source of attenuation has been considered by Weston and Ching (1970). They note a diurnal pattern in the magnitude of attenuation with the maximum occurring at night. Attenuation of up to 2 dB/km at 700 Hz was observed for a concentration of one 24-cm fish to approximately 10 square meters of sea surface. If it is assumed that the Biot sediment model accurately predicts the bottom absorption at 750 Hz [i.e.,  $\delta = (0.0009)(707 \text{ dB/km} = 0.64 \text{ dB/km}]$ , then the excess attenuation attributed to other mechanisms must be, subtracting this  $\delta$  from that in Table 3, approximately 0.79 dB/km. This is well within the magnitude observed by Weston and Ching. However, whether the concentration and size of the scatterers are consistent with the observed attenuation is an unanswered question.

#### 4.4 Analysis of Data--Site 2

At Site 2, both long-range and short-range data were obtained. The short-range data were analyzed by McDaniel (1979). Mode-attenuation coefficients were calculated in that paper and are presented for both sloping (H) and constant depth (G) tracks. Results from the constant-depth leg of the long-range propagation experiment are presented in the next section. A bottom model is described based on seismic-refraction and dispersion analysis, and the results from the short-range seismic experiment conducted in 1973.

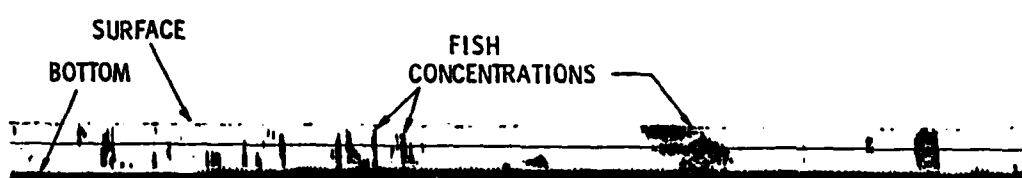


Figure 18. Fathometer Record--Daytona Beach Site 1,  
Leg E (5.6 - 7.4 km)

#### 4.4.1 Received energy and mode-attenuation calculations--Site 2.

An analysis of the short-range data by McDaniel indicated that, for signals received on the vertical array from the small charges detonated at 17 m, sufficient suppression of the second mode was obtained. By selecting the array hydrophone (number 5 from the bottom) nearest the node for the third mode, excellent suppression of both modes two and three was obtained. The data was then processed as described in Chapter III for the calculation of the received energy using a single hydrophone. The mode-attenuation coefficients for the first mode were calculated by McDaniel for one-third-octave center frequencies of 40 to 500 Hz and are presented in Table 8 along with the 95 percent confidence limits on the coefficients.

The signals received along the constant-depth leg (Leg J) of the long-range propagation experiment were analyzed in one-third-octave bands with center frequencies from 160 to 500 Hz. The received energy was calculated from signals received on the top hydrophone of the bottom unit (one meter above the bottom) according to the procedure described in Chapter III for a single hydrophone. The received energy was then corrected for relative gain and cylindrical spreading and is plotted in Figure 19. The straight lines shown represent a least-squares straight-line fit to the data points. The mode-attenuation coefficients (for the first mode) obtained from the straight lines are listed in Table 9.

#### 4.4.2 Bottom model--Site 2.

A bottom model for Site 2 was constructed from seismic-refraction experiments performed during the 1973 and 1976 tests, the short-range seismic experiment performed in 1973, and dispersion analysis performed on shots from the 1976 tests.

TABLE 8

MODE-ATTENUATION COEFFICIENT ( $\delta$ )---SITE 2, LEGS G AND H

## Daytona Beach

<u>Leg</u>	<u>Frequency (Hz)</u>	<u>Mode-Attenuation Coefficient (<math>\delta</math>) (dB/km)</u>	<u>95% Confidence Interval</u>	
			<u>Upper Limit</u>	<u>Lower Limit</u>
G	40	2.60	2.93	2.27
	63	1.78	2.07	1.49
	100	1.28	1.55	0.98
	160	0.92	1.05	0.79
	200	0.80	0.85	0.75
	250	0.62	0.67	0.58
	315	0.50	0.73	0.28
	400	0.40	0.52	0.28
	500	0.32	0.47	0.18
H	40	5.28	6.65	3.91
	63	4.97	6.02	3.92
	100	2.91	3.19	2.64
	160	1.11	1.21	1.00
	200	0.75	0.88	0.63
	250	0.78	0.94	0.62
	315	0.41	0.65	0.16
	400	0.40	0.52	0.28
	500	0.32	0.47	0.18



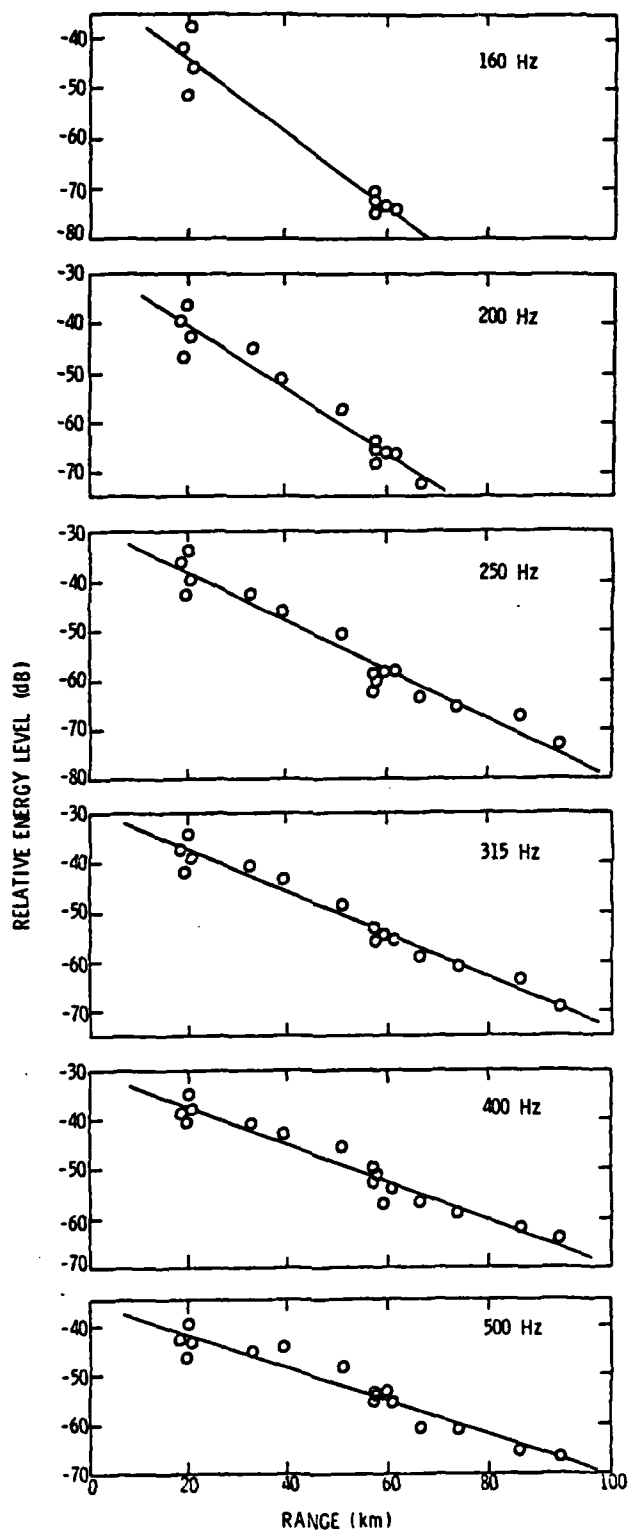


Figure 19. Relative Energy Levels--Daytona Beach Site 2, Leg J

TABLE 9

MODE-ATTENUATION COEFFICIENT ( $\delta$ )--SITE 2, LEG J

Daytona Beach

Frequency (Hz)	Mode-Attenuation Coefficient ( $\delta$ ) (dB/km)	<u>95% Confidence Interval</u>	
		<u>Upper Limit</u>	<u>Lower Limit</u>
160	0.75	0.92	0.58
200	0.65	0.76	0.54
250	0.50	0.57	0.43
315	0.43	0.48	0.38
400	0.38	0.43	0.33
500	0.34	0.39	0.28

---

The seismic-refraction results are summarized in Table 10 where they are also compared with work by Hersey et al. (1950), and Worzel and Ewing (1948). These models were tested through the use of dispersion analysis and the results are plotted in Figure 20. The three-layer model shown in the figure gave the best match to the experimental data and, although this model differed somewhat from the other results in that the first layer thickness was much less, it was confirmed by the results from the short-range seismic experiment [described by McDaniel (1980)]. Such an experiment provided better resolution for detecting thin layers than experiments using larger charges and greater source-receiver separations.

4.4.3 Experimental sediment absorption--Site 2. Once a bottom model is established, it may be used in the normal-mode model and the distribution of energy among the bottom layers determined. This was done using the three-layer bottom model in Figure 20. By assuming the absorption coefficient was the same for both bottom layers, the energy ratios were summed and the bottom-absorption coefficients were calculated from experimental mode-attenuation coefficients as described in Chapter II. The results of these calculations are presented in Table 11 for the two short-range legs (G and H) and the long-range leg (J).

4.4.4 Predicted bottom absorption--Site 2. As noted in the discussion on Site 1, grab-sample or core data is required to obtain input parameters for the sediment model. At Site 2, the grab-samples noted previously (reported by Milliman et al.) provided adequate sampling, particularly near the long-range propagation leg. In

TABLE 10

## SUMMARY OF SEISMIC-REFRACTION WORK--Site 2

Daytona Beach							<u>Data Source</u>
<u>C<sub>1</sub></u> (m/sec)	<u>H<sub>1</sub></u> (m)	<u>C<sub>2</sub></u> (m/sec)	<u>H<sub>2</sub></u> (m)	<u>C<sub>3</sub></u> (m/sec)	<u>H<sub>3</sub></u> (m)	<u>C<sub>4</sub></u> (m/sec)	
1723	38	1884	177	2271	478	3820	1973 Seismic Refraction
1754	86	2382	186	3140	763	5033	1976 Seismic Refraction
1723	6	2222	∞	- -	- -	- -	1973 Short-Range Seismic
1760	80	2420	200	3160	420	4260	Hersey et al. (1950)
1631	305	2950	686	4063	∞	- -	Worzel and Ewing (1948)

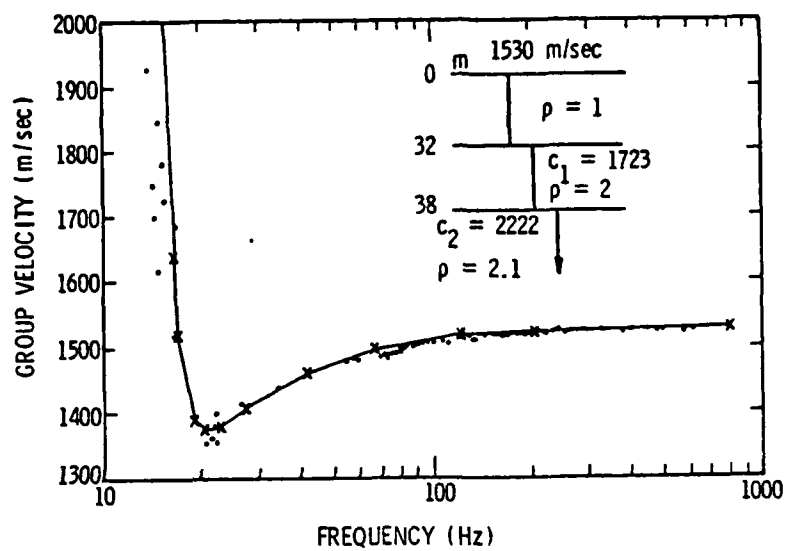


Figure 20. Daytona Beach Experimental and Model Dispersion--Site 2

TABLE 11

ENERGY DISTRIBUTION ( $\gamma$ ) AND BOTTOM-  
 ABSORPTION COEFFICIENTS ( $\alpha_A$ )--SITE 2

Daytona Beach

Frequency (Hz)	$\gamma^{(1)}$	$\gamma^{(2)}$	$\gamma$	$\alpha_A$ (dB/km)		
				$G$	$H$	$J$
50	0.07091	0.02548	0.09639	26.97	54.78	- -
63	0.04297	0.00592	0.04889	36.41	101.66	- -
100	0.02211	0.00097	0.02308	55.46	126.08	- -
160	0.00909	0.00008	0.00917	100.33	121.05	81.79
200	0.00551	0.00002	0.00553	144.67	135.62	117.54
250	0.00319	- -	0.00319	194.36	244.51	156.74
315	0.00175	- -	0.00175	285.71	234.29	245.71
400	0.00091	- -	0.00091	439.56	439.56	417.58
500	0.00048	- -	0.00048	666.67	666.67	708.33

addition, a single core obtained by the Naval Research Laboratory (NRL) is indicated near Site 2 in Figure 10. By selecting those grab-samples closest to the point where Leg J crosses the sample line, the data in Table 12 was obtained. Data for the NRL core (averaged over the 40 cm core length) is also presented in the table. From the average mean grain-size ( $M_z$ ) and sorting ( $\sigma_\phi$ ) for the grab-samples, the permeability ( $K$ ) and pore-size parameter ( $a$ ) were calculated and the sediment model input parameters in Table 13 assumed. The bulk modulus for the mineral frame ( $k_r$ ) was calculated using the VRH method by assuming a mineral content of 60 percent calcium carbonate and 40 percent quartz. With these input parameters, the Biot sediment model was run and the absorption values in Table 14 were predicted.

4.4.5 Discussion of results--Site 2. The absorption predicted by the sediment models and that obtained from experimental mode-attenuation coefficients is compared in Figure 21. Also shown is the absorption predicted by Hamilton for the sediment mean grain-size found at Site 2. As may be seen, the absorption predicted by both techniques is somewhat lower than that obtained experimentally below 150 Hz. As noted in the discussion on Site 1, this is probably due to the depth of penetration into the bottom occurring at the lower frequencies [note  $\gamma^{(2)}$  in Table 18]. The volume absorption coefficients for the deeper layers are unknown; however, it is probable that attenuation due to conversion to shear waves occurs since McDaniel (1980) found that the shear velocity of the second bottom layer is higher (670 m/sec) than the value assume here. At frequencies above 150 Hz, the energy tends to be concentrated in the first bottom layer and, as may be seen in the

TABLE 12

## GRAB-SAMPLE AND CORE DATA--SITE 2

## Daytona Beach

Sample Number	$M_z$ (phi)	$\sigma_\phi$ (phi)	Percent CaCO <sub>3</sub>	$\beta$	$\rho$ (g/cm <sup>3</sup> )
1379	0.43	1.77	62.1	--	--
1380	0.96	0.65	47.3	--	--
1381	1.20	0.69	56.2	--	--
1382	0.11	1.76	64.5	--	--
1383	1.33	0.44	62.3	--	--
1384	1.02	0.59	55.1	--	--
1385	1.05	0.47	52.5	--	--
1386	1.15	0.58	59.3	--	--
1387	0.61	0.58	58.9	--	--
1388	0.66	0.74	66.4	--	--
Average	0.85	0.83	58.5	--	--
NRL Core	0.59	1.21	—	0.38	2.06

---

Note:  $\phi = -\log_2 d$  ; d is the mean grain diameter in mm.

---



TABLE 13  
SEDIMENT MODEL PARAMETERS--SITE 2

Daytona Beach

$M_z$ (phi)	$\sigma_\phi$ (phi)	$K$ (cm <sup>2</sup> )	$a$ (cm)	$\beta$	$\rho$ (g/cm <sup>3</sup> )	$k_r$ (dyne/cm <sup>2</sup> )
0.85	0.83	$7.5 \times 10^{-7}$	$3.3 \times 10^{-3}$	0.38	2.06	$5.6 \times 10^{11}$

Note: Other input parameters identical to Table 6.

TABLE 14

PREDICTED SEDIMENT ABSORPTION ( $\alpha_A$ )--SITE 2

Daytona Beach

$M_z$	$\sigma_\phi$	$\alpha_A$ (dB/km)					
		40 Hz	100 Hz	200 Hz	300 Hz	400 Hz	500 Hz
0.85	0.83	6.6	39.3	141.8	278.2	421.1	553.5

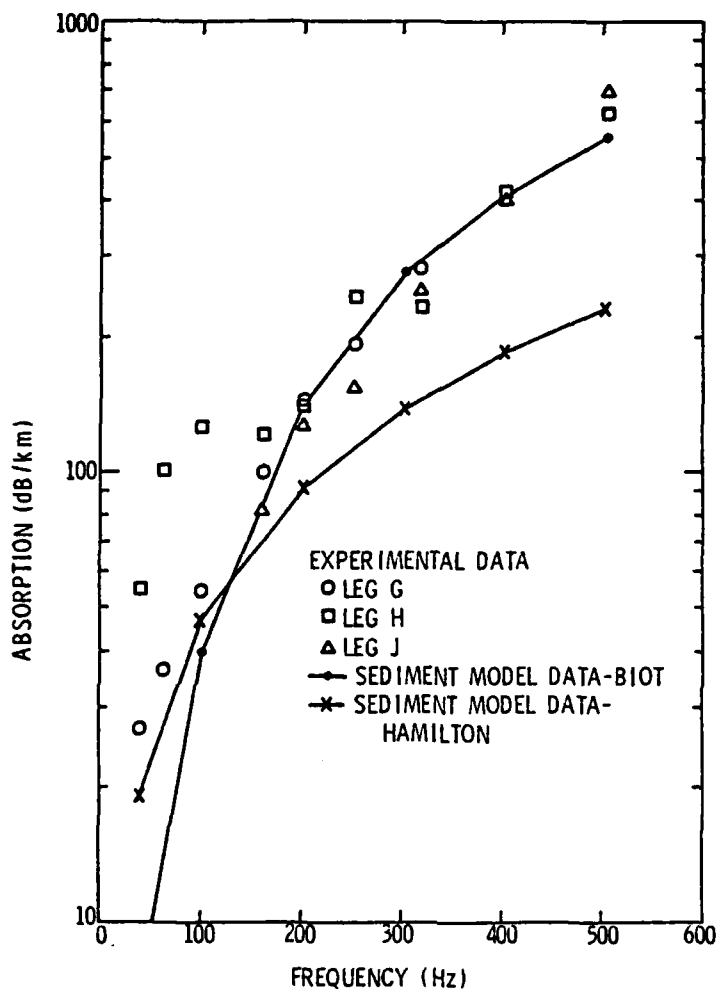


Figure 21. Comparison of Experimental and Predicted Bottom Absorption-- Daytona Beach Site 2

figure, the predicted and experimental absorption agree much better. The absorption predicted by Hamilton's regression formula matches somewhat better at low frequency but gives poorer agreement than the Biot model at high frequency.

#### 4.5 Comparison of Results at Site 1 and Site 2

Although Sites 1 and 2 are separated by only about 37 km, some difference does exist in the surficial sediments which appears to be reflected in the modal attenuation. As discussed in the previous sections, the surficial sediment at Site 1 is best characterized as a moderately-sorted ( $\sigma_\phi = 0.84$ ), medium sand ( $M_z = 1.44$ ) with a calcium carbonate content of approximately 30 percent. A coarser sediment ( $M_z = 0.86$ ) with nearly the same sorting, but with a calcium carbonate content twice that of Site 1, exists at Site 2. Based on dispersion studies, the uppermost layers are on the average very thin, i.e., 4 m at Site 1 and 6 m at Site 2. The compressional sound speed in these layers is consistent with the average grain-sizes in that the finer sediment has the lower sound speed. In both cases, the next layer is relatively thick; however, the compressional velocity of the half-space assumed for Site 2 is somewhat larger (2200 m/sec) as compared to that of the second bottom layer at Site 1 (1800 m/sec).

The mode-attenuation coefficients measured at Sites 1 and 2 are comparable (except for Leg H at Site 2) at low frequency; however, at the higher frequencies, the mode attenuation at Site 1 is roughly twice that found at Site 2. Because of this, Leg H at Site 2 and the 750 Hz data at Site 1 have been deleted from further comparisons.

Kibblewhite and Denham (1966) note that, at high frequencies, the mode attenuation for the first mode  $\delta_1$  should follow the relation

$$\delta_1 \sim \frac{\alpha_A}{H^3} \quad (49)$$

Thus, for the same sediment type, the mode attenuation is proportional to  $H^{-3}$ , where  $H$  is the water depth. It follows then that the mode attenuation at Site 1 should be larger. If the ratio of the mode attenuation at Site 1 to that at Site 2 is calculated based on Equation (49) (assuming  $\alpha_A$  the same), then the attenuation at Site 1 should be 3.8 times that at Site 2. An examination of Table 3 and Table 9 indicates that this does not hold true; hence, if we assume that Equation (49) is valid, then the bottom-absorption coefficients ( $\alpha_A$ ) for the two sites must be different. This is confirmed by the bottom-absorption coefficients calculated from the mode-attenuation coefficients. These differences are readily apparent in Table 15 where power-law fits have been calculated for the experimental and the predicted bottom-absorption coefficients. The experimental relations for Site 2 show some variation in magnitude. This may be due to the high shear speed recently determined for this leg by McDaniel. The differences noted in sediment type for the two sites, although small, are reflected in the bottom absorption predicted by both the Biot and Hamilton methods. Over the frequency ranges discussed (50 to 600 Hz at Site 1 and 40 to 500 Hz at Site 2), the absorption predicted by the Biot theory provides better agreement over the greatest proportion of the frequency range. This appears to indicate that a frequency dependence other than  $f^1$  is required.

TABLE 15

## POWER-LAW FITS TO BOTTOM-ABSORPTION

COEFFICIENTS ( $\alpha_A$ )--SITES 1 AND 2

Daytona Beach

<u>Site</u>	<u>Leg</u>	Experimental $\alpha_A$ (dB/km)	Predicted $\alpha_A$ (dB/km)	
			<u>Riot</u>	<u>Hamilton</u>
1	E	$0.013 f^{1.65}$	$0.004 f^{1.84}$	$0.49 f$
	F	$0.013 f^{1.65}$		
2	G	$0.179 f^{1.28}$	$0.011 f^{1.76}$	$0.47 f$
	J	$0.005 f^{1.88}$		

---

Note: The frequency  $f$  is in Hertz.

---

## CHAPTER V

### BOTTOM-ABSORPTION ANALYSIS

### CORPUS CHRISTI EXPERIMENTS

#### 5.1 Introduction

In the previous chapter, data were analyzed from a test site where the sediments were in the medium-to-coarse sand range. The clay and silt sediments found off the coast of Corpus Christi, Texas, provide test data at the extreme end of the grain-size scale. Cores were obtained at the test site and were analyzed for sediment parameters which provide the basis for bottom-absorption predictions.

The procedure followed is much the same as that followed in the preceding chapter. The experimental program is defined, and received energy and mode-attenuation coefficients calculated. The bottom model derived is somewhat unique for continental-shelf areas in that the uppermost sedimentary layer has a sound speed less than that of the water column. This model is used in the normal-mode program to calculate energy ratios and, hence, experimental bottom absorption. The experimental values are then compared with absorption predicted by the sediment models.

#### 5.2 Experiments

During April 1977, experiments were performed off the coast of Corpus Christi, Texas. Short-range and long-range propagation and seismic-refraction experiments were performed as described in Chapter III; however, only constant-depth leg results are considered here.

Both short-range and long-range propagation data were analyzed by Rubano (1980) for the site and legs shown in Figure 22. The water depth at the receiver was 30.5 m and varied by less than 0.5 m along the short-range constant-depth leg. The maximum range attained was 14.7 km. For the short-range tests, small (7.1 g) charges were detonated at depths of 9.5 and 19 m. The new vertical array was used as the receiver.

Long-range data were obtained using an aircraft to drop SUS charges, set to detonate at a depth of 18.3 m, out to a range of 77.6 km along the constant-depth track. The bottom-sensor unit was in place for the long-range tests; hence, the top hydrophone (1 m above the bottom) was used as the receiver for these tests. Along this leg, the bathymetry varied as shown in Figure 23.

Seismic-refraction analysis was performed on data obtained along the constant-depth leg out to 12 km in range. A 12 kHz fathometer was towed over the same leg, yielding bottom and shallow sub-bottom data. A total of four cores, which will be discussed later, were obtained for this site. Sound-velocity profiles obtained along both tracks showed a very slight positive gradient.

### 5.3 Analysis of Data

The received energy (corrected for cylindrical spreading) was calculated for short-range and long-range data, and mode-attenuation coefficients were obtained for the first normal mode. The bottom model derived by Rubano (1980), from dispersion and seismic-refraction analysis, was used in a four-layer normal-mode program to calculate the energy ratios for each layer. Experimental bottom-absorption

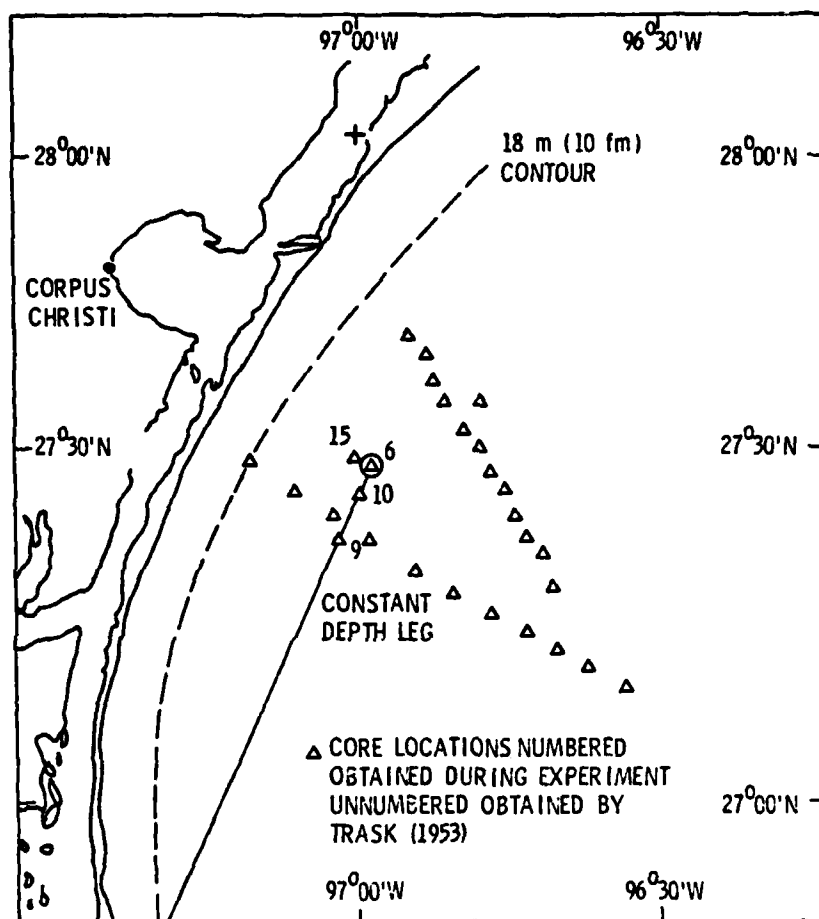


Figure 22. Corpus Christi Test Area



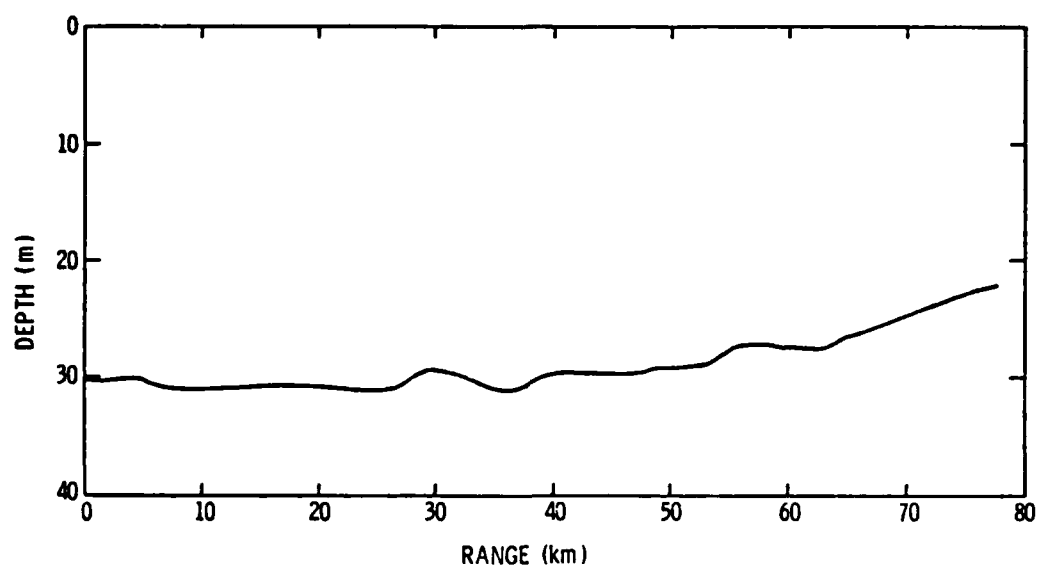


Figure 23. Depth Profile--Corpus Christi, Long-Range Leg

coefficients were then calculated. Bottom absorption was predicted by the sediment models, using input data based on the analysis of the cores obtained at the site, and compared with the experimental results.

#### 5.3.1 Received-energy and mode-attenuation calculations.

Short-range data were obtained for ranges from 1.0 to 14.7 km and for frequencies from 25 to 400 Hz. Energy received on the bottom hydrophone of the array was analyzed for the small charges detonated at a depth of 19.5 m. Rubano (1980) noted that the portion of the signal due to the first mode was well separated in time from the higher-order mode arrivals (basically, the second mode). Hence, the data from a single hydrophone of the array was processed using temporal separation to obtain the first mode. Two shots were analyzed for each of ten range points (at most frequencies) spaced over the range interval noted above. Both shots were averaged to obtain the plot of relative received energy shown in Figure 24. A least-squares, straight-line fit was calculated for all of the data points at each frequency and is also plotted in the figure. The mode-attenuation coefficients obtained from the slope of this straight line are listed in Table 16 with the calculated 95 percent confidence-interval limits for the slope. Note that only data up to 250 Hz is presented, whereas received energy was calculated out to 400 Hz. This limitation is imposed due to unusual propagation effects, which will be discussed later, that occurred at the higher frequencies.

Long-range data were analyzed for ranges from 18.5 to 55.6 km over a nominal frequency range of 25 to 250 Hz. Shots were detonated to a range of 77.6 km; however, beyond 55.6 km, the signal-to-noise ratio was inadequate for data analysis. The relative received energy

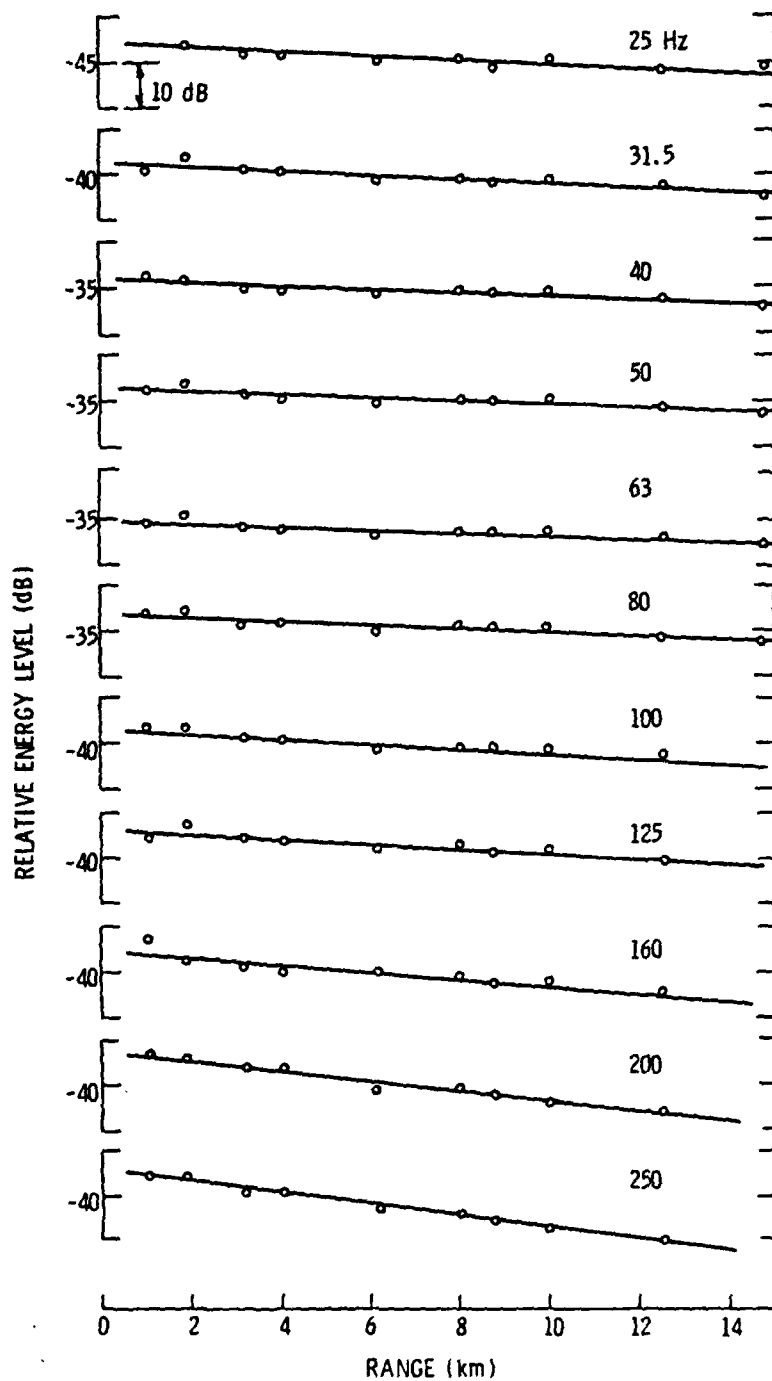


Figure 24. Relative Energy Levels--Corpus Christi, Short-Range Data

TABLE 16

SHORT-RANGE MODE-ATTENUATION COEFFICIENT ( $\delta$ )

## Corpus Christi

<u>Frequency (Hz)</u>	<u>Mode-Attenuation Coefficient (dB/km)</u>	<u>95% Confidence Interval</u>	
		<u>Upper Limit</u>	<u>Lower Limit</u>
25	0.48	0.64	0.32
31.5	0.45	0.58	0.32
40	0.38	0.50	0.26
50	0.36	0.49	0.24
63	0.33	0.45	0.22
80	0.45	0.59	0.32
100	0.56	0.70	0.42
125	0.53	0.71	0.35
160	0.83	1.03	0.63
200	1.13	1.30	0.96
250	1.29	1.42	1.15

---

was calculated using corrections for gain and cylindrical spreading and is plotted in Figure 25 for each frequency. The mode-attenuation coefficients obtained from the straight-line fits to these data are listed in Table 17.

5.3.2 Bottom model. The bottom model derived by Rubano is presented in Figure 26. The four-layer model is based on seismic-refraction and dispersion analysis. Note that the upper sediment layer has a sound speed less than that found in the water column. This low velocity (1490 m/sec) is consistent with the grain-size and velocity measurements obtained from analysis of the four cores. The effect of the low sound speed in this layer is to trap bottom-incident energy above a frequency (estimated by Rubano) of 250 Hz. This is recognized as the angle of intromission effect associated with the plane-wave reflection and transmission coefficients, in which the reflected signal goes to zero for certain frequencies and angles of incidence. Since the measured losses are directly related to this phenomenon, the frequency range for the data presented is limited to 250 Hz.

The bottom model derived by Rubano appears to be consistent with other data from the literature. Although the closest seismic-refraction data to be found are roughly 300 km to the northeast, near Galveston, Texas, the velocities shown in Table 18 are in general agreement with the model. These studies by Ewing, Antoine, and Ewing (1960), and Antoine and Ewing (1963), also agree in general with seismic-refraction results obtained very near the test site in water 18 m deep. A low-velocity layer is not reported in these references. However, seismic-refraction analysis assumes that the velocity always increases with

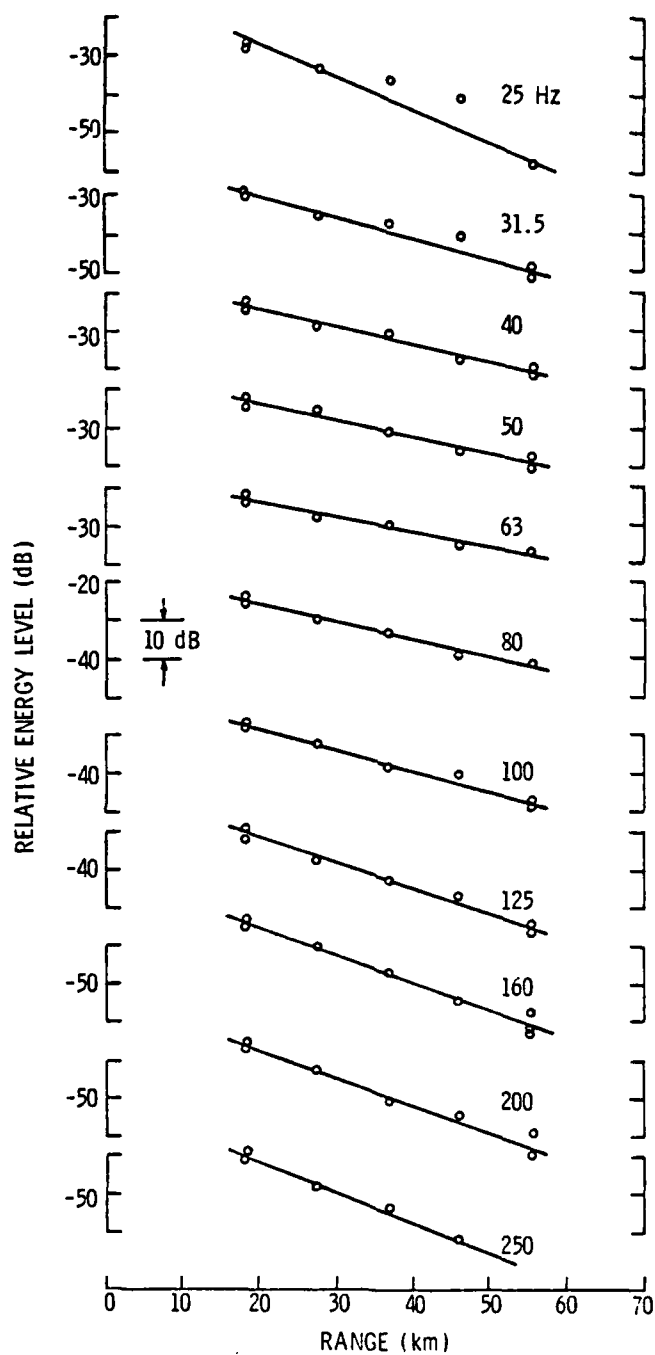


Figure 25. Relative Energy Levels--Corpus Christi, Long-Range Data

TABLE 17

LONG-RANGE MODE-ATTENUATION COEFFICIENT ( $\delta$ )

Corpus Christi

Frequency (Hz)	Mode-Attenuation Coefficient (dB/km)	95% Confidence Interval	
		Upper Limit	Lower Limit
25	0.86	1.09	0.63
31.5	0.56	0.65	0.47
40	0.47	0.51	0.42
50	0.43	0.49	0.38
63	0.40	0.43	0.36
80	0.46	0.51	0.42
100	0.56	0.61	0.51
125	0.67	0.73	0.62
160	0.72	0.79	0.65
200	0.73	0.83	0.63
250	0.79	0.86	0.72

---

CORPUS CHRISTI BOTTOM MODEL  
RUBANO (1980)

30.5 m	$c_w = 1512$ $\rho_w = 1.0$
4 m	$C_1 = 1490$ $\rho_1 = 1.4$
31 m	$C_2 = 1700$ $\rho_2 = 1.7$
	$C_3 = 1830$ $\rho_3 = 2.0$

Figure 26. Corpus Christi Bottom Model



TABLE 18

## SEISMIC-REFRACTION DATA

Corpus Christi						<u>Data Source</u>
<u>C<sub>1</sub></u> (m/sec)	<u>H<sub>1</sub></u> (m)	<u>C<sub>2</sub></u> (m/sec)	<u>H<sub>2</sub></u> (m)	<u>C<sub>3</sub></u> (m/sec)	<u>H<sub>3</sub></u> (m)	
1700	310	2200	1200	2900	5500	Ewing, Antoine and Ewing (1960)
1700	188	1900	437	2300	1375	Antoine and Ewing (1963)
1651	43	1775	453	2192	340	Seismic Refraction at Site
					2767	

depth; hence, the referenced refraction results do not include the low-velocity layer. In addition, layer thicknesses will be in error due to neglect of the low-velocity layer. Thus, the bottom model of Rubano is considered to be valid.

5.3.3 Experimental bottom absorption. Using the four-layer bottom model and normal-mode program, energy ratios for the sub-bottom layers were calculated. These values are shown in Table 19 where  $\gamma$  is the sum of the values for the individual layers. With  $\delta$  known for each frequency, the experimental bottom absorption ( $\alpha_A$ ) was calculated by dividing the mode-attenuation coefficients for the first mode in Tables 16 and 17 by the appropriate value of  $\gamma$ . These coefficients are also listed in Table 19.

5.3.4 Predicted bottom absorption. During the experimental program, four cores were obtained near the 30 m test site. The cores were analyzed by the Geological Laboratory of the Naval Oceanographic Office where velocities ranging from 1490 to 1500 m/sec were measured through the cores. Grain-size measurements on the cores show that this thin layer consists of a very poorly sorted, medium-to-fine silt. A summary of the data provided by the core analysis is listed in Table 20. The grain-sizes listed represent the maximum and minimum values within each core except for core number 10 where only one value was used. The dominant constituents of the cores were quartz sand and shell fragments. Cores obtained by other researchers are indicated in Figure 22. Trask (1953) analyzed these cores for organic content, chemical composition, and water content, and found median grain-sizes averaging 7.5 phi and calcium carbonate content averaging 3.4 percent near the numbered cores.

TABLE 19

ENERGY DISTRIBUTION ( $\gamma$ ) AND  
 BOTTOM-ABSORPTION COEFFICIENTS ( $\alpha_A$ )

Corpus Christi

Frequency (Hz)	$\gamma$ (1)	$\gamma$ (2)	$\gamma$ (3)	$\gamma$	$\alpha_A$ (dB/km)	
					Short Range	Long Range
25	0.1016	0.3886	0.0897	0.5799	0.83	1.48
31.5	0.1145	0.2816	0.2230	0.4184	1.08	1.34
40	0.1143	0.1788	0.0043	0.2974	1.28	1.58
50	0.1074	0.1119	0.0007	0.2200	1.64	1.95
63	0.0974	0.0681	$8.2 \times 10^{-5}$	0.1656	1.99	2.42
80	0.0868	0.0410	$5.9 \times 10^{-6}$	0.1278	3.52	3.60
100	0.0780	0.0258	- -	0.1038	5.39	5.39
125	0.0711	0.0166	- -	0.0877	6.04	7.64
160	0.0668	0.0106	- -	0.0774	10.72	9.30
200	0.0673	0.0076	- -	0.0749	15.09	9.75
250	0.0756	0.0062	- -	0.0818	15.77	9.66

TABLE 20

## CORE DATA-MAXIMUM AND MINIMUM GRAIN SIZES

## Corpus Christi

<u>Core Number</u>	<u>Length (cm)</u>	<u>M<sub>z</sub> (phi)</u>	<u><math>\sigma_{\phi}</math> (phi)</u>	<u><math>\rho_r</math> (g/cm<sup>3</sup>)</u>	<u><math>\rho</math> (g/cm<sup>3</sup>)</u>	<u><math>\beta</math></u>
6	47	6.07	2.00	2.67	1.82	0.51
6	47	8.78	2.13	2.73	1.52	0.70
9	69	6.37	2.19	2.67	1.58	0.65
9	69	8.78	2.10	2.73	1.48	0.72
10	59	8.67	2.17	2.71	1.51	0.70
15	36	6.51	2.61	2.67	1.73	0.56
15	36	8.38	2.36	2.68	1.57	0.66

These results suggest that the data in Table 20 is representative of the test area and that the mineral composition of the sediment frame may be considered pure quartz (since the carbonate content is low).

Using the data in Table 21, sediment model runs (with the Biot model) were made to predict the absorption within the sedimentary layer. The permeability (K) and pore-size parameters (a) were calculated from the mean grain-size ( $M_z$ ) and the standard deviation ( $\sigma_\phi$ ) as described in Chapter II. The densities and porosities are measured data from the core analysis. Note that values different than those used in Chapter IV are used for  $\alpha$ ,  $\Delta_s$  and  $\Delta_E$  for the fine sediments found at this site. These values are recommended by Stoll (1974) as providing the best fit to the fine-grained experimental data of Wood and Weston (1964).

The results of the sediment model runs are listed in Table 21. As may be seen, the range of absorption values predicted is rather small for the mean grain-sizes used. If the absorption is expressed in the power law form,  $\alpha_A = K_A f^n$ , by calculating a power-law fit to the absorption as a function of frequency, the exponent  $n$  is one in all cases and  $K_A$  varies between 0.052 and 0.061 dB/km·Hz. A typical value for the absorption is  $\alpha_A = 0.057 f$ . Rubano found by trial and error that the bottom absorption was  $0.005 f^{1.1}$  nepers/m or in the units used here,  $\alpha_A = 0.022 f^{1.1}$  dB/km.

#### 5.4 Discussion of Results

The results of the experimental and predicted bottom-absorption calculations are plotted in Figure 27. Two different prediction equations, from the models of Hamilton and Biot, are compared with both

TABLE 21  
BIOT SEDIMENT MODEL PARAMETERS AND PREDICTED BOTTOM ABSORPTION ( $\alpha_A$ )

Corpus Christi

Core No.	K (cm <sup>2</sup> )	a (cm)	Absorption (dB/km)							
			25 Hz	50 Hz	80 Hz	100 Hz	160 Hz	200 Hz	250 Hz	
6	$1.23 \times 10^{-10}$	$4.29 \times 10^{-5}$	1.53	3.07	4.91	6.14	9.83	12.29	15.37	
6	$2.47 \times 10^{-12}$	$6.08 \times 10^{-6}$	1.36	2.72	4.35	5.44	8.71	10.88	13.60	
9	$6.33 \times 10^{-11}$	$3.08 \times 10^{-5}$	1.43	2.85	4.56	5.70	9.13	11.41	14.27	
9	$2.57 \times 10^{-12}$	$6.20 \times 10^{-6}$	1.30	2.61	4.17	5.22	8.35	10.43	13.04	
10	$2.77 \times 10^{-12}$	$6.44 \times 10^{-6}$	1.35	2.69	4.31	5.38	8.62	10.77	13.46	
15	$2.96 \times 10^{-11}$	$2.10 \times 10^{-5}$	1.53	3.05	4.88	6.10	9.76	12.21	15.26	
15	$3.11 \times 10^{-12}$	$6.80 \times 10^{-6}$	1.42	2.83	4.53	5.66	9.06	11.33	14.16	

Note:  $k_r = 3.8 \times 10^{11}$  dyne/cm<sup>2</sup>

$k_f = 2.4 \times 10^{10}$  dyne/cm<sup>2</sup>

$\eta = 0.1$  dyne-sec/cm<sup>2</sup>

$\alpha = 3.0$

$v_E = 3 \times 10^4$  cm/sec

$v_s = 2.1 \times 10^4$  cm/sec

$\Delta_E = 0.45$

$\Delta_s = 0.60$

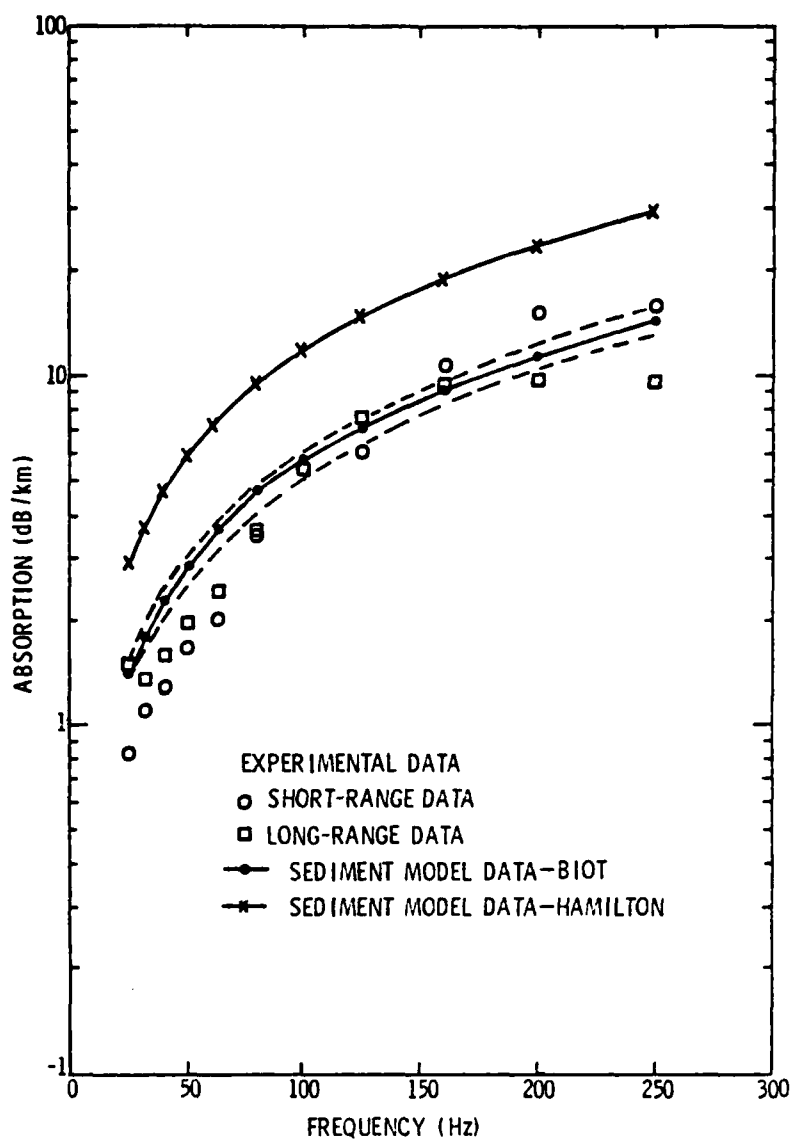


Figure 27. Comparison of Experimental and Predicted Bottom Absorption--Corpus Christi

short-range and long-range calculations of bottom absorption from Table 19. Both model predictions, shown by the solid lines, are based on the largest mean grain-size for core 9 (6.37 phi). The range of values predicted by the Biot model, based on the mean grain-sizes from the core data, is indicated by the dotted lines in the figure. If a prediction based upon porosity is calculated with the Hamilton model, the values are even larger. As can be seen, the predictions by Hamilton are much too large over the entire frequency range, whereas the predictions based on the Biot model give good agreement except at low frequencies. It might be expected that the predictions are poorest at the low frequencies where significant energy penetrates to the second and third layers. In calculating the experimental bottom absorption, it was assumed that the attenuation was the same in all of the bottom layers. This is probably not true and, at low frequencies with deep penetration, this is reflected in poorer agreement between experimental and predicted absorption. For the data in Figure 27, the best agreement occurs from 100 to 250 Hz for the short-range data. Over this frequency range, 75 to 92 percent of the bottom energy is in the first layer, as is shown in Table 19. Thus, it appears that the predictive ability of the sediment models is best assessed over this frequency range at the Corpus Christi test site.



## CHAPTER VI

### BOTTOM-ABSORPTION ANALYSIS

#### PANAMA CITY EXPERIMENTS

##### 6.1 Introduction

Using mode-attenuation data from the literature, experimental and predicted bottom absorption was calculated for constant-depth propagation paths in water depths of 18.3 and 30.5 m. The seabed in Panama City test areas consisted of moderately well-sorted, fine-to-medium sand with a carbonate content of approximately 18 percent. The area was similar to the Daytona Beach test area in terms of the surficial sediments, but differed in the sub-bottom structure. A separate environmental measurement and analysis program conducted by the University of Texas at Galveston provided new and refined data which were used in modeling the sub-bottom structure.

##### 6.2 Experiments

Shallow-water propagation experiments were performed off the coast of Panama City, Florida, in January, April, and June of 1976. The experiments to be discussed here were performed using the vertical array (LC-10 array) during the June time-period. Mode-attenuation data were obtained along the two short-range propagation legs shown in Figure 28. Seismic-refraction data were also obtained and analyzed. Cores were obtained and analyzed by the University of Texas at Galveston.

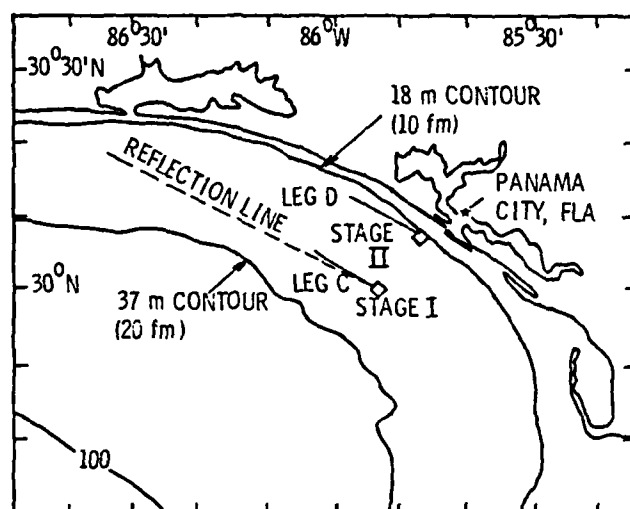


Figure 28. Panama City Test Sites

At each site, the receiving array was cabled directly to an oceanographic platform: Stage I in 30.5 m of water, and Stage II in 18.3 m of water. From Stage I, short-range data were obtained out to a maximum range of 17.8 km along a constant-depth track (Leg C) in water 30.5 m deep. Short-range data were obtained from Stage II out to a maximum range of 17 km along constant-depth Leg D (18.3 m water depth). The receiving array for the experiment from Stage II was shortened, using five of the eight hydrophones; the remaining three were coiled at the surface. The signal sources for both experiments were the small (7.1 g) charges. These charges were detonated at depths of 9.5 m and 19.2 m along Leg C, and 5.8 and 11.3 m along Leg D. In both cases, the shallow source was predicted to (and, in fact, did) maximize the excitation of the second mode, while the deeper source was designed to minimize the second mode.

The water depth along both tracks was determined to be essentially constant. The sound-velocity profiles obtained during the experiment showed only a slight variation with range. The profiles used in the analysis were typical of those obtained and will be presented with the bottom models in a later section.

### 6.3 Analysis of Data

Propagation along both Legs C and D was analyzed extensively by Caswell (1979). Using array processing of the data to select the desired modes, he obtained mode-attenuation coefficients for the first mode over a frequency range of 50 to 750 Hz along Leg C and 100 to 750 Hz along Leg D. The attenuation of the second and third modes was also obtained for portions of the data.

6.3.1 Mode-attenuation coefficients. By processing the short-range data along Legs C and D using the array techniques described in Chapter III, the mode-attenuation coefficients listed in Table 22 were obtained by Caswell. Along Leg C, these results may be compared with those of Ingenito (1973). At 400 Hz, Ingenito reported a mode-attenuation coefficient of  $0.61 \pm 0.19$  dB/km within 95 percent confidence limits, giving reasonable agreement with the results of Caswell ( $0.85 \pm 0.08$ ). However, at 750 Hz, Ingenito found mode attenuation of  $0.30 \pm 0.39$  dB/km, while Caswell found attenuation of  $1.28 \pm 0.24$  dB/km. The reason for the difference at 750 Hz is not apparent from either paper.

6.3.2 Bottom model. A valid bottom model is necessary to calculate the experimental bottom-absorption coefficients from the mode-attenuation values listed in Table 22. An incorrect choice of bottom parameters can lead to large errors in the calculated absorption coefficients since the modal energy distribution and, hence, the energy ratios are dependent upon these parameters. The bottom models selected by Caswell and Ingenito are quite different as may be seen in Table 23. The key parameter here is the sound speed of the first bottom layer ( $c_1$ ). While substantial differences exist in the choice of these parameters, the effect of these differences is not easily assessed because of the differences in mode attenuation noted in the previous paragraph. As will be discussed in the summary of this chapter, the results of bottom-absorption calculations by Caswell and Ingenito are remarkably close in their frequency dependence.

TABLE 22

MODE-ATTENUATION COEFFICIENT ( $\delta$ )

[Caswell (1979)]

Panama City

<u>Leg</u>	<u>Frequency (Hz)</u>	<u>Mode-Attenuation Coefficient (dB/km)</u>	<u>95% Confidence Interval</u>	
			<u>Upper Limit</u>	<u>Lower Limit</u>
C	50	1.80	2.14	1.46
	100	1.22	1.36	1.08
	200	1.01	1.23	0.89
	400	0.85	0.93	0.77
	600	0.91	1.05	0.77
	750	1.28	1.04	1.52
D	100	2.25	2.56	1.94
	200	1.96	2.18	1.74
	400	1.70	1.86	1.54
	600	1.77	1.55	1.99
	750	1.68	1.96	1.40

---

TABLE 23

## OTHER BOTTOM MODELS FOR PANAMA CITY

<u>Leg</u>	<u>Bottom Parameters</u>				<u>Bottom Model Source</u>
	<u>C<sub>1</sub></u> <u>(m/sec)</u>	<u>H<sub>1</sub></u> <u>(m)</u>	<u>C<sub>2</sub></u>	<u>H<sub>2</sub></u>	
C	1711	3.8	2100	$\infty$	Caswell (1979)
D	1708	$\infty$	- -	- -	Caswell (1979)
C	1589	$\infty$	- -	- -	Ingenito (1973)

The bottom parameters in Table 23 were based on the best available information at the time the analysis was performed. More recently, however, results of refraction and reflection analysis, core analysis, and in-situ sound-velocity measurements performed by personnel of the Marine Science Laboratory of the University of Texas at Galveston have become available. Addy et al. (1979) correlated the results of sub-bottom reflection surveys with sediment lithology based on long piston cores. McMillan et al. (1978) discussed the sediments of the test area (again, based on the cores) in detail. Velocity measurements were made in-situ using a velocimeter placed in the cutting head of the coring apparatus [see Shirley and Anderson (1975)]. Using data from the reflection surveys, Houston (1978) performed a refraction analysis of this data and obtained both velocities and layering of the sub-bottom structure within the test area.

The environmental models used in this study for Legs C and D are listed in Table 24. The sound-velocity profiles are those used by Caswell as representative of the complete propagation path. The bottom models differ from those of both Caswell and Ingenito, being based on the work noted in the previous paragraph. The first layer velocity for Leg C (1640 m/sec) is substantiated by an in-situ velocity measurement made near Stage I. The thickness of this layer is that used by Caswell and is based on seismic-refraction analysis. This layer thickness appears reasonable based on the length of the cores which yielded the velocity (2 to 4 m). In addition, Houston noted a layer thickness of 15 m for a layer of comparable velocity at a distance of 33 km along a 252° bearing from the stage. The second velocity (1850 m/sec) is an

TABLE 24

## ENVIRONMENTAL MODELS--LEGS C AND D

## Panama City

<u>Leg C</u>			<u>Leg D</u>		
<u>Depth</u> <u>(m)</u>	<u>Sound</u> <u>Velocity</u> <u>(m/sec)</u>	<u>Density</u>	<u>Depth</u> <u>(m)</u>	<u>Sound</u> <u>Velocity</u> <u>(m/sec)</u>	<u>Density</u>
0	1527.5		0	1527.0	
1.1	1526.0	1.0	4.1	1526.3	1.0
30.5	1525.0		10.5	1526.2	
			18.3	1525.2	
- - - Water/Bottom Interface - - -					
30.5	1640.0		18.3	1640.0	
34.3	1640.0	2.0	22.1	1640.0	2.0
34.3	1850.0		22.1	1850.0	
$\infty$	1850.0		$\infty$	1850.0	



average of those along the reflection leg (Figure 28) as determined by Houston.

The recent studies noted above covered an area seaward from Stage I. Hence, these findings must be extrapolated inshore to establish a bottom model for the region near Stage II and along Leg D. Ludwick (1964) studied the sediments in the northeastern Gulf of Mexico and classified the sediment, for a large region which included Panama City, as quartz sand of thickness less than 15 m. He noted the seaward distribution of this sand alternated between fine and medium sand out to a depth of about 20 fathoms. Calculations based on the grain-size distribution of Ludwick for sands in this region yielded a mean grain-size of 2.5 phi and a standard deviation of 0.51 phi. Gould and Stewart (1955) also studied the sediments off Northern Florida and arrived at basically the same conclusion; that is, that the sediments are quartz sands with no progressive change in particle-size distribution with increasing distance from shore. On this basis, it was concluded that the bottom model for Leg D should not differ substantially from that of Leg C. Thus, the same basic bottom model (see Table 24) was used for both sites.

6.3.3 Experimental bottom absorption. With bottom models established for Legs C and D, it is now possible to calculate energy ratios ( $\gamma$ ) using the three-layer normal-mode model, and hence, the experimental bottom absorption ( $\alpha_A$ ). These calculated values are listed in Table 25 for both legs using the mode-attenuation coefficients from Table 22 measured by Caswell. If the mode-attenuation coefficients of Ingenito are used and the bottom absorption is calculated with

TABLE 25

ENERGY DISTRIBUTION ( $\gamma$ ) AND BOTTOM-ABSORPTION COEFFICIENT ( $\alpha_A$ )--LEGS C AND D

Panama City

Frequency (Hz)	Leg C			Leg D		
	$\gamma^{(1)}$	$\gamma^{(2)}$	$\gamma$	$\gamma^{(1)}$	$\gamma^{(2)}$	$\gamma$
						$\alpha_A$ (dB/km)
50	0.05347	0.04663	0.10010	18.0	---	---
100	0.02636	0.00627	0.03263	37.4	0.06699	0.01879
200	0.00941	0.00045	0.00985	102.5	0.02796	0.00146
400	0.00233	$9.05 \times 10^{-6}$	0.00234	363.3	0.00769	$3.18 \times 10^{-5}$
600	0.00096	$3.63 \times 10^{-7}$	0.00096	945.0	0.00307	$1.23 \times 10^{-6}$
750	0.00061	$4.11 \times 10^{-8}$	0.00061	2088.1	0.00183	$1.29 \times 10^{-7}$
						0.00183
						919.5

4

the energy ratios from Table 25, bottom-absorption values of 260.7 dB/km at 400 Hz and 489.4 dB/km at 750 Hz are obtained.

6.3.4 Predicted bottom absorption. As noted previously, the sediments in the vicinity of Stage I have been described in some detail by Addy et al. (1979), and McMillan et al. (1978). Both studies are based on piston cores obtained along sample lines emanating from Stage I. Within 8 km of Stage I, four cores were obtained with lengths ranging from 2 to 4 m. The sediments within the cores were generally classified by McMillan as quartz-shell sands having mean grain-sizes ranging from 1.35 to 1.85 phi, with an average of 1.64. The sorting of this type of sand ranged from a standard deviation of 0.53 to 0.80 phi and the calcium carbonate content averaged approximately 18 percent. Addy estimated the mean grain-size for a larger area as 2.3 phi with a standard deviation of 1.0 phi. Using the grain-size values of McMillan, the Biot sediment model was used to predict the bottom absorption for frequencies from 50 to 750 Hz. The grain-sizes, other bottom parameters, and predicted absorption values are listed in Table 26 (a) and (b). Since some evidence exists for finer grain sizes in the test area, a mean grain-size of 1.85 phi [from Table 26 (a)] was used as being typical for the area.

#### 6.4 Discussion of Results

Mode-attenuation data from papers by Caswell and Ingenito were used for this test area to obtain experimental bottom-absorption data. Recent studies of the sediments off Panama City indicated that the bottom models assumed by both researchers might be improved. Based on these studies, a new bottom model was derived for both Legs C and D,

TABLE 26 (a)  
BIOT SEDIMENT MODEL PARAMETERS

## Panama City

Sample No.	Bottom Parameters					
	$M_z$ (phi)	$\sigma_\phi$ (phi)	$K$ (cm <sup>2</sup> )	$a$ (cm)	$\beta$	$\rho$ (g/cm <sup>3</sup> )
1	1.35	0.80	$4.1 \times 10^{-7}$	$2.5 \times 10^{-3}$	0.375	2.07
2	1.64	0.62	$3.5 \times 10^{-7}$	$2.3 \times 10^{-3}$	0.400	2.03
3	1.85	0.53	$2.9 \times 10^{-7}$	$2.1 \times 10^{-3}$	0.410	2.01

Note:  $k_r = 4.2 \times 10^{11}$  dyne/cm<sup>2</sup>       $\eta = 1.0 \times 10^{-2}$  dyne-sec/cm<sup>2</sup>  
 $k_f = 2.4 \times 10^{10}$  dyne/cm<sup>2</sup>       $v_E = 3 \times 10^4$  cm/sec       $\Delta_E = 0.15$   
 $\rho_r = 2.71$  g/cm<sup>3</sup>       $v_s = 2.1 \times 10^4$  cm/sec       $\Delta_s = 0.20$   
 $\rho_f = 1.00$  g/cm<sup>3</sup>       $\alpha = 1.25$

TABLE 26 (b)  
PREDICTED BOTTOM ABSORPTION ( $\alpha_A$ )

## Panama City

Sample No.	Absorption (dB/km)					
	50 Hz	100 Hz	200 Hz	400 Hz	600 Hz	750 Hz
1	6.1	22.4	83.5	294.6	563.6	768.1
2	5.2	18.6	69.5	252.6	507.2	717.8
3	4.4	15.7	58.2	214.8	444.0	644.4

and the experimental bottom absorption was then calculated for frequencies from 50 to 750 Hz. The most sensitive parameter in the bottom model was determined to be the velocity of the first bottom layer. For example, as this parameter was varied from 1620 to 1711 m/sec, the absorption ( $\alpha_A$ ) varied from  $0.022 f^{1.63}$  to  $0.007 f^{1.94}$  dB/km ( $f$  in Hz). On the other hand, as the first layer thickness varied from 3.8 to 10 m, the absorption ( $\alpha_A$ ) varied from  $0.015 f^{1.73}$  to  $0.0065 f^{1.86}$  dB/km. The bottom model chosen for Legs C and D (Table 24) used a sound speed of 1640 m/sec determined from in-situ velocity measurements on cores near Stage I. Using this bottom model and the mode-attenuation coefficients of Caswell and Ingenito, the bottom absorption was calculated. From analysis of these same cores, mean grain-size data were obtained and used in the sediment models of Biot and Hamilton to predict bottom absorption.

The experimental and predicted bottom-absorption data is plotted in Figure 29 and listed in Table 27 in the power law form  $\alpha_A = K_A f^n$ . Also listed in Table 27 is the original data of Caswell and Ingenito. In the figure, the Hamilton model matches the experimental absorption reasonably well at low frequencies, whereas the Biot model does not predict enough absorption. At the higher frequencies (600 to 750 Hz), neither model predicts enough absorption when compared with the results obtained from Caswell's mode-attenuation data. When the predicted values are compared with the experimental values based on Ingenito's measurements, the agreement is better. Because of this inconsistency, the 750 Hz data points have been deleted in the power-law calculations in Table 27. In general, the Biot model shows slightly better agreement with the data over the frequency range than does Hamilton's model,

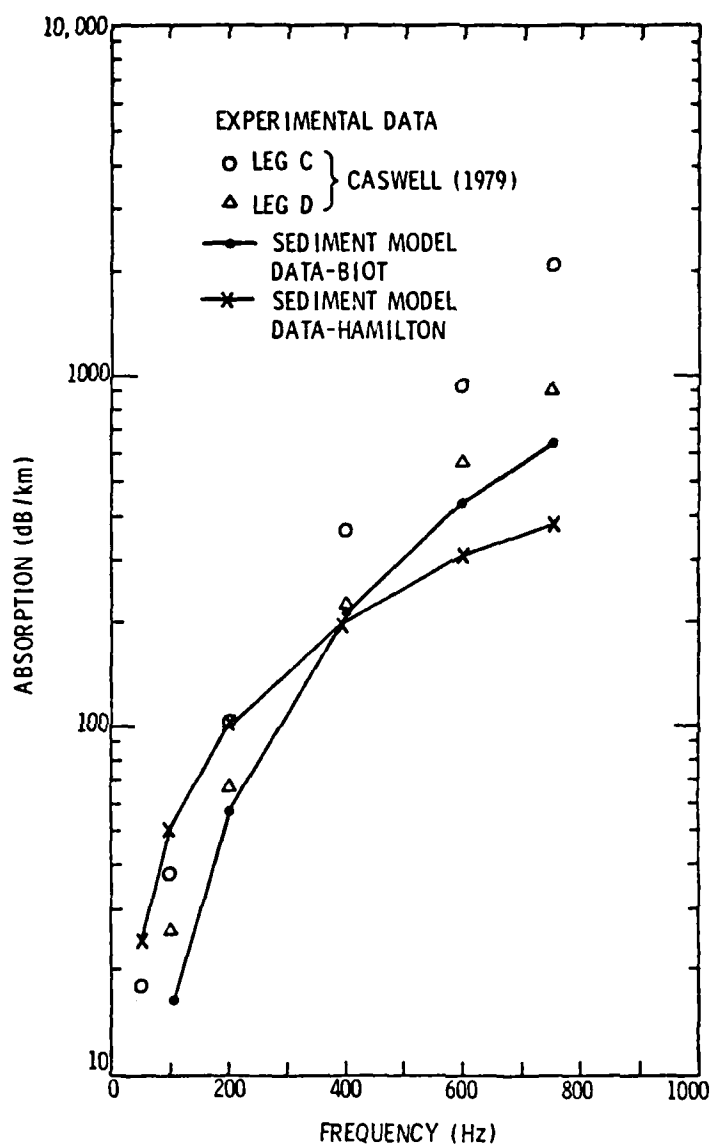


Figure 29. Comparison of Experimental and Predicted Bottom Absorption--Panama City

TABLE 27

POWER-LAW FITS TO BOTTOM-ABSORPTION COEFFICIENTS ( $\alpha_A$ )

## Panama City

<u>Leg</u>	Experimental $\alpha_A$ (dB/km)	Predicted $\alpha_A$ (dB/km)	
		<u>Biot</u>	<u>Hamilton</u>
C	0.0177 $f^{1.81}$ (Caswell, 1979)	0.003 $f^{1.86}$	0.501 $f^{1.0}$
	0.0028 $f^{1.75}$ (Ingenito, 1973)		
	0.0290 $f^{1.59}$		
D	0.0015 $f^{2.08}$ (Caswell, 1979)	0.003 $f^{1.86}$	0.501 $f^{1.0}$
	0.0090 $f^{1.71}$		

---

Note:  $f$  is in Hz.

---

although the agreement is not as good as that obtained at other sites. As may be seen in Table 27, the frequency dependence for all the data (except the predictions of Hamilton) is closer to  $f^2$  than  $f^1$ . The difference in bottom models has a relatively small effect on the value of  $K_A$  and  $n$  as may be seen by comparing Caswell's original Leg C data and the experimental absorption data for Leg C derived here.



## CHAPTER VII

### PREDICTION OF TRANSMISSION LOSS

#### SCOTIAN SHELF EXPERIMENTS

##### 7.1 Introduction

The ultimate test of a sediment model is how well transmission loss is predicted when the results of this model are used in the propagation model. Thus, in this chapter, bottom absorption-loss ( $\alpha_A$ ) is predicted based on the best available sediment data. The adiabatic normal-mode propagation model is then run using the bottom-absorption data to calculate the transmission loss. The Scotian Shelf site is interesting for this purpose, since a wide variety of sediment types and bottom structures is present. In addition, excellent sediment data and advice as to its interpretation were provided by the Bedford Institute of Oceanography of Dartmouth, Nova Scotia.

The procedure followed is similar to previous chapters in that the experiment and the calculation of experimental transmission loss are described first. The prediction of transmission loss is discussed next, wherein the construction of a geoacoustic model for the water-seabed system is described. Finally, the experimental and predicted loss data are discussed and then compared.

##### 7.2 Experiments

During September of 1978, experiments were performed at two sites off the coast of Nova Scotia. Long-range and short-range propagation and seismic-refraction experiments were performed at

both sites; however, only the long-range experiment at one site will be discussed here. Prior to the September experiment, sub-bottom profiling was performed along the propagation track using the Huntec Deep-Tow System. The data obtained from this system and grab-sample data obtained from the Bedford Institute of Oceanography of Dartmouth, Nova Scotia, provided useful information describing the seabed in the test area.

At the test site, the new array was moored in water 57 m deep. The long-range propagation track covered a sloping bottom with the water depth reaching approximately 265 m near the maximum range of 125 km. Large (456 g) charges were dropped at nominal depths of 38 and 79 m at range intervals of 1.6 km. The array covered approximately the bottom half of the water column at this site. The bathymetry and sound-velocity profiles obtained along the propagation track are depicted in Figure 30. The source depths are indicated by the dotted lines in the figure.

### 7.3 Calculation of Experimental Transmission Loss

Signals received on the bottom hydrophone of the array (1 m above the bottom) were analyzed as discussed in Chapter III to determine their energy content in one-third-octave bands centered at frequencies from 25 to 800 Hz. Source spectrum levels for the 456 g shots were established by R. C. Hughes, Defense Research Establishment Atlantic, Dartmouth, Nova Scotia, using a modification of the Gaspin and Shuler (1971) technique [see Hughes (1976)] to obtain improved results below the bubble frequency. Hughes verified the predicted source levels for the 79 m depth by comparing them with actual recorded levels for a similar charge detonated at a depth of 77 m. The transmission loss

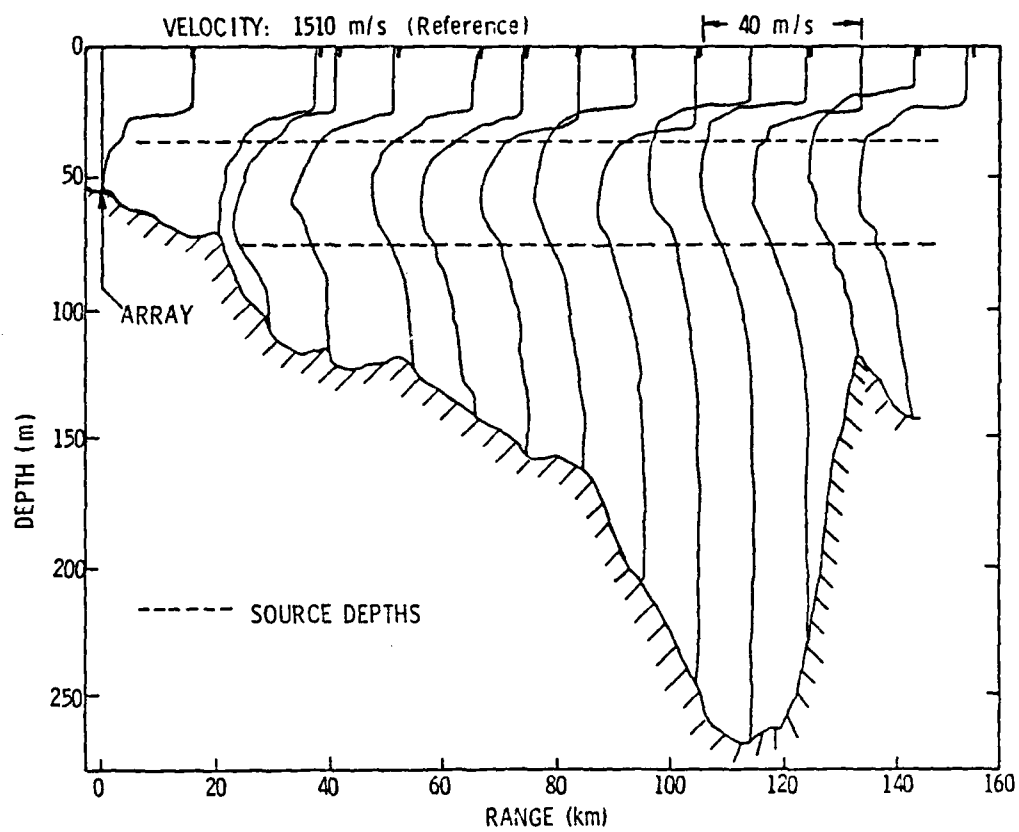


Figure 30. Depth and Sound Velocity Profiles--Scotian Shelf

was calculated by taking the difference between the received energy level and the source spectrum level in the desired one-third-octave band and at the source-receiver range of interest. The range separation was calculated (see Chapter III) using the shot instant time (recorded on the shot boat) and the receive time to obtain the travel time; the range was calculated by multiplying the travel time by the sound speed in water.

The experimental transmission loss measurements for the test site will be discussed later when comparisons with the predicted losses are made.

#### 7.4 Calculation of Predicted Transmission Loss

7.4.1 Range-dependent model. Because of the sloping bottom found at the site, the standard normal-mode propagation model does not apply. As discussed in Chapter II, a modification to this model, the adiabatic normal-mode model, may be used for bottoms having a moderate slope. This model assumes that each normal mode propagates independently with no exchange of energy between modes (i.e., no mode coupling.) McDaniel (1977) has shown that mode coupling, which may be due to surface or bottom roughness, inhomogeneities within the water column, or severe bottom slopes, increases with frequency. Hence, the model will have definite high-frequency limitations.

The adiabatic normal-mode model is implemented by assuming that the propagation track may be divided into segments for which the standard normal-mode theory applies. The mode excitation may be found at the source and receive positions for each segment and then, knowing the mode attenuation along the segment, the transmission loss may be calculated. To calculate mode attenuation, estimates of the attenuation

due to scattering, conversion to shear, and bottom absorption must be obtained. The prediction calculation is thus the reverse of that employed in Chapters IV - VI. For example, bottom absorption will be predicted and the mode-attenuation coefficient calculated from the product of the bottom-absorption coefficient and the energy ratio. Thus, both the water column and ocean bottom must be well characterized (i.e., a geoacoustic model for the environment) to use the adiabatic normal-mode model.

7.4.2 Geoacoustic model. This model is a complete environmental model for the water-bottom system in the sense that all the parameters relating to acoustic propagation are specified. These parameters include the sound speed in the water and its variation with depth, the compressional and shear velocity, the density, and the absorption coefficients for compressional and shear waves as a function of depth in the bottom. As noted previously, the bottom is assumed to consist of discrete layers so that the layer thickness and the other parameters must be specified for each bottom layer.

Because of the Huntec profiling and the grab-sample data available for the Scotian Shelf, the formulation of a well-documented geoacoustic model was possible. In addition, seismic-refraction and dispersion analysis provided confirmation (and, in some cases, the only data) for the chosen model.

The Huntec system consists of an electrodynamic source towed at mid-depth and the associated shipboard signal processing equipment. It has been shown by Parrott et al. (1979) that the system provides a reliable indication of surficial sediment type due to a statistical analysis of the energy returned from the bottom. The presence and

identity of deeper (up to 50 m or so) sub-bottom reflectors is readily apparent on the system output. In many cases, surficial, intermediate, and bedrock layers were identified from the records. Where grab-samples were available near the propagation track, the mean grain-size obtained from this data was used in the sediment models to predict bottom absorption. In other cases, the Hunttec records were used as an indication of sediment mean grain-size. The findings of King (1970) provided supporting data on the sediment types at the site.

Sound speeds were established using a regression equation derived by Anderson (1974) which used mean grain-size as the independent variable. The velocity  $c$ (m/sec) at a temperature of 20°C and a pressure of one atmosphere was calculated from the expression:

$$c = -68.156 M_z + 3.053 M_z^2 + 1874.4$$

These velocities were then corrected to the bottom temperature and depth.

The intermediate layers were identified by the appearance of the fine structure on the Hunttec records. A mean grain-size was assigned based on this identification and the absorption was calculated using the sediment models. The work of Hamilton (1975) was followed in determining a depth correction for the calculated absorption values.

In those cases where the bedrock layer could not be identified from the Hunttec record, estimates of the depth to this layer and the probable type were obtained from King and MacLean (1976). Tertiary and cretaceous formations were identified as the bedrock structure along the track. King estimated that compressional sound speeds of

2000 to 2300 m/sec would exist for these structures; hence, the bedrock is classified as more of a semi-consolidated sediment.

Based on the preceding considerations, the bottom structure at the site was modeled as shown in Figure 31. For use in the adiabatic normal-mode model, the bottom in the figure was broken down into the segments identified, by range from the array, in Table 28. At the site and along the track, sediment identification was based on grab-sample data as noted in the table. Beneath the array, the sediments consisted of gravel and sand. Because the regression equation for calculating the velocities does not apply to such coarse sediments, seismic-refraction and dispersion analyses were used to establish the first layer velocity for the zero and 11 km segments. The 19 km segment consisted of slightly finer sediments; hence, the velocity was reduced slightly from that of the previous segments. The portion of the track from 27 through 95 km was modeled using velocities and absorption coefficients predicted by the regression equation and the Biot sediment model using mean grain-size data. At the opposite end of the track (117 km), the Hunttec records showed that the bottom consisted of a thin clay layer over a pocket of silt and diffused gas. A mean grain-size was assumed from the Hunttec data for the clay. The absorption and velocity for the gassy silt were obtained by modifying the fluid parameters in the Biot model according to an assumed concentration of methane gas in seawater. With this approach, the pore fluid was assumed to be a suspension of small methane bubbles in seawater so that the equation of Wood (1944) applied.

That is, the density and compressibility of the mixture were obtained from the volume fraction of methane and seawater present.

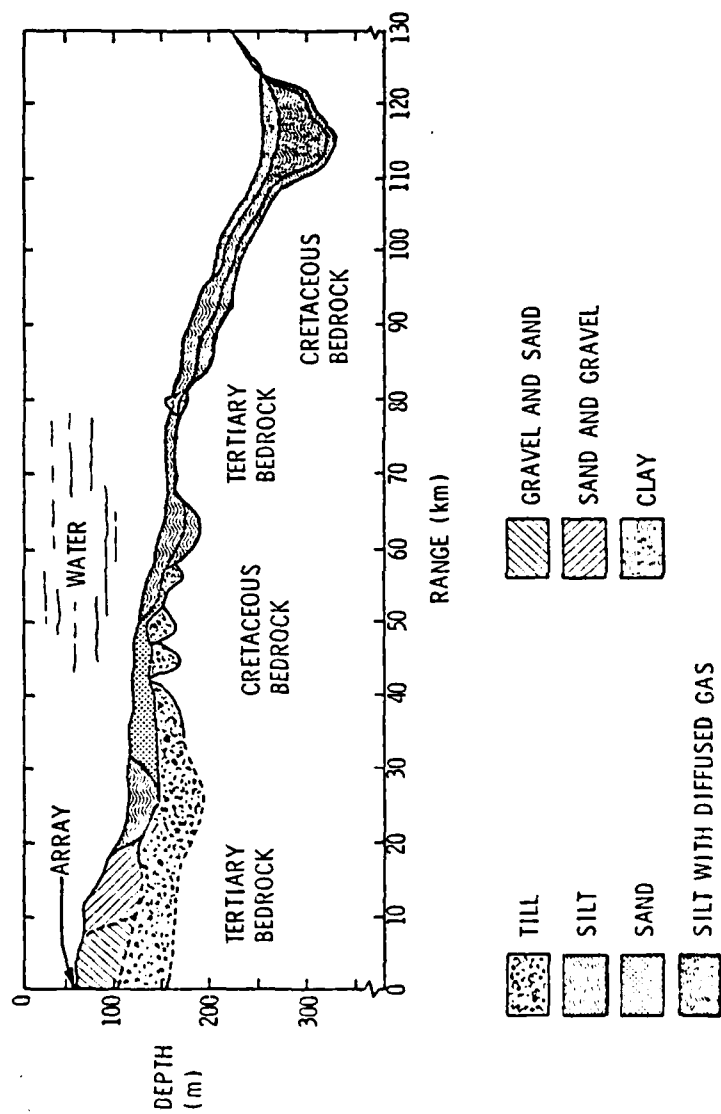


Figure 31. Bottom Structure--Scotian Shelf



TABLE 28  
SEABED PARAMETERS - SCOTIAN SHELF

Range (km)	Water Depth (m)	Layer	$M_z$ (phi)	$\sigma_\phi$ (phi)	Thickness (m)	Velocity (m/sec)	Density (g/cm <sup>3</sup> )	$K_A$ (dB/km · Hz)	n
0	57	1	0.5	1.0	3	1850	2.06	0.0300	1.57
		2	1.2	0.6	47	1900	2.00	0.0113	1.72
		3	1.0	1.5	50	1950	2.10	0.0034	1.83
		4			$\infty$	2000	2.20	0.0500	1.00
11	67				SAME AS ABOVE				
19	76	1	0.5	1.0	3	1800	2.06	0.0300	1.57
		2	1.2	0.6	47	1850	2.06	0.0113	1.72
		3	1.0	1.5	30	1950	2.10	0.0034	1.83
		4			$\infty$	2000	2.20	0.0500	1.00
27	106	1	6.3	2.7	30	1600	1.56	0.0560	1.01
		2	1.0	4.0	50	1900	2.00	0.0065	1.30
		3			$\infty$	C 2300 S 1200	2.30	0.0090	1.00
33	118				SAME AS ABOVE				
45	126	1	3.0	1.7	28	1650	1.96	0.0370	1.14
		2	1.0	4.0	24	1900	2.10	0.0065	1.30
		3			$\infty$	C 2300 S 1200	2.30	0.0090	1.00
58	137	1	7.0	2.3	13	1513	1.45	0.0570	1.00
		2	1.0	4.0	21	1850	2.10	0.0065	1.30
		3			$\infty$	C 2000 S 900	2.20	0.0500	1.00

TABLE 28 (continued)

Range (km)	Water Depth (m)	Layer	$M_z$ (phi)	$\sigma_\phi$ (phi)	Thickness (m)	Velocity (m/sec)	Density $\rho$ (g/cm <sup>3</sup> )	$K_A$ (dB/km · Hz)	n
67	150	1	5.8	1.7	25	1550	1.58	0.0570	1.00
		2			10	1850	2.10	0.1020	1.00
		3			$\infty$	C 2000 S 900	2.20	0.0500	1.00
79	161	1	4.2	1.7	10	1580	1.56	0.0560	1.01
		2			$\infty$	C 2000 S 900	2.20	0.0500	1.00
95	214	1	4.2	1.7	18	1580	1.56	0.0560	1.01
		2			6	1800	2.10	0.0870	1.01
		3			$\infty$	C 2000 S 900	2.20	0.0500	1.00
117	265	1	8.0*	2.0*	7	1510	1.41	0.0560	1.00
		2			10	**	1.68	**	1.01
		3			6	1850	2.10	0.0870	1.01
		4			$\infty$	C 2300 S 1200	2.30	0.0090	1.00
125	236	1	3.0*	1.0*	10	1580	1.54	0.0200	1.02
		2			40	1640	1.72	0.1120	1.00
		3			6	1850	2.10	0.0870	1.01
		4			$\infty$	C 2300 S 1200	2.30	0.0090	1.00

\*  $M_z$  deduced from Hunttec Reflectivities;  $\sigma_\phi$  assumed.

\*\* Values were obtained from Table 29 for 0.1 and 0.01% concentrations of methane.

Thus, if  $V_m$  is the fraction of methane present, the density ( $\rho_{mw}$ ), bulk modulus ( $k_{mw}$ ), and sound velocity are obtained as follows:

$$\rho_{mw} = V_m \rho_m + (1 - V_m) \rho_w ,$$

$$k_{mw} = \frac{k_m k_w}{V_m k_w + (1 - V_m) k_m}$$

and

$$c_{mw} = \sqrt{\frac{k_{mw}}{\rho_{mw}}} ,$$

where the subscripts  $m$  and  $w$  indicate quantities of methane and water, respectively. The effect of changing the fraction of methane in the mixture may be seen in Table 29. The values for  $K_A$ ,  $n$  and  $C$  were obtained by using  $\rho_{mw}$  and  $k_{mw}$  as the fluid density and bulk modulus in the Biot sediment model. As will be discussed later, adiabatic normal-mode runs were made using the Biot model parameters from Table 29 for concentrations of 0.1 and 0.01 percent methane within the segment at 117 km.

#### 7.5 Comparison of Measured and Predicted Transmission Loss

The experimental and predicted transmission loss data are plotted in Figures 32 (38 m source depth) and 33 (79 m source depth) for frequencies of 25, 80, 250, and 800 Hz. The discussion to follow begins with a paragraph relating the experimental data to environmental conditions; the predicted loss is discussed next in terms of the geoacoustic model, and finally, possible reasons for agreement and disagreement between the measured and predicted loss are considered.

TABLE 29  
EFFECT OF METHANE CONCENTRATION

% Methane	$\rho_{nw}$ (g/cm <sup>3</sup> )	$k_{nw}$ (dyne/cm <sup>2</sup> )	$c_{mw}$ (m/sec)	Biot Model Predictions		
				K <sub>A</sub>	n	C (m/sec)
10.00	0.923	$1.32 \times 10^8$	119.5	11.70	1.00	266.8
5.00	0.974	$2.62 \times 10^8$	164.1	9.10	1.00	289.7
1.00	1.015	$1.26 \times 10^9$	351.9	2.86	1.00	426.3
0.50	1.020	$2.39 \times 10^9$	483.9	1.39	1.00	540.8
0.10	1.024	$8.54 \times 10^9$	913.2	0.26	1.01	942.1
0.05	1.024	$1.26 \times 10^{10}$	1108.9	0.15	1.01	1128.6
0.01	1.025	$2.03 \times 10^{10}$	1408.1	0.07	1.01	1411.3

Note: In calculating the quantities in this table, the following values were assumed:

$$\rho_w = 1.025, \quad \rho_m = 0.007168 \text{ g/cm}^3$$

$$k_w = 2.4 \times 10^{10} \text{ and } k_m = 0.001325 \times 10^{10} \text{ dyne/cm}^2$$

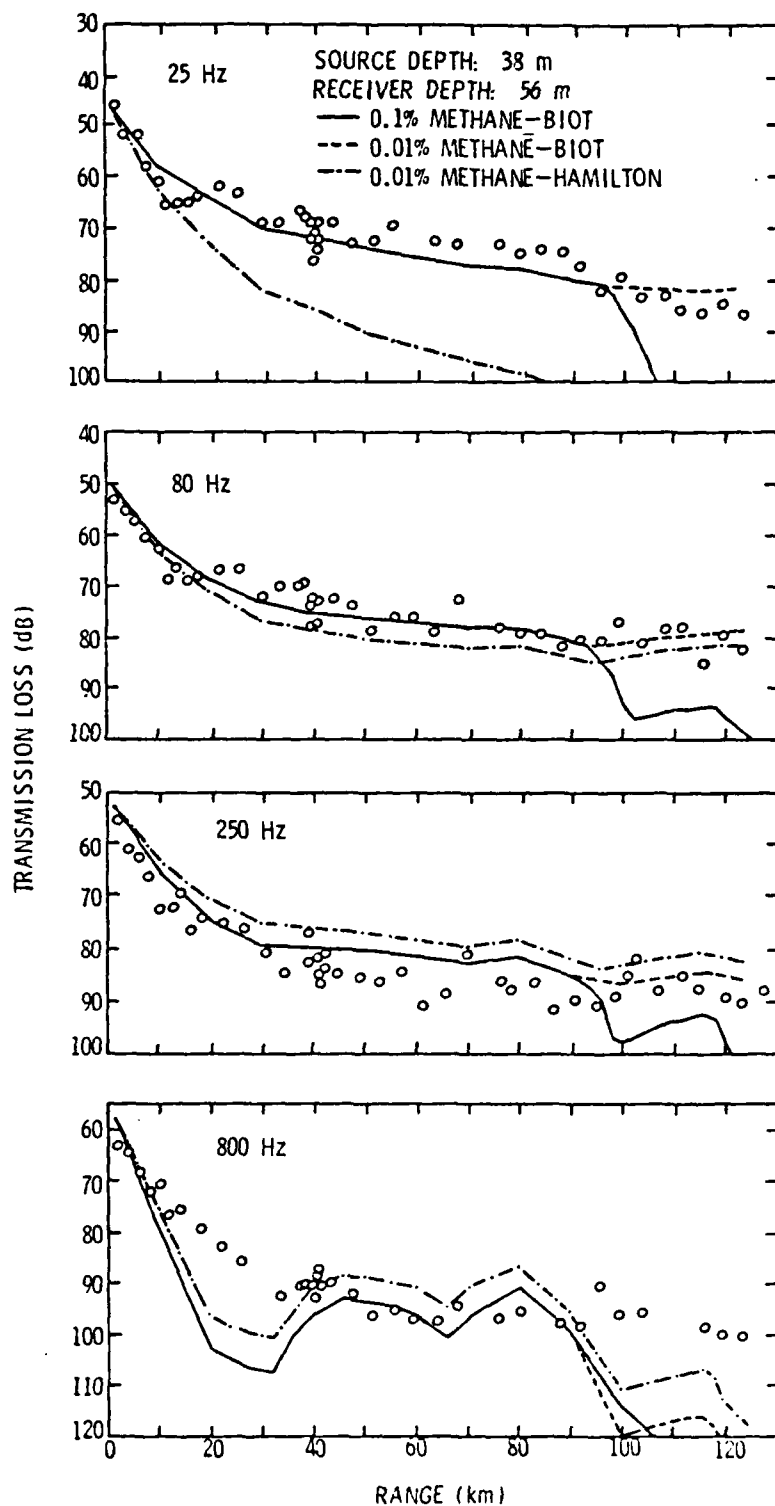


Figure 32. Comparison of Experimental and Predicted Transmission Loss--Scotian Shelf, 38 m Depth

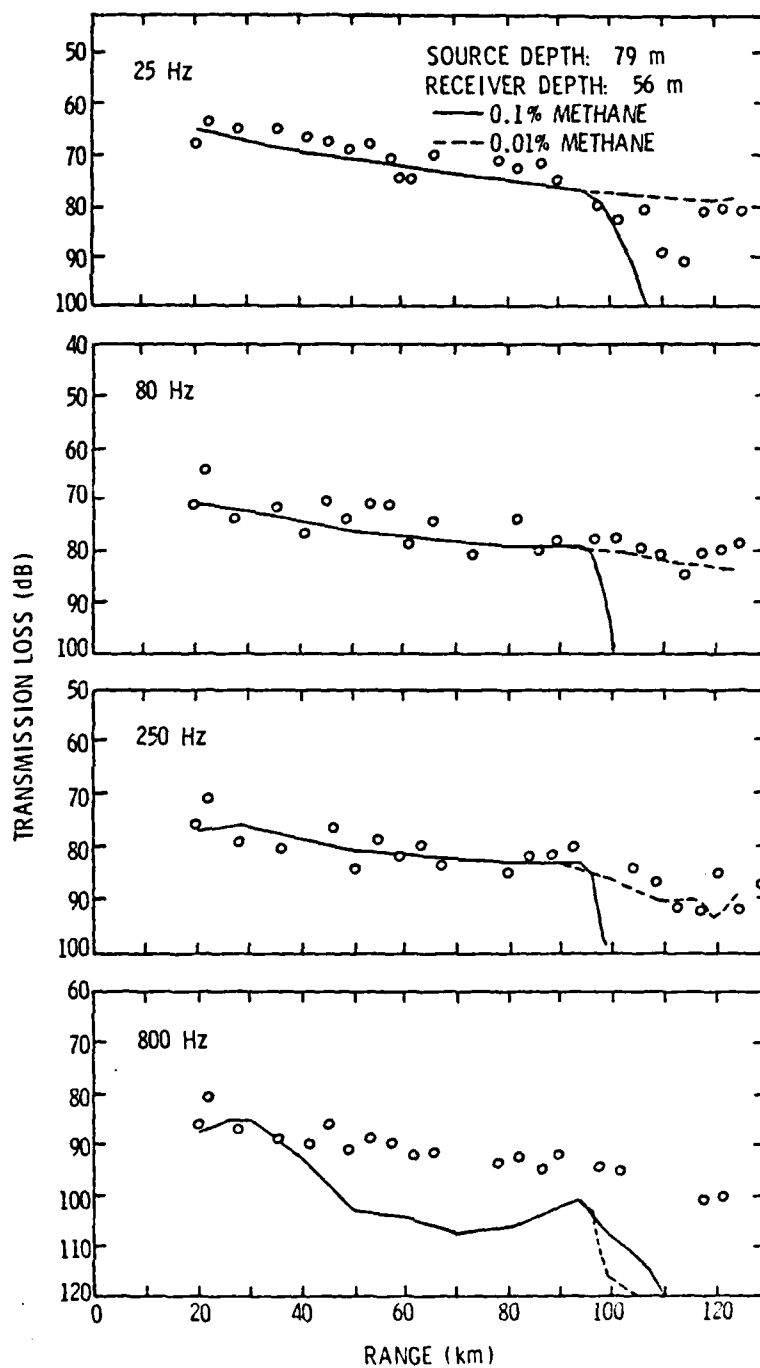


Figure 33. Comparison of Experimental and Predicted Transmission Loss-Scotian Shelf, 79 m Depth

7.5.1 Experimental transmission loss. Propagation at the Scotian Shelf site was largely controlled by the sound-velocity profiles which existed there. The loss measured for the shallow source (Figure 32) reflects this best, as charges were dropped over all but the first 2 km of the track. In Figure 30, it can be seen that out to a range of 20 km, the shot is detonated in a region where, due to the decrease of sound velocity with depth (a negative profile), the sound rays will be refracted into the bottom. This resulted in bottom-dominated propagation in this region and accounted for the large increase in loss as the range increased.

Beyond 20 km, the sound-velocity profiles in Figure 30 indicate the presence of a sound-velocity minimum. This type of profile will cause the energy, for a source detonated near the axis of the minimum, to be channeled with little interaction with the surface or bottom. Losses in the channel are expected to be near cylindrical spreading in magnitude. The losses were, in fact, near cylindrical spreading for 25 and 80 Hz beyond 20 km, as both source depths were near the channel axis (note the dotted lines in Figure 30). A last point of interest is near 117 km where the pocket of silt with diffuse gas is indicated in Figure 31. An increase in loss is shown in Figure 32 in this same region, particularly at 25 Hz, and in Figure 33 for all frequencies to some extent. In general, the loss appeared to increase, for both source depths, as the frequency increased from 25 to 800 Hz.

7.5.2 Predicted transmission loss. Using the sound-velocity profiles from Figure 30 along with the seabed parameters of Table 28, the adiabatic normal-mode computations of transmission loss were

performed. As noted in the table, the bottom is specified by 12 segments. Over the first 20 km of the propagation track in Figure 32, the bottom is well characterized by the first three segments, and high losses are predicted for the coarse sediments in this region. In the region between 20 and 95 km, the finer silt and sand sediments modeled in Table 28 cause the rate of loss to be somewhat reduced from that encountered over the early portion of the track. The erratic behavior shown at 800 Hz reflects the extreme sensitivity to changing environmental parameters encountered as the frequency increases. The segment at 117 km reflects profoundly the effect of the silt-gas sediments. Methane concentrations of 0.1 and 0.01 percent are used since the true concentration is unknown. The effect of this gas is to reduce the sound velocity and increase the attenuation within the sediment. Because the adiabatic model uses interpolation between segments, the effects of the gassy sediment are indicated by increased transmission loss from 95 km to the end of the track. The main cause of the increased loss is the low sound velocity. A low-velocity layer is formed, as in the Corpus Christi discussion, which traps energy in the layer and reduces the pressure field in the water column.

The transmission loss predicted using the Hamilton method for sediment absorption is also shown in Figure 32.

7.5.3 Comparison. In both figures, the agreement is excellent for frequencies of 25, 80, and 250 Hz. At 25 Hz, the propagation model (Biot sediment model) accurately predicts the rapid increase in loss occurring at ranges less than 20 km. As discussed earlier, the bottom absorption dominates this loss since most of the energy is refracted



into the bottom. The reduced loss, occurring at ranges greater than 20 km due to the sound channel, is also predicted with reasonable accuracy out to a range of 90 km or so. At this range, the experimental transmission loss tends to increase somewhat due to the basin where the gassy sediments are found. The loss predicted for the two assumed methane concentrations appears to bracket the observed variation in transmission loss. That is, a reduction of the second bottom layer sound velocity to 942 m/sec (0.1 percent concentration) in the model causes an excess of energy to be trapped in the layer. The higher velocity (1411 m/sec) for the 0.01 percent concentration has very little effect. Possibly, an intermediate concentration or a more detailed model (in range segments) would give better results.

The loss predicted at 80 Hz gives excellent agreement over all of the track if the methane concentration is correctly assumed to be 0.01 percent. The experimental data shows little of the effects (for either source depth) at 117 km that were noted at 25 Hz, so the methane could be ignored with probably the same result.

As the frequency increases to 250 Hz, the rapid increase in loss over the first 20 km of the track is still predicted. At ranges greater than 20 km, the agreement for the shallow source is not quite as good as for the deep source. In the region around 117 km, agreement is still good for both source depths, assuming a 0.01 percent concentration. The shallow source and the reduced bottom penetration (due to the higher frequency) appear to result in less trapping of energy in the low-velocity layer for the 0.1 percent concentration. The deep source still predicts losses in excess of 100 dB in the gassy region for the same concentration.

The predicted losses at 800 Hz are in poor agreement with the measured data. While the frequency dependence of the bottom absorption appears to be satisfactory over the lower frequencies, an excess of attenuation is predicted at 800 Hz. The only region with good agreement is the section between 40 and 90 km for the shallow source. Extreme effects are noted beyond 90 km for both concentrations. Since this behavior is not consistent with the low frequency performance, something other than the bottom model is assumed responsible. It appears that these predicted variations are due to the changing temperature structure shown in Figure 30, and particularly, the depth of the isovelocity layer. In addition, at this frequency, mode coupling can no longer be ignored and its inclusion in the model will have some effect (although unknown at this time). Thus, the data at 800 Hz does not represent a valid test of our ability to predict bottom absorption as the propagation model itself is not adequate at these frequencies and water depths.

In Figure 32, transmission loss is also predicted using Hamilton's method for calculating sediment absorption. The mean grain-sizes in Table 28 were used in Hamilton's equations to obtain  $\alpha_A$ , and these values were then used in the adiabatic normal-mode propagation model. At 117 km, the gassy silt was modeled with the Biot values (0.01 percent concentration) for absorption and velocity, although the upper clay layer was modeled using Hamilton's equation. As can be seen in Figure 32, the transmission loss predicted at 25 Hz is much greater than that measured for ranges beyond 15 km or so. At 80 Hz, the predictions are only 4 to 5 dB low, and at 250 Hz, the situation reverses with predictions somewhat less than that measured.

The loss predicted at 800 Hz parallels the Biot results but is 4 to 5 dB greater. Overall, the results using Hamilton's method give poorer agreement than those using Biot's theory.

## CHAPTER VIII

### SUMMARY AND CONCLUSIONS

The degree to which transmission loss may be accurately predicted is dependent upon both a detailed knowledge of the ocean environment and the use of propagation models which faithfully represent the physical processes at work. The purpose of this study has been to show that, given a comprehensive propagation model (the normal-mode model), transmission loss may be predicted using an environmental model whose bottom effects are predicated on two sediment models. As a test of the accuracy of the theories, experimental bottom absorption, calculated from mode-attenuation coefficients using a normal-mode model, has been compared with the absorption predicted by the Biot sediment model. This comparison was also performed for sediment absorption calculated using the procedures developed by Hamilton.

Values of bottom absorption obtained from experimental data acquired at several test sites were compared with the bottom absorption predicted by the Biot and Hamilton models. The experimental bottom absorption ( $\alpha_A$ ) was calculated through the relation  $\alpha_A = \delta/\gamma$ , where the mode-attenuation coefficient ( $\delta$ ) was obtained experimentally. The energy distribution ( $\gamma$ ) was obtained by calculations performed using the normal-mode program. The accuracy of this calculation for  $\alpha_A$  rested upon the validity of the bottom model developed to represent the test site. A key component of the discussion within these chapters was the variation of the experimental and predicted bottom absorption

with frequency. This frequency dependence constitutes one of the basic differences between the Biot and Hamilton predictions of sediment absorption.

The Scotian Shelf data were used for testing the transmission loss predictions using the range-dependent propagation model and the two sediment models. A wide variation in sediment type from gravel to clay was present along the propagation track and excellent data characterizing the seabed was available.

### 8.1 Discussion of Results

The calculation of experimental bottom absorption was based on mode-attenuation data, where sediment absorption was the dominant loss mechanism, and an environmental model which accurately represented the water-bottom system. The mode-attenuation data have been discussed in some detail in the relevant chapters, as have the environmental data. However, some additional discussion of the environment is appropriate. In addition, the sediment models and the parameters required to use them are discussed and compared.

8.1.1 Environmental effects. The calculated bottom absorption is dependent upon the environmental model through the energy distribution parameter  $\gamma$ . That is, any change in the sound-velocity profile within the water column or within the bottom will affect the mode amplitude distribution in the water and bottom and, hence, the energy distribution. These effects are frequency dependent in that the high frequencies are influenced much more than the low frequencies. For any sound velocity profile, most of the energy will be concentrated in the water column at high frequencies (750 Hz or greater). Of the

remaining energy (that in the bottom), 99 percent is found within the uppermost bottom layer. This is in contrast to the situation at low frequencies (50 Hz and less) where the energy in the uppermost layer may be only 40 percent or so of the total bottom energy. Because of this, a small change in the sound-velocity gradient (e.g., from a weak sound channel to a positive gradient) can cause a decrease in  $\gamma^{(1)}$  and, consequently, a significant increase (50 percent or so) in the absorption at high frequency; essentially none occurs at low frequency. As the sound waves propagate along a track where such changes occur, only net effects are observed. Hence, by choosing some mean profile, these effects can be modeled. The situation at Daytona Beach--Site 1 represents this type of problem, and by choosing a representative sound-velocity profile, the changing sound speed profile effects are minimized. In all the other test data, except the range-dependent case on the Scotian Shelf, a near-isovelocity sound speed profile was present.

The bottom parameters affecting the experimental bottom absorption are, for the three-layer model, the velocity ( $c_1$ ) and thickness ( $H_1$ ) of the first bottom layer, and the velocity ( $c_2$ ) of the second bottom layer. The effect of certain of these parameters has been noted with regard to the Panama City data. The general behavior of these parameters may be inferred through a more detailed analysis of the Panama City--Leg C bottom absorption data. The bottom model used for this site is listed (model number 4) in Table 30 (a) along with four other possible bottom models and the consequent bottom absorption ( $\alpha_A$ ) for frequencies of 50, 400, and 750 Hz. Sensitivity parameters  $SC_1$ ,  $SH_1$ , and  $SC_2$  are calculated

TABLE 30 (a)  
BOTTOM PARAMETERS FOR SENSITIVITY STUDY  
Panama City Leg C

Model No.	$C_1$ (m/sec)	$H_1$ (m)	$C_2$ (m/sec)	$\alpha_A$ (dB/km)			$K_A$	n
				50 Hz	400 Hz	750 Hz		
1	1620	3.8	2100	23.7	295.1	1618.2	0.0436	1.52
2	1711	3.8	1850	19.4	648.9	3950.6	0.0070	1.94
3	1620	3.8	1850	17.6	290.9	1616.2	0.0215	1.63
4	1640	3.8	1850	18.0	363.3	2088.1	0.0152	1.73
5	1640	10.0	1850	13.7	352.0	2035.7	0.0065	1.86

TABLE 30 (b)  
SENSITIVITY TO BOTTOM PARAMETERS  
Panama City Leg C

Sensitivity Measure	Definition	Comparison Models	Sensitivity		
			50 Hz	400 Hz	750 Hz
$SC_1$	$\Delta\alpha_A / \% C_1$	2 - 3	0.34	67.31	440.45
$SH_1$	$\Delta\alpha_A / \% H_1$	4 - 5	-0.07	-0.18	-0.04
$SC_2$	$\Delta\alpha_A / \% C_2$	1 - 3	0.51	0.35	0.17

Note:  $\% C_1 = 5.3$ ,  $\% H_1 = 62.0$ ,  $\% C_2 = 11.9$ .

in Table 30 (b) by dividing the change in  $\alpha_A$  by the percentage change in the parameter of interest, the other parameters remaining constant. The two models involved for each comparison (e.g., two and three for  $SC_1$ ) and the resulting sensitivity to the three parameters at each frequency are noted. As can be seen, at 50 Hz, the absorption is somewhat more sensitive to  $c_2$  than the other parameters. At the mid-frequency (400 Hz) and the highest frequency (750 Hz), the absorption is extremely sensitive to  $c_1$ . An analysis of the sensitivity of  $K_A$  and  $n$  would show a similar relation (i.e., most sensitive to  $c_1$ ) as  $c_1$  has a large effect over a great proportion of the frequency range. The negative values for  $SH_1$  indicate that, as the layer thickness decreases, the absorption increases. The value selected for  $c_1$  in the bottom model for each site is based on the best available information; for the Daytona Beach and Corpus Christi sites,  $c_1$  was determined by dispersion analysis, and for the Panama City site,  $c_1$  was based on an in-situ measurement with the coring apparatus. This value will be most reliable for short-range measurements.

8.1.2 Predicted bottom absorption. The ability to predict bottom absorption is dependent upon the adequacy of the sediment data and the validity of the sediment model. However, even the best of sediment information will describe only the upper few meters of the ocean bottom and waves propagating at the lower frequencies will frequently penetrate much deeper than this.

The ideal type of sediment data consists of long cores, taken every kilometer or so along the shot tracks. This enables a complete



description of the sediments and their variation with range and depth to be made. As noted in the respective analysis chapters, this type of data was generally not available. Of the sites discussed, the short-range Corpus Christi site has the best sampling of cores; two cores were obtained near the site, and two more were spaced along the short-range track. In addition to the standard analysis of these cores, the sound velocity through the core was also measured. The combination of Hunttec profiling and ample grab-samples resulted in good sediment data for the Scotian Shelf site. The Panama City and Daytona Beach sediments were not characterized as well. Adequate coring data were available at the deeper site (31 m) off Panama City, but none was available along the track at the deep site nor for the shallow site and shot track. The shallow site (Site 1) off Daytona Beach was sampled with cores and grab-samples around the periphery of the short-range legs, while the deeper site was characterized by grab-samples at either end of the long-range shot track. In most cases, except for the Scotian Shelf, the sediment parameters assumed are most representative of the short-range propagation tracks. These parameters ( $M_z$  and  $\sigma_\phi$ ) are listed in the table of summary parameters, Table 31, along with other parameters to be discussed later.

While the best available data were used as inputs for the sediment models, all of the information desired was not available at every site. Thus, the validity of the sediment model is not so much a question of its credibility as a question of the validity of its input and peripheral calculations. Both sediment models have achieved credibility as discussed in Chapter II. Thus, the critical input parameters will be discussed and then certain effects embodied in the

TABLE 31

## DATA SUMMARY

Site	Sediments	Frequency Dependence						Fit of Prediction			
		Experimental $\alpha_A$			Predicted $\alpha_A$			$\chi^2$ Experimental Data			
		$M_z$	$\sigma_\phi$	$K_A$	n	$K_A$	n	Biot	Hamilton		
<u>Daytona Beach</u>											
Site 1:											
	Leg E	1.44	0.84	0.013	1.65	0.004	1.86	0.490	1.0	73.3	180.1
	Leg F	1.44	0.84	0.013	1.65	0.004	1.86	0.490	1.0	65.4	170.0
Site 2:											
	Leg G	0.85	0.83	0.179	1.28	0.011	1.76	0.470	1.0	10.8	144.7
	Leg J	0.85	0.83	0.005	1.88	0.011	1.76	0.470	1.0	43.4	180.2
<u>Corpus Christi</u>											
	Short-Range	6.37	2.19	0.008	1.39	0.057	1.0	0.118	1.0	1.6	3.4
	Long-Range	6.37	2.19	0.041	1.03	0.057	1.0	0.118	1.0	1.4	5.5
<u>Panama City</u>											
	Deep, Leg C	1.85	0.53	0.029	1.59	0.003	1.86	0.501	1.0	218.3	281.6
	Shallow, Leg D	1.85	0.53	0.009	1.71	0.003	1.86	0.501	1.0	73.6	146.1

73.3 180.1  
65.4 170.0  
10.8 144.7  
43.4 180.2  
1.6 3.4  
1.4 5.5  
218.3 281.6  
73.6 146.1

Biot theory will be considered. These effects are the frequency dependent viscous losses and the frame losses.

The most sensitive of the input parameters is the permeability which is calculated, Equation (46), from the mean grain diameter (in mm) and its standard deviation. The permeability is smallest for the fine grain sizes, and poorer sorting (large  $\sigma_\phi$ ) reduces the permeability. Consequently, a poorly sorted sediment has the absorption characteristics of a finer sediment. Hovem (1980) has derived an absorption relation using a modified suspension theory in order to include the effects of sorting. As noted in Chapter II, sorting is handled within the permeability calculation in an empirical manner and has the greatest effect on the coarser grain-sizes.

Within the Biot theory, losses due to the inelastic nature of the granular frame are included by making the shear and bulk modulus (for the frame) complex functions. This is expressed by the pair of equations for  $\bar{k}_b$  and  $\bar{\mu}$  [Equation (39)]. These are calculated, as discussed by Stoll, from experimental values for the log decrement ( $\Delta_E$  and  $\Delta_S$ ) and the longitudinal and shear velocity for the dry, granular frame material ( $v_E$  and  $v_S$ ). These steps involve Equations (40) through (44) and, based on Stoll's work, require different values for  $\Delta_E$ ,  $\Delta_S$ , and  $\alpha$ , depending on the grain-size. Thus, to provide consistency, values of 0.15, 0.20, and 1.2 were assumed for  $\Delta_E$ ,  $\Delta_S$ , and  $\alpha$ , respectively, for mean grain-sizes less than 2.5 phi, and 0.45, 0.60, and 3.0 for  $M_z$  greater than 2.5 phi. Above 4 phi, the main effect of selecting the larger values is to increase the magnitude of the attenuation and not the frequency dependence. Stoll reports good agreement with other fine sediment data, but the data reported

here, although in good agreement, is not considered extensive enough to provide unquestioned verification of Stoll's approach to this aspect of the theory.

The effect of losses due to frame inelasticity (e.g., intergranular friction) may be evaluated by removing this mechanism, setting  $\Delta_E = \Delta_S = 0$ , and comparing the absorption with that predicted using the values noted for the log decrement. This was done for mean grain-sizes ranging from 0 to 7  $\phi$  in 1  $\phi$  increments ( $\sigma_\phi = 0.5$ ) over a frequency range of 50 to 750 Hz. The results indicate that frame losses play a dominant role for  $M_z \geq 2 \phi$ , based on an arbitrary threshold defined by absorption values within 10 percent of the normal case. This result is somewhat frequency dependent as the equality in the above relation holds for frequencies of 100 Hz or less. As expected, this is in agreement with Stoll.

The contribution from viscous, flow-related losses was evaluated over the same range of grain-size and frequency by forcing the function  $F$ , in Equations (30) and (31), to be unity. The results show that this type of loss dominates for  $M_z < 2 \phi$ , based on the same criteria as above. Some frequency dependence was noted for  $M_z = 1$ , as the flow losses dominated at 400 Hz and above.

8.1.3 Accuracy of predicted absorption. In Chapters IV through VI, absorption was predicted using the methods of Biot and Hamilton. The results were compared with the experimental absorption calculated from mode-attenuation coefficients. These comparisons were, in general, good, but in recalling this data (Figures 16, 21, 27, and 29), it is obvious that the predicted absorption agrees better with the experimental results for some sites than for others. It is also apparent

that the Biot model appears to give better results than the method of Hamilton. However, if some numerical measure of closeness could be calculated, the comparisons would have more meaning. This was done by calculating the root-mean-square (RMS) difference over the applicable frequency range between the experimental absorption values and the values predicted by the models. Thus, from Tables 4, 11, 19, and 25, experimental values of  $\alpha_A$  were obtained, and using the power law form of the predicted absorption from Table 31, differences were calculated for each frequency. The RMS values of these differences were then calculated for each set of data and are listed in Table 31.

The magnitude of the RMS difference is a measure of how well the predicted absorption fits the experimental data. Thus, in Table 31, the site with the best agreement is seen to be the Corpus Christi site, and the site with the worse agreement is Leg C at Panama City. The data has been edited by deleting some high-frequency data as discussed previously so that for the data considered, the dominant loss mechanism is volume absorption in the sediments. However, the poor agreement at the higher frequencies is still the greatest contributor to the large RMS difference for Leg C. In comparing the RMS values obtained using the Biot and Hamilton approaches, it is obvious that, in all cases, the Biot model predictions give the best fit. It is of interest to note that the Corpus Christi site, at which the best agreement between measured and predicted absorption was obtained, is also the site at which the best bottom data, in the form of cores along the shot track, was obtained.

The frequency dependence of bottom absorption is another point of interest illustrated in Table 31. The experimental data collected

by Hamilton over a wide range of frequencies show a first power dependence on frequency; however, as has been discussed, this point is disputed by many researchers. As can be seen in Table 31, power law fits to the experimental data show a first power dependence only for the long-range shot track at Corpus Christi. Some variation does exist, but in all other cases, the frequency dependence of the experimental data is much greater than the first power. The predictions of the Biot model tend to show either unity or something approaching a second power frequency dependence.

## 8.2 Conclusions

As noted previously, the ultimate goal of developing a valid sediment model is to improve transmission loss predictions. Sediment absorption is one loss mechanism among several which must be modeled effectively if transmission loss predictions are to be improved. A site off the coast of Nova Scotia was selected to evaluate the Biot and Hamilton models for computing sediment absorption within the adiabatic normal-mode propagation model. The Nova Scotia site presented difficulties due to its range dependence, but it was also very well characterized by a number of data sources. This data implies that sediment absorption was the dominant loss mechanism along the propagation track. The results of the transmission loss predictions for this site in Chapter VII appear to confirm this, as good agreement was obtained for frequencies from 25 to 250 Hz. The results at 800 Hz were much poorer for reasons discussed in Section 7.5.3.

The processes involved in constructing the seabed model for the propagation track and the subsequent results lead to several conclusions, some of which relate to the sediment model, while others reflect upon the propagation model itself.

- (1) The Biot model, with appropriate inputs, provides good estimates of the bottom absorption needed to model propagation loss. The Hamilton model performs well for fine-grained sediments, but does not perform adequately for coarse-grained sediments due to its linear dependence upon frequency.
- (2) It is extremely important to know as much about the deeper sediment layers as about the surficial layer. The depth of interest is approximately one wavelength so that, if the lowest frequency considered is 25 Hz as for the Nova Scotia site, then the bottom parameters must be specified to a depth of 60 m or so.
- (3) The combination of high resolution sub-bottom profiling and deep cores will provide this type of data. For the Nova Scotia site, grab-samples rather than cores were available; however, the site was one which had been extensively studied by the Bedford Institute of Oceanography. The identification of a sediment type from Hunttec data, or actual grab-sample data, gave a mean grain-size which was then used in the Biot sediment model to obtain the absorption values for propagation modeling.

- (4) A valuable attribute of the Biot model is the ability to modify both fluid and frame parameters. This was of particular value when modeling the sediments consisting of silt containing diffuse gas. At other sites, the bulk modulus for the frame material was modified according to its mineralogy (i.e., the calcium carbonate content).
- (5) Frame losses require further studies to verify Stoll's use of the log decrements in establishing complex bulk and shear moduli for fine- and coarse-grained sediments.
- (6) Modeling of sound propagation through gas-filled sediments must be improved. These sediments are found in both deep-sea and shallow-water areas. McIver (1974) has summarized tests for gas content performed on 35 cores obtained through the Deep Sea Drilling Project (DSDP) and found that the gas is 98 to 100 percent methane in concentrations (for individual cores) ranging from 0.11 to 21.7 percent by volume. The cores were obtained on the Oregon Shelf, in the Aleutian Trench, the Bering Sea, and the Red Sea. By averaging the concentrations obtained on cores from the same region, the concentrations ranged from 1.0 to 15.7 percent. Thus, the concentrations assumed for the Scotian Shelf site are possibly too low.
- (7) Propagation modeling at 800 Hz for the Scotian Shelf and other areas with range-dependent environments necessitates the use of a model which includes mode



coupling. To take advantage of this added sophistication, greater detail in the environmental model may be required.

- (8) The more general case of propagation modeling requires the inclusion of other loss mechanisms. For example, sites having near-surface, high-velocity bedrock will require a solid-bottom model and absorption coefficients for both compressional and shear waves. Very rough bottoms or high seas will require that scattering losses and/or mode coupling be included at even lower frequencies.

## BIBLIOGRAPHY

- Addy, S. K., Behrens, E. W., Haines, T. R., Shirley, D. J., and Worzel, J. L. Correlation of some lithologic and physical characteristics of sediments with high frequency sub-bottom reflection types. Paper presented at the Offshore Technology Conference, Houston, Texas, 1979.
- Anderson, R. S. Statistical correlation of physical properties and sound velocity in sediments. In L. Hampton (Ed.), Physics of sound in marine sediments. New York: Plenum Press, 1974.
- Antoine, J., and Ewing, J. Seismic refraction measurements on the margins of the Gulf of Mexico. J. Geophys. Res., 1963, 68, 1975-1996.
- Antoine, J. W., and Henry, V. J., Jr. Seismic refraction study of shallow part of continental shelf off Georgia coast. Bull. Seismol. Soc. Am., 1965, 49, 601-609.
- Biot, M. A. Theory of elastic wave propagation in a fluid-saturated porous solid. I. Low-frequency range. II. Higher frequency range. J. Acoust. Soc. Am., 1956, 28, 168-191.
- Biot, M. A. Generalized theory of acoustic propagation in porous dissipative media. J. Acoust. Soc. Am., 1962, 34, 1254-1264.
- Brutsaert, W. The propagation of elastic waves in unconsolidated unsaturated granular mediums. J. Geophys. Res., 1964, 69, 243-257.
- Busby, J., and Richardson, E. G. The absorption of sound in sediments. Geophysics, 1957, 22, 821-828.
- Caswell, W. R. The frequency dependence of normal-mode attenuation in shallow-water sound propagation. Unpublished doctoral dissertation, The Pennsylvania State University, 1979.
- Clay, C. S., and Medwin, H. Acoustical oceanography: Principles and application. New York: John Wiley and Sons, 1977.
- Cole, B. F. Marine sediment attenuation and ocean-bottom reflected sound. J. Acoust. Soc. Am., 1965, 38, 291-297.
- Dobrin, M. B. Introduction to geophysical prospecting (3rd ed.). New York: McGraw-Hill, 1976.
- Eby, R. K., Williams, A. O., Jr., Ryan, R. P., and Tamarkin, P. Study of acoustic propagation in a two-layered model. J. Acoust. Soc. Am., 1960, 32, 88-99.

- Ewing, J., Antoine, J., and Ewing, M. Geophysical measurements in the Western Caribbean Sea and in the Gulf of Mexico. J. Geophys. Res., 1960, 65, 4087-4126.
- Ferris, R. H. Comparison of measured and calculated normal-mode amplitude functions of acoustic waves in shallow water. J. Acoust. Soc. Am., 1972, 52, 981-988.
- Ferry, J. D. Viscoelastic properties of polymers. New York: John Wiley and Sons, 1961.
- Gaspin, J. B., and Shuler, V. K. Source levels of shallow underwater explosions (Report NOLTR 71-160). White Oak, Maryland: Naval Ordnance Laboratory, 1971.
- Gould, H. R., and Stewart, R. H. Continental terrace sediments in the northeastern Gulf of Mexico. In J. L. Hough, and H. W. Menard (Eds.), Finding ancient shorelines. Soc. Econ. Paleontologists and Mineralogists Special Pub. No. 3, 1955, 2-20.
- Hamilton, E. L. Sound velocity, elasticity, and related properties of marine sediments, North Pacific. II. Elasticity and elastic constants (NUC TP 144). San Diego, California: Naval Undersea Research and Development Center, 1969.
- Hamilton, E. L. Sound attenuation in marine sediments (NUC TP 281). San Diego, California: Naval Undersea Research and Development Center, 1972.
- Hamilton, E. L. Geoacoustic models of the sea floor. In L. Hampton (Ed.), Physics of sound in marine sediments. New York: Plenum Press, 1974.
- Hamilton, E. L. Acoustic and related properties of the sea floor: sound attenuation as a function of depth (NUC TP 482). San Diego, California: Naval Undersea Research and Development Center, 1975.
- Hampton, L. D. Acoustic properties of sediments. J. Acoust. Soc. Am., 1967, 42, 882-890.
- Hardin, B. O. The nature of damping in sands. J. Soil Mechanics and Foundations Div., Proc. Am. Soc. Civil Eng., 1965, SM1, 91, 63-97.
- Hardin, B. O., and Richart, F. E., Jr. Elastic wave velocities in granular soils. J. Soil Mechanics and Foundations Div., Proc. Am. Soc. Civil Eng., 1963, SM1, 89, 33-65.
- Hersey, J. B., Bunce, E. T., Wyrick, R. F., and Dietz, F. T. Geophysical investigation of the continental margin between Cape Henry, Virginia, and Jacksonville, Florida. Bull. Geol. Soc. Am., 1950, 70, 437-466.

- Houston, M. H., Jr. Shallow water acoustic structure of the continental shelf by continuous refraction profiling with a multichannel towed array. In Proceedings workshop on seismic propagation in shallow water. Arlington, Virginia: Office of Naval Research, 1978.
- Hovem, J. M. Attenuation of sound in marine sediments. In Proceedings SACLANTCEN conference on bottom-interacting ocean acoustics. La Spezia, Italy, 1980.
- Hughes, R. C. Low frequency underwater explosive source levels. J. Acoust. Soc. Am., 1976, 60, Suppl. 1, S72 (A).
- Ingenito, F. Measurements of mode attenuation coefficients in shallow water. J. Acoust. Soc. Am., 1973, 53, 858-863.
- Ingenito, F., and Wolf, S. N. Acoustic propagation in shallow water overlying a consolidated bottom. J. Acoust. Soc. Am., 1976, 60, 611-617.
- Ingenito, F., Ferris, R. H., Kuperman, W. A., and Wolf, S. N. Shallow water acoustics: Summary report (first phase) (NRL Report 8179). Washington, D. C.: Naval Research Laboratory, 1978.
- Johnston, D. H., Toksöz, M. N., and Tinnus, A. Attenuation of seismic waves in dry and saturated rocks: II. Mechanisms. Geophysics, 1979, 44, 691-711.
- Kibblewhite, A. C., and Denham, R. N. Experiment on sound propagation in shallow water under isovelocity conditions. J. Acoust. Soc. Am., 1966, 40, 1337-1344.
- King, L. H. Surficial geology of the Halifax-Sable Island map area. Marine sciences Paper 1. Ottawa, Canada: Department of the Environment, 1970.
- King, L. H., and MacLean, B. Geology of the Scotian Shelf. Marine Sciences Paper 7. Ottawa, Canada: Department of the Environment, 1976.
- Korn, G. A., and Korn, T. M. Mathematical handbook for scientists and engineers (2nd ed.). New York: McGraw-Hill, 1968.
- Kornhauser, E. T., and Raney, W. P. Attenuation in shallow-water propagation due to an absorbing bottom. J. Acoust. Soc. Am., 1955, 27, 689-692.
- Krumbein, W. C., and Monk, G. D. Permeability as a function of the size parameters of unconsolidated sand. Petroleum Technology, Am. Inst. Mining and Metallurgical Engineers, Tech. Pub. No. 1492, 1942, 1-9.

- Ludwick, J. C. Sediments in northeastern Gulf of Mexico. In R. C. Miller (Ed.), Papers in marine geology, Shepard Commemorative Volume. New York: MacMillan Co., 1964.
- Mackenzie, K. V. Reflection of sound from coastal bottoms. J. Acoust. Soc. Am., 1960, 32, 221-231.
- McCann, C., and McCann, D. M. The attenuation of compressional waves in marine sediments. Geophysics, 1969, 34, 882-892.
- McDaniel, S. T. Mode conversion in shallow-water sound propagation. J. Acoust. Soc. Am., 1977, 62, 320-325.
- McDaniel, S. T. Measurement of the attenuation of acoustic normal modes. J. Acoust. Soc. Am., 1979, 65, Suppl. No. 1, S18 (A).
- McDaniel, S. T. Sediment shear-wave velocities derived from Stonely wave observations. J. Acoust. Soc. Am., 1980, 67, Suppl. 1, S30 (A).
- McIver, R. D. Hydrocarbon gas (methane) in canned deep sea drilling project core samples. In I. R. Kaplin (Ed.), Natural gases in marine sediments. New York: Plenum Press, 1974.
- McMillan, K. J., Haines, T., and Addy, S. K. Sediments of the northwest Florida and Alabama shelves and upper slope. Unpublished manuscript, The University of Texas at Austin, 1978.
- Meisburger, E. P., and Field, M. E. Geomorphology, shallow structure and sediments of the Florida inner continental shelf, Cape Canaveral to Georgia (Report TM-54). Fort Belvoir, Virginia: U. S. Army Corps of Engineers, Coastal Engineering Research Center, 1975.
- Miller, J. F., and Ingenito, F. Normal mode FORTRAN programs for calculating sound propagation in the ocean (NRL Memorandum Report 3071). Washington, D. C.: Naval Research Laboratory, 1975.
- Milliman, J. D., Pilkey, O. H., and Ross, D. A. Sediments of the continental margin off the eastern United States. Geol. Soc. Am. Bull., 1972, 83, 1315-1334.
- Morse, R. W. Acoustic propagation in granular media. J. Acoust. Soc. Am., 1952, 24, 696-700.
- Neprochnov, Y. P. Seismic studies of the crustal structure beneath the seas and oceans. Oceanology, 1971, 11, 709-715.

- Nolle, A. W., Hayer, W. A., Mifsud, J. F., Runyan, W. A., and Ward, M. B. Acoustic properties of water-filled sands. J. Acoust. Soc. Am., 1963, 35, 1394-1408.
- Officer, C. B. Introduction to the theory of sound transmission. New York: McGraw-Hill, 1958.
- Parrott, D. R., Dodds, D. J., King, L. H., and Simpkin, R. G. Measurement and evaluation of the acoustic reflectivity of the sea floor (Huntec Report H7903-02/SB/DRP). Scarborough, Ontario, Canada: Huntec ('70) Ltd., 1979.
- Pekeris, C. L. Theory of propagation of explosive sound in shallow water. Geological Society of America Memoir 27, 1948.
- Pierce, A. D. Extension of the method of normal modes to sound propagation in an almost-stratified medium. J. Acoust. Soc. Am., 1965, 37, 19-27.
- Plona, T. J. Observation of a second bulk compressional wave in a porous medium at ultrasonic frequencies. Appl. Phys. Lett., 1980, 36, 259-261.
- Rubano, L. A. Acoustic propagation in shallow water over a low-velocity bottom. J. Acoust. Soc. Am., 1980, 67, 1608-1613.
- Sheridan, R. E., Drake, C. L., Nafe, J. E., and Hennion, J. Seismic-refraction study of continental margin east of Florida. Bull. Am. Assoc. Petroleum Geologists, 1966, 50, 1972-1991.
- Shirley, D. J., and Anderson, A. L. In-situ measurement of marine sediment acoustical properties during coring in deep water. IEEE Trans. Geoscience Electronics, 1975, GE-13, 163-169.
- Shumway, G. Sound speed and absorption studies of marine sediments by a resonance method, Parts I and II. Geophysics, 1960, 25, 451-467, 659-682.
- Stoll, R. D. Acoustic waves in saturated sediments. In L. Hampton (Ed.), Physics of sound in marine sediments. New York: Plenum Press, 1974.
- Stoll, R. D., Acoustic waves in ocean sediments. Geophysics, 1977, 42, 715-725.
- Stoll, R. D. Experimental studies of attenuation in sediments. J. Acoust. Soc. Am., 1979, 66, 1152-1160.
- Stoll, R. D., and Bryan, G. M. Wave attenuation in saturated sediments. J. Acoust. Soc. Am., 1970, 47, 1440-1447.

- Tolstoy, I. Shallow water test of the theory of layered wave guides. J. Acoust. Soc. Am., 1958, 30, 348-361.
- Tolstoy, I., and Clay, C. S. Ocean acoustics. New York: McGraw-Hill, 1966.
- Trask, P. D. Part II. Chemical studies of sediments of the western Gulf of Mexico. Papers in Physical Oceanography and Meteorology, Massachusetts Institute of Technology and Woods Hole Oceanographic Institution, 1953, 12, 46-120.
- Walton, K. Elastic wave propagation in model sediments, I. Geophys. J. Royal Astronomical Soc., 1977, 48, 461-478.
- Weston, D. E. Underwater explosions as acoustic sources. Proc. Phys. Soc. London, 1960, 76, 233-249.
- Weston, D. E. Contradiction concerning shallow-water sound attenuation. J. Acoust. Soc. Am., 1967, 42, 526-527.
- Weston, D. E., and Ching, P. A. Sound extinction by fish in one-way shallow-water propagation (MC Report 005). In Proceedings International Symposium on Biological Sound Scattering in the Ocean. Washington, D. C.: Naval Research Laboratory, 1970.
- Williams, A. O., Jr., and Eby, R. K. Acoustic attenuation in a liquid layer over a 'slow' viscoelastic solid. J. Acoust. Soc. Am., 1962, 34, 836-843.
- Wood, A. B. A text-book of sound. London: G. Bell and Sons, Ltd., 1944.
- Wood, A. B., and Weston, D. E. The propagation of sound in mud. Acustica, 1964, 14, 156-162.
- Worzel, J. L., and Ewing, M. Explosion sounds in shallow water. Geological Society of America Memoir 27, 1948.

## APPENDIX A

### NORMAL-MODE INTEGRAL EVALUATION

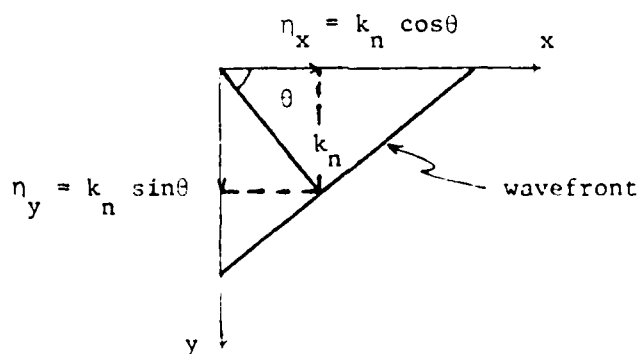
In Section 2.1.1, the velocity potential solution in cylindrical coordinates is obtained by evaluating the integral

$$I = \int_{-\infty}^{\infty} \int_{-\infty}^{\infty} \frac{e^{i(\eta_x x + \eta_y y)}}{\eta^2 - k_n^2} d\eta_x d\eta_y \quad . \quad (A1)$$

We first rotate coordinates so that  $\eta_x = \frac{x}{r} \eta'_x - \frac{y}{r} \eta'_y$  and  $\eta_y = \frac{y}{r} \eta'_x + \frac{x}{r} \eta'_y$ , where  $r^2 = x^2 + y^2$ . If we then drop the prime (') on  $\eta'_x$  and  $\eta'_y$ , Equation (A1) becomes:

$$I = \int_{-\infty}^{\infty} \int_{-\infty}^{\infty} \frac{e^{ir\eta_x}}{\eta^2 - k_n^2} d\eta_x d\eta_y \quad . \quad (A2)$$

This integral may be evaluated by first performing the integration over  $\eta_x$ . Since  $\eta^2 = \eta_x^2 + \eta_y^2$ , the integrand will have singularities on the real axis at  $\eta_x = \pm \sqrt{k_n^2 - \eta_y^2}$ . These roots are real since  $\eta_x$  and  $\eta_y$  correspond to the  $x$  and  $y$  components of the modal wave number  $k_n$  and, as shown below, will always be less than or equal to  $k_n$ .





The integral over  $\eta_x$  is then

$$I_x = \int_{-\infty}^{\infty} \frac{e^{i r \eta_x}}{(\eta_x + \sqrt{k_n^2 - \eta_y^2})(\eta_x - \sqrt{k_n^2 - \eta_y^2})} d\eta_x \quad (A3)$$

The integral is evaluation by integration in the complex  $z$ -plane using Cauchy's residue theorem and the contour in Figure 34. In the figure, the two roots,  $z_1$  and  $z_2$ , have been given very small complex values  $\epsilon$  so as to move the roots away from the real axis. In Figure 34,  $\epsilon$  is chosen positive to insure that the radiation condition holds.

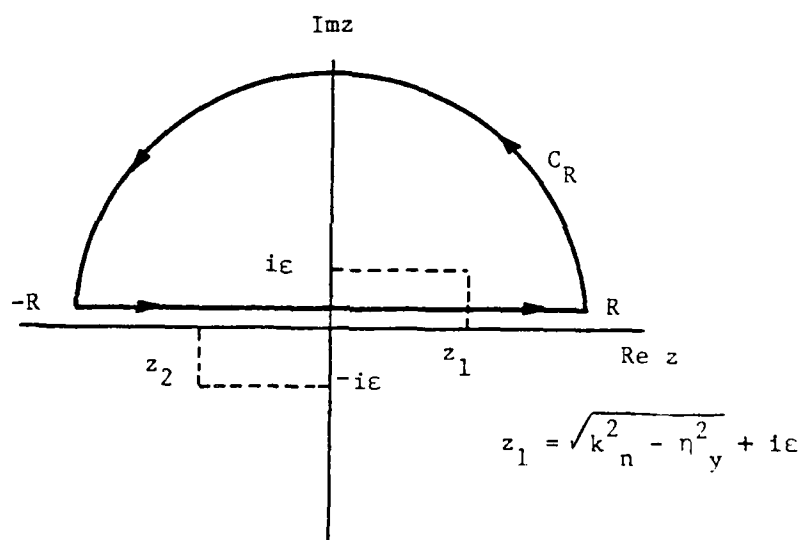


Figure 34. Contour for  $\eta_x$  Integration

The integral on  $(-\infty, \infty)$  may then be broken down as

$$I_x = \int_{-\infty}^{\infty} = \lim_{R \rightarrow \infty} \left[ \int_{-R}^R + \int_{C_R} \right] = 2\pi i \sum \text{Residues} \quad .$$

It may be shown that  $\int_{CR} \rightarrow 0$  and the integral is then equal to the residue of the pole  $z_1$  enclosed by the integration contour. The positive root is chosen in closing the contour to insure propagation away from the source. We have then for the integration over  $\eta_x$  that

$$I_x = \pi i \frac{e^{i\sqrt{k_n^2 - \eta_y^2} x}}{\sqrt{k_n^2 - \eta_y^2}} \quad (A4)$$

when  $\epsilon$  goes to zero.

The integral on  $\eta_y$  to be evaluated is then

$$I_y = \pi i \int_{-\infty}^{\infty} \frac{e^{ir\sqrt{k_n^2 - \eta_y^2}}}{\sqrt{k_n^2 - \eta_y^2}} d\eta_y \quad (A5)$$

Noting that  $\eta_y = k_n \sin\theta$  and  $\sqrt{k_n^2 - \eta_y^2} = k_n \cos\theta$ , Equation (A5) becomes

$$I_\theta = \pi i \int_{-\pi/2+i\infty}^{\pi/2-i\infty} e^{ik_n r \cos\theta} d\theta \quad (A6)$$

which has been identified by Korn and Korn (1968) as Sommerfeld's integral. The integral is evaluated by letting  $\theta$  become complex with the integration limits shown. For these limits, Korn and Korn show that

$$\frac{1}{\pi} \int_{-\pi/2+i\infty}^{\pi/2-i\infty} e^{ik_n r \cos\theta} d\theta = H_0^{(1)}(k_n r) \quad (A7)$$

with the result that

$$I = i\pi^2 H_0^{(1)}(k_n r) \quad .$$

DISTRIBUTION

Commander (NSEA 0342)  
Naval Sea Systems Command  
Department of the Navy  
Washington, D.C. 20362

Copies 1 and 2

Commander (NSEA 9961)  
Naval Sea Systems Command  
Department of the Navy  
Washington, D.C. 20362

Copies 3 and 4

Defense Technical Information Center  
5010 Duke Street  
Cameron Station  
Alexandria, VA 22314

Copies 5 through 16

END